

ENGINEERING

EDGE

Accelerate Innovation
with CFD & Thermal
Characterization



**Airbus
Operations
Ltd.**
Aircraft Refuel
Rig Modeling
Page 10

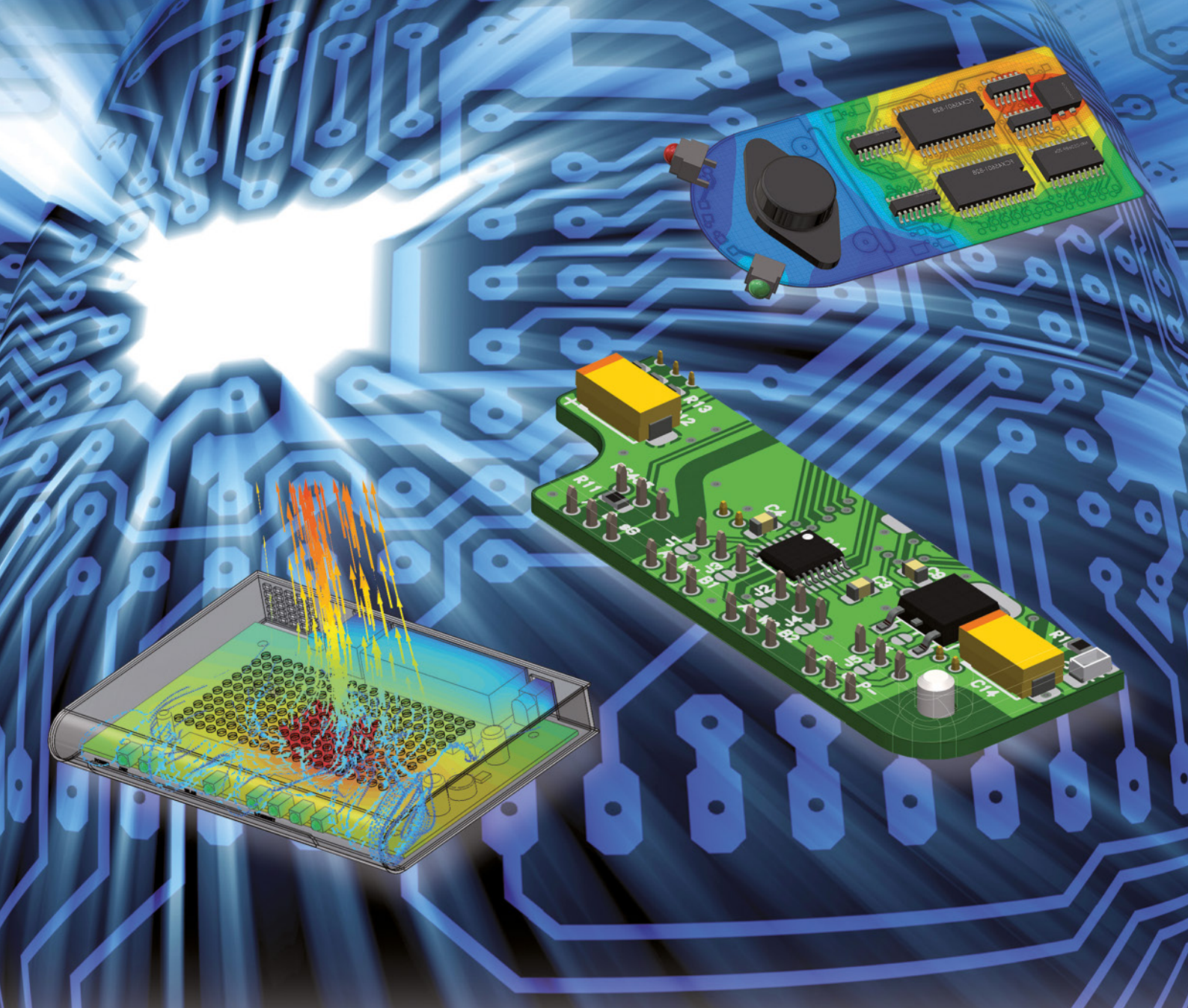
Lenovo
Electrolytic
Capacitor
Thermal
Conductivity
Study
Page 40

**Robert Bosch
Automotive
Steering
GmbH**
Flow Conditions
Optimization
Page 60

mentor.com/mechanical

**Mentor
Graphics**

— Mechanical Analysis



Learn to drive FloTHERM[®] XT

- With this hands-on virtual lab
- Become proficient using FloTHERM XT
- Create accurate thermal models in less time

Register Now for your instant 30 Day Free Trial
Go.mentor.com/flothermxt-vlab

Mentor
Graphics[®]

— Mechanical Analysis



**Mentor
Graphics**

— Mechanical Analysis

Mentor Graphics Corporation

Pury Hill Business Park,
The Maltings,
Towcester, NN12 7TB,
United Kingdom
Tel: +44 (0)1327 306000
email: ee@mentor.com

Editor:
Keith Hanna

Managing Editor:
Natasha Antunes

Copy Editor:
Jane Wade

Contributors:
Robin Bornoff, Mike Croegaert, Mike Gruetzmacher, Keith Hanna, Doug Kolak, Boris Marovic, John Murray, John Parry, Nazita Saye, Thomas Schultz, Prasad Tota, Tatiana Trebunskikh, Katherine Tupper, John Wilson

With special thanks to:
Airbus Operations Ltd.,
Analog Devices Inc.,
battenfeld-cincinnati,
Chongqing Changan Motors,
EnginSoft Italy,
EU Joint Research Center ISPRa,
Kitasato University School of Allied Health Sciences,
Lenovo,
Liebherr-Werk Nenzing GmbH,
Mercury Racing,
Pan Asia Technical Automotive Center,
Robert Bosch Automotive Steering GmbH,
Rockwell Collins,
Rohm Semiconductors, and
University of Nottingham

©2016 Mentor Graphics Corporation, all rights reserved. This document contains information that is proprietary to Mentor Graphics Corporation and may be duplicated in whole or in part by the original recipient for internal business purposes only, provided that this entire notice appears in all copies. In accepting this document, the recipient agrees to make every reasonable effort to prevent unauthorized use of this information. All trademarks mentioned in this publication are the trademarks of their respective owners.

Perspective

Vol. 05, Issue. 01



Greetings readers! I served for a time in the German military as a helicopter pilot and also lectured in aerodynamics part-time. I look back fondly to those days and I retain an abiding passion for everything aircraft. This edition's cover story from Airbus' thermo-fluid modeling of fuel systems reminded me again of the immense complexity of modern aeroplanes and how simulation tools (like Mentor's Flowmaster® in this instance) are mission critical to the design and maintenance of complex systems and systems-of-systems. Our unique ability to model 3D components

in FloEFD™ and 1D systems in Flowmaster means we can offer design-centric insights early in the customer design processes unlike any other company in the marketplace.

Two years ago we released our MicReD® Industrial Power Tester 1500A with three channels to meet an increasing need in the power electronics market for thermal cycling and non-destructive thermal characterization of IGBTs during their lifetime. The product has seen a huge uptake in usage, such that we have released a 12 channel 1500A Power Tester and recently in February, 1800A and 3600A versions. In this edition of Engineering Edge we announce a significant new release from our MicReD stable, the 600A Power Tester to meet the specific needs of the automotive electric vehicle and hybrid electric vehicle power electronics sectors, with a machine that can be scaled to test up to 128 power modules in series. Nottingham University in the UK, who purchased the first Power Tester, report some fascinating results from their research that shows how the delamination of IGBTs can be quantified with the equipment throughout their lifetime, (Page 14). And with the release of FloTHERM® 11.1 last year we offer unprecedented accuracy in 3D electronic thermal simulations of power electronics when calibrated with our T3Ster based hardware measurements.

This edition of Engineering Edge has a very strong automotive flavor from around the world and across our product lines. From Robert Bosch (ZF) steering systems and Liebherr cranes in Germany to HVAC ducts/heat exchangers and lubrication systems in China (PATAC and Chongqing). Not to mention 1D-3D CFD for power electronics cooling inside electric vehicles (Hyundai in Korea), we see the range and versatility of our FloEFD, FloTHERM and Flowmaster products for this industry.

Finally, in our News Section, we announce a new "Frontloading CFD Award" which aims to recognize excellence and the excellent ROI to be found with FloEFD in the early design stages of manufactured product development. In addition, Prof Lorenzo Codecasa from Milan has been acknowledged for his work on the mathematics of reduced order models as applied to electronics thermal simulations by winning the 2016 Harvey Rosten Award (Page 8). And we should not forget our very own FloTHERM XT recently won the prestigious Electronic Products Magazine "Product of the Year" Award for a "...thermal simulation tool that connects MCAD and EDA" which is a testament to our Product Managers and developers in the FloTHERM product line and the realization of their original vision.

**Roland Feldhinkel, General Manager,
Mechanical Analysis Division, Mentor Graphics**



News

- 6 **New Release:
MicReD® Power
Tester 600A**
- 7 **FloTHERM® XT Wins
Product of the Year**
- 8 **Harvey Rosten
Award 2016**
- 8 **New Release:
Flowmaster® v7.9.5**
- 9 **FloEFD™
Frontloading CFD
Award Announcement**

Engineering Edge

- 10 **Airbus Operations Ltd.**
Aircraft Refuel Rig Pressure
Surge Modeling
- 14 **University of
Nottingham**
Quantification of Cracked Areas in
Thermal Path of High-Power Modules
- 20 **Early Stage Analysis
of EV Power
Electronics**
- 27 **Analog Devices Inc.**
Thermal Analysis of PCB Mounted
Small Outline Packages

- 35 **Liebherr-Werk
Nenzing GmbH**
The Liebherr LHM 550 Mobile Harbor Crane
- 37 **Rockwell Collins**
In-Depth Lessons Learned: Review
of an Avionics Thermal Analysis Project
- 40 **Lenovo**
Electrolytic Capacitor Thermal
Conductivity Study
- 47 **battenfeld-cincinnati**
FloEFD to Model High-spec
Extrusion Pipes
- 49 **Chongqing
Changan Motors**
Analysis of the Optimized Designs for the
WL Engine Lubrication System

52 Rohm Semiconductors

Dynamic Compact Thermal
Model Development

54 Pan Asia Technical Automotive Center

HVAC Module Temperature Linearity Design

57 EU Joint Research Center ISPRA

European Nuclear Safeguards

60 Robert Bosch Automotive Steering GmbH

Flow Conditions Optimization

62 Mercury Racing

Innovation as Standard

64 Kitasato University School of Allied Health Sciences

Hole Implantable Collamer Lens

14

Contents



Regular Features

24 Ask the GSS Expert

Simplifying Modeling Challenges
in Complex Networks

32 How To...

How to characterize Heat Exchangers

45 Interview

Alberto Deonti, EnginSoft SpA

68 Geek Hub

What's the Fastest Way to Dry
your Hands?

70 Brownian Motion

New Release: Unique MicReD® Power Tester 600A for EV/HEVs

Mentor Graphics is pleased to announce the launch of the MicReD® Power Tester 600A, which tests electric and hybrid vehicle (EV/HEV) power electronics reliability during power cycling. The MicReD Power Tester 600A allows EV/HEV development and reliability engineers to test power electronics (such as insulated gate bipolar transistors – IGBTs, MOSFETs, transistors, and chargers) for mission-critical thermal reliability and lifecycle performance. Thermal reliability issues can result in EV/HEV automotive recalls, and the ever wider adoption of electric and hybrid cars has created a specific need for this solution. The Mentor Graphics® MicReD Power Tester 600A also meets the industry's need for power electronics thermal simulation and test, delivering unmatched accuracy and scalability.

Delta Electronics develops high-efficiency and high-density power module products in Taiwan. "We apply the Power Tester 1500A to gain insight into the lifetime performance and assure the reliability of the IGBT module," said Andy Liao, section manager, Delta Electronics. "The Power Tester 600A could provide a scalable solution that would allow us to measure many discrete power devices or modules concurrently. This increased testing throughput would give us statistical failure data that we need in order to accurately predict the field lifetime of the products."

Reliability, Accuracy and Scalability Solves EV/HEV Power Electronics Thermal Issues

Designers of today's EV/HEVs are faced with significant mission-critical challenges: foremost among these is ensuring the thermal reliability of power electronics modules; detecting potential degradation of IGBTs caused by a range of standard drive cycles; and identifying the underlying damage root causes. Mentor's MicReD Power Tester 600A solution provides accurate and reliable test results that scale to real-world requirements:

- **Comprehensive Diagnostics for Thermal Reliability:** The MicReD Power Tester 600A product provides a simple reliability testing process for lifecycle



Figure 1. MicReD Power Tester 600A

estimation. Device set-up is easy and power cycles are fully automated. The T3Ster® "structure function" feature inside the Power Tester yields non-destructive "failure-in-progress" data for each IGBT. All diagnostic information is recorded during testing, from current, voltage and die temperature sensing, to "structure function" changes that point to reasons for failures in the package structure. Package development, reliability and batch checking of incoming parts can now be tested before production.

- **Simulation Accuracy:** The MicReD Power Tester 600A product can power IGBT modules through tens of thousands of cycles. This provides "real-time" failure-in-progress data for diagnostics, significantly reducing test time and eliminating the need for post-mortem or destructive failure analysis. Associated 3D CFD (computational fluid dynamics) simulation errors can be reduced from typically up to 20% to 0.5% for accurate thermal characterization of IGBTs and components due to Mentor's calibration technology solely found in the MicReD T3Ster product.

- **Scalability – Tests Up to 128 IGBTs in Series:** Up to eight MicReD 600A Power Testers can be chained together to allow users to power cycle up to 128 IGBTs simultaneously in a system test. The MicReD Power Tester 600A product delivers 48V under load, and users can deal with components mounted externally on cooling systems for maximum flexibility. The MicReD Power Tester 600A also meets the needs of emerging de facto EV/HEV power electronics testing best practices such as those currently being developed for the German automotive industry.

MicReD Power Tester 600A – Part of a Comprehensive Solution

Mentor Graphics is uniquely positioned as the only company that can provide a complete thermal software simulation and hardware testing solution specifically for the EV/HEV market. The MicReD Power Tester 600A product can be coupled with Mentor's leading CFD simulation technologies. Mentor's FloTHERM® and FloEFD™ 3D CFD software provide for front-loading thermal simulation of power modules. When coupled with the Flowmaster® full vehicle thermo-fluid

system-of-system 1D CFD modeling tool, this yields unparalleled levels of accuracy. This is done by MicReD's T3Ster technology providing CFD input material properties for automated model calibration functionality to accurately simulate the real temperature response of an EV/HEV's dynamic power input. This combination of technologies allows users to generate IGBT thermal lifetime failure estimations with the greatest accuracy possible.

"The MicReD Power Tester 600A is an extension of our total solution in automotive thermal engineering, and there is no other product like this for the EV/HEV market today," stated Roland Feldhinkel, general manager of Mentor Graphics Mechanical Analysis Division. "We have leveraged our best-in-class products to deliver a comprehensive thermal simulation and hardware test solution that meets auto maker EV/HEV industry needs while supporting the rapid growth forecast for the market in the next few years."

Product Availability

Mentor Graphics is now accepting orders for the MicReD Power Tester 600A with shipping scheduled for summer of 2016. For additional product information, please visit: www.mentor.com/powertester-600a.

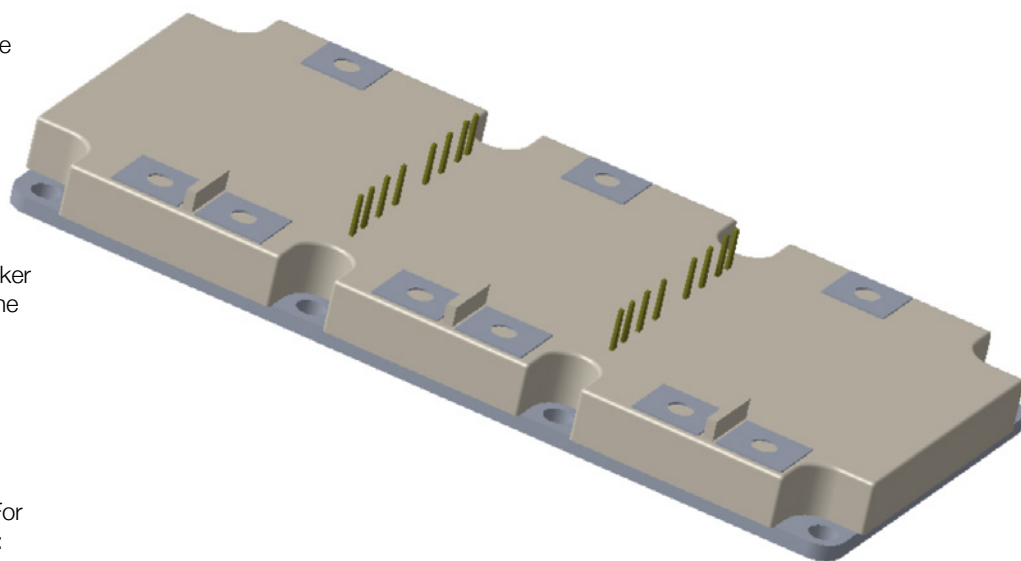
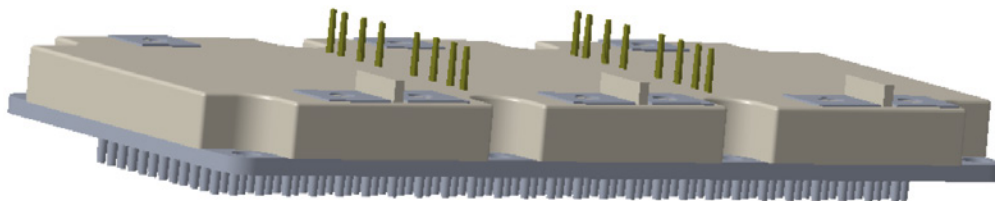


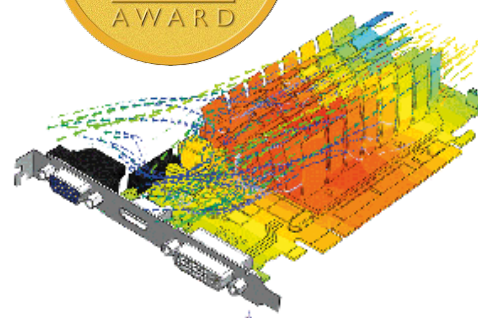
Figure 2. Insulated Gate Bipolar Transistor

FloTHERM® XT Awarded Product of the Year

FloTHERM® XT has been awarded Product of the Year by Electronics Products Magazine. FloTHERM XT is a unique thermal simulation software package that can be used during all stages of the electronics design process to improve design layout and reliability. The tool tightly couples mechanical and electronic CAD design flows and cuts design times significantly with its ability to examine thermal situations early in the EDA-MDA design process.

The package offers a robust geometry engine for complex shapes and supports transient analysis, Joule heating, parametric

studies, and the ability to represent copper in full 3D detail for complex PCBs. FloTHERM XT's CAD-centric technology includes a robust mesher that simulates complex geometries with ease, speed, and accuracy. The tool features an integrated environment for defining, solving, and analyzing results for parametric variations of geometry, material attributes, and other solution parameters that significantly enhances the design process. More information: <http://bit.ly/1ZAORTh>



Harvey Rosten Award 2016 Winner: One Giant Leap for Compact Thermal Models

Compact Thermal Models, or CTMs of chip packages have been a subject of research since the mid 1990s, starting with work done in the DELPHI project. CTMs provide a black box representation of a chip package, allowing package vendors to provide a thermal model for use in design by a systems integrator, yet hide sensitive internal details like die size, thickness, and die attach properties. Despite decades of research, existing methods have had the drawback of only being able to create steady-state models they only represent a single heat source, or dynamic models (DCTMs) that are linear, and so do not take into account the variation of material properties with temperature. They are also limited in that the temperature distribution on the surface of the package is only roughly captured, for example by using two isothermal regions to represent the top or bottom surfaces of the package.

This year's winner, Prof. Codecasa's most recent work, published at the THERMINIC Workshop in Paris in September/October 2015 has overcome all of these limitations and more, by taking a radically different approach to the way DCTMs are derived. He and his co-workers have developed a novel model

order reduction method for the construction of parametric DCTMs. This extends a previous method put forward by the authors to handle non-linear properties, yet preserve the model's dependency on changes to the input parameters, allowing them to be used to explore the design space very quickly to test the sensitivity of the package's thermal performance to say the thermal conductivity of the mold compound. The method is capable of capturing the spatial temperature variation on the package surface, and the temporal variation of the temperature of a massive number of independent heat sources, both with a very high degree of fidelity. These reduced order models take approximately as long to create as performing a single transient simulation on the full 3D conduction model from which they are derived. Thereafter a full transient calculation can be run in just a few minutes.

Lorenzo Codecasa received the Laurea degree (with highest honors) and a Ph. D. degree both in Electronic Engineering from Politecnico di Milano, in 1997 and 2001 respectively. From 2002 to 2010 he worked as Assistant Professor of Electrical Engineering with the Department of Electronics, Information, and Bioengineering of Politecnico di Milano. Since 2010 he has worked as Associate Professor of Electrical Engineering in the same



Figure 1. Lorenzo Codecasa receiving the Harvey Rosten Award in California

Department. His main research contributions are in theoretical analysis and in the computational investigation of electric circuits and electromagnetic fields. As a member of the thermal community he has, in particular, introduced original approaches to the extraction of several classes of compact thermal models, aimed at the effective thermal simulation of packages and electro-thermal simulation of electronic circuits. In his research areas he has authored or co-authored over 150 papers in refereed international journals and conference proceedings.

Flowmaster® V7.9.5

May saw the release of Flowmaster V7.9.5, a significant milestone in that it represents the last of the V7 product releases.

The focus of this latest release is the Airside Visualizer and Segmenter tool, which is now replaced and updated with a modern 3D tool created by a collaborative team from the Flowmaster and FloEFD™ development teams. The new visualizer introduces a number of enhancements to the user interface, all of which are detailed in the updated AVS Appnote, available via SupportNet.

As well as the enhancement to AVS, V795 contains fixes to 29 customer reported issues. For full details, please consult the V7.9.5 Release Highlights document, also available via Supportnet.

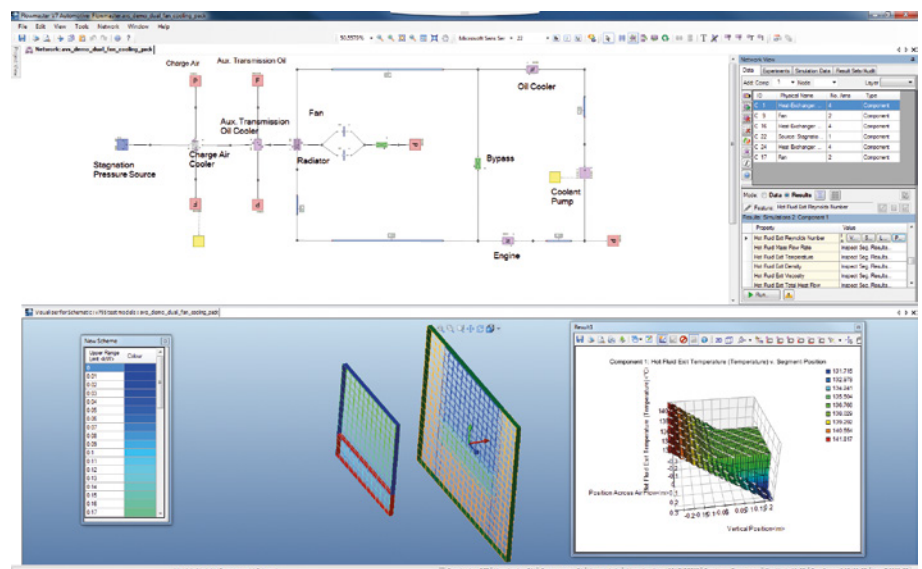


Figure 1. Flowmaster V7.9.5. sees the launch of a brand new AVS 3D Viewer

Announcing the FloEFD™ Frontloading CFD Award



Mentor Graphics is pleased to announce a new award in recognition of excellence in the use of FloEFD in implementing Frontloading CFD.

Frontloading CFD refers to the practice of utilizing CFD simulation to optimize a proposed design early during the design phase – when it is easier and less expensive to modify a design. Since FloEFD is the premier solution for Frontloading CFD, Mentor Graphics is pleased to spread the word about the use of the concept in both research and real-world applications.

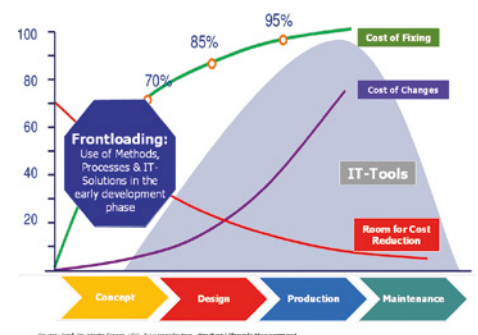
The award judging criteria are as follows:

- Work demonstrates clear application of Frontloading CFD with FloEFD. Published papers, conference papers, Powerpoint presentations (with background info), website content, animations, videos etc. may be submitted in support of entry.

- Work is in the public domain and disseminated to the public within 12 months of the nomination deadline.
- Pragmatic approach has been taken in the application.
- Work and improvement due to use of frontloading CFD and FloEFD is quantifiable.
- Entrant must have authority /permission from their organization to apply (exclude company confidential information).
- Entries must be submitted in full and include all supporting material by the deadline – June 30, 2016.

All eligible work will be scored by the members of the selection committee against the qualification criteria.

The winner and runners up receive a generous cash prize and a plaque in November 2016. The first prize consists of \$1,500 and the two runners up will receive \$500 in cash. If the winners are unable to



accept the cash prize, the amount will be donated on their behalf to their chosen charity instead.

If you are interested in applying for the award, please send an email containing your application including supporting materials by June 30, 2016 to nazita_saye@mentor.com.





Airbus leverages Flowmaster for Aircraft Refueling Rig Pressure Surge Modeling



By D. Morrison, Airbus Operations Ltd, Inerting and Fluid Physics, UK; and
R. Illidge, Airbus Operations Ltd, Fuel & Landing Gear Systems Test, UK



Figure 1. Aircraft refuel from airport underground supply

Civil aircraft refuel systems enable the transfer of fuel under pressure from ground level supply to the required quantity into each fuel tank. The closure of a fuel tank inlet valve may result in a surge pressure. The magnitude will depend on a number of factors, including the closure operation of the tank inlet valve, fuel flow velocity, and the critical time. Certification requirements of an aircraft refuel system include the consideration of surge pressure loading. Full scale refuel test rigs are costly to develop, modify and operate. In an effort to reduce the reliance on these costly test rigs Airbus has attempted to verify a 1D flow simulation approach using Flowmaster.

Fuel is stored onboard civil aircraft in the geometrically complex cavities enclosed by the wing surfaces. Fuel can also be stored in the center tank that connects the two main wing tanks and/or in the horizontal tail plane wing tanks. The fuel tanks are vented to atmosphere, which provides an escape path for fuel in the event of a refuel overflow and pressure equalization of the air (ullage) within the tanks. The fuel inlet total pressure in the aircraft tanks during refuel will be the ullage pressure plus the static head of fuel in the tank. The pressure losses in the system are produced by the pipework and the refuel coupling that controls the flow onboard. The fuel is supplied to the underwing aircraft refuel coupling via a truck with connecting

flexible hose that is pumped from airport underground storage tanks, or mobile fuel storage tanks. The ground refuel pressure is typically 50 psig.

The amount of fuel loaded on an aircraft will be dependent on the planned flight distance so the fill level in the tank will change from flight to flight to manage the onboard fuel weight. Therefore a programmable control is used to provide the correct fuel level. During the refuel operation, as each tank reaches its target capacity, the corresponding fuel inlet valves are commanded shut. The closure of a fuel tank inlet valve may cause a pressure surge event. Typically, full scale refuel test rigs are built to assess the impact of refuel pressure surge on the connecting fuel pipework to ensure that maximum working pressures are not exceeded. If it is determined that the maximum pressures are exceeded then the piping system needs to be redesigned and the test rig will also need to be reconfigured so the redesigned system can be retested. This is an expensive and time consuming process. Therefore, limiting the number of iterations of physical testing with simulation has significant potential value. To be confident in the simulation, Airbus conducted a verification of the Flowmaster model against an existing test rig.

The aircraft refuel test rig is made up of three elevated fuel tanks (center tank, two wing tanks) and the complex connecting pipework necessary for refuel. Fuel is supplied under pressure from ground level via a flexible riser hose attached to the refuel couplings, and enters each targeted tank via a number of inlet valves and diffusers. Figure 2 provides an elevation view of the aircraft refuel test rig. Figure 3 shows a close up view of the refuel coupling and the connected fuel pipework. The three fuel tanks are represented by rectangular volumes in which the required fuel head is achieved via internal overflow weirs – fuel is then returned to ground storage.

During refuel surge tests, various flow configurations and several refueling scenarios were evaluated with high frequency pressure readings being taken from key test rig point locations and the open/closed position of the refuel valves was also recorded.

1D Pressure Surge Model Set Up

Steady Flow

Steady state performance data was linked to the Flowmaster fluid simulation model

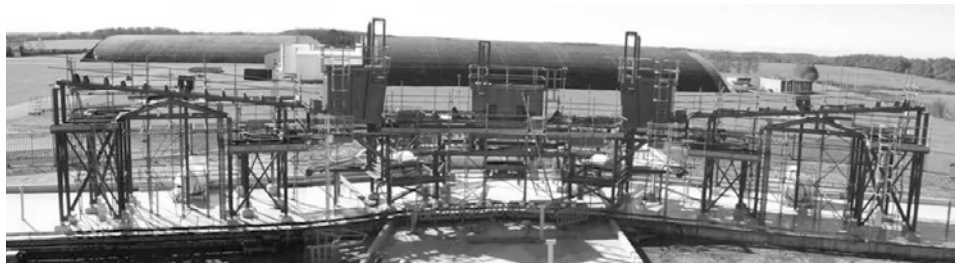


Figure 2. Aircraft refuel test rig, elevation view

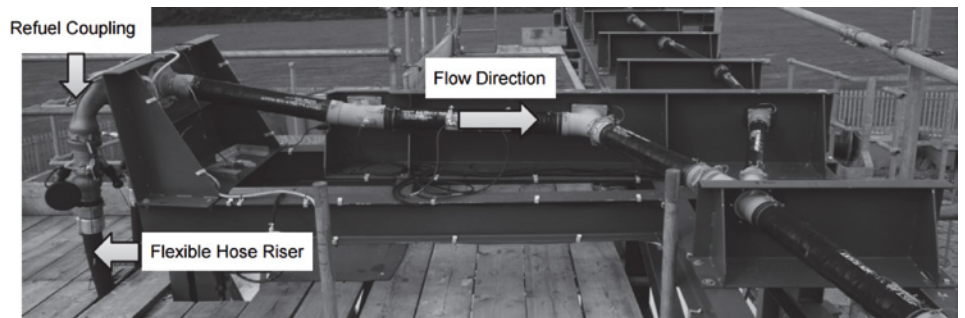


Figure 3. Aircraft refuel test rig, Refuel coupling

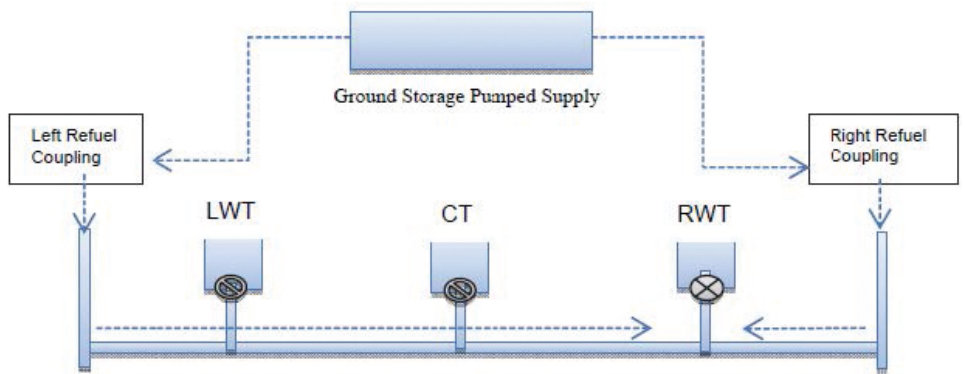


Figure 4. Schematic overview of aircraft refuel rig/1D model

Tank Inlet Valve	Loss Data from Equipment Supplier
Refuel Coupling	Loss Data from Equipment Supplier
Flow Split Junctions	Loss Data from 3D CFD analysis
Bends, Transitions	Internal Flow Systems 2nd Edition
Pipe Losses	Colebrook White Equation

Table 1. Steady state fluid simulation model data inputs

RWT Tank Inlet Valve	Close time from test rig (1.5s)
Refuel Coupling	Fully open throughout surge event
Air In Fuel	Not considered – Single Phase only
Fluid Structure Interaction	Not considered – Rigid Structure
Ground Pump Performance	Pump Curve (Head vs Flow) from Supplier
Pipe Material Properties	Supplier data

Table 2. Unsteady fluid simulation model data inputs

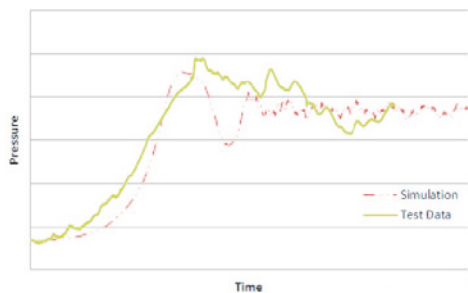


Figure 5. Pressure vs. time plot - left hand refuel coupling

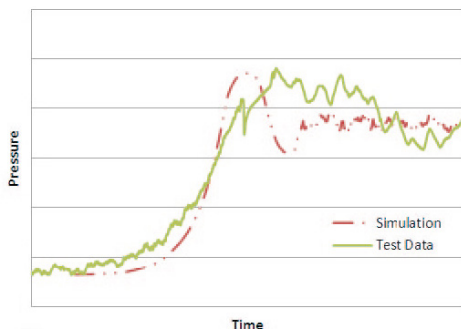


Figure 6. Pressure vs. time plot - Right hand refuel coupling

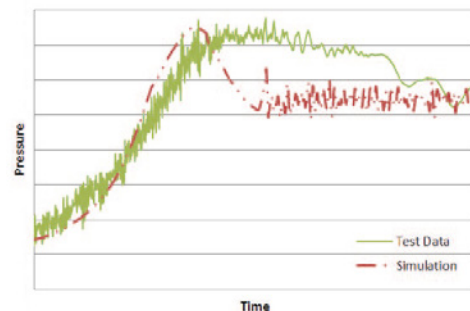


Figure 7. Pressure vs. time plot - upstream of right wing tank inlet valve

as listed in Table 1. Fuel flow rate was not specified in the model. The driving pressure was specified by the supply pump head curve. The Right Wing Tank (RWT) base level total pressure was specified as ambient plus fuel head (average fuel velocity was taken as zero within the tank).

Initial steady state analysis with the above input performance data provided close matching of the refuel rig pressure measurements taken at both refuel couplings and the upstream of RWT inlet valve. This provided confidence that the model was geometrically correct and the validation could progress to the transient scenarios.

Unsteady Flow

For the transient cases, additional unsteady performance data was added to the Flowmaster model as listed in Table 2.

Some additional specifics about the Flowmaster model were that the ground supply pump model, connecting fuel pipework and flexible hose riser, were included in the pressure surge model. No surge attenuation was modeled across components considered to be of a short length or of a rigid structure. Detailed surge behavior across other equipment such as the refuel coupling were unknown and as such no specific surge model was developed. Also, the fluid structure interaction was not modeled. It was felt that this was not necessary since the test rig pipe network was mounted rigidly. Finally, any entrained air in the system was ignored. This again is a reasonable assumption since the entrained air would only have a dampening effect on the system and thereby lessen the possible pressure spikes observed during a surge event.

The transient Flowmaster simulations were then run and compared against the refuel test rig measurements for the pressure vs.

time results. High frequency noise in the test data made it difficult to make an exact comparison of the pressure vs. time results, consequently a degree of smoothing was applied to the test data. For the left hand refuel coupling results (Figure 5), the initial steady state and final stabilized pressures are in close agreement. There is a significant difference in the shape of the rising pressure profiles, where the model appears to have a slower initial response followed by a steeper pressure gradient. There is also an under-prediction of first peak pressure for the simulation.

For the right hand refuel coupling, (Figure 6) the initial steady state pressures are offset by approximately 1.5psid. This offset may result from a pressure imbalance between the left hand refuel coupling and right hand refuel couplings. As discussed above, there is a difference in the shape of the rising pressure profiles where the model appears to have a slower initial response followed by a steeper pressure gradient. Given the differences in the shape of the pressure time profile, the predicted maximum surge values and the final stabilized pressure values are in good agreement.

Pressure vs. time results were plotted upstream of the right wing tank fuel inlet valve, (Figure 7). Similar to the other measurement points, the initial and final stabilized system pressure vs. time results are in close agreement.

Differences in the surge pressure profile may be accounted for as follows: Initially the ground supply pump is delivering pressure/flow to both left and right refuel couplings whereby fuel enters the right wing tank. When the inlet valve closes, the supply flow drops off to zero, at this point the pump moves from its normal operating point to zero flow and max head rise, as indicated by (Figure 7). The exact operation of the supply pump (speed, pressure) during the surge

event was not recorded during the test and has not been modeled. Also, the shape of the test rig pressure vs. time curves (wider bandwidth at maximum pressure) indicate that trapped air may have been present in the closed off fuel lines to the left wing and center tanks and/or significant compliance of the test rig flexible riser hoses. Finally, the first peak over-pressure is defined by the pressure rise above the supply pump stabilized dead head pressure. This shows that a combination of valve closure and pump operation drive the surge over-pressure.

This article has presented the set-up of an aircraft refuel test rig, where the key driver for the test was to verify that the fuel pipework pressures did not exceed the system design limit pressures. Given that refuel test rigs are expensive to develop, operate and cannot be readily modified, this test and simulation, as investigated by the use of Flowmaster, means that the use of full scale tests may be reduced.

References:

[1] Aircraft refuel rig pressure surge modelling and test verification D Morrison, Airbus Operations Ltd, Inerting and Fluid Physics, UK. R Illidge, Airbus Operations Ltd, Fuel & Landing Gear Systems Test, UK. First presented at the BHR Group Pressure Surge Conference 2015.

Cracking Explained

Quantification of Cracked Areas in the Thermal Path of High-power Multi-chip Modules using MicReD Power Tester® 1500A

By Mohammed Amir Eleffendi, Li Yang, Pearl Agyakwa, and Mark Johnson, Department of Electrical and Electronics Engineering, University of Nottingham, UK

Degradation of the thermal conduction path is one of the most common failure mechanisms of power semiconductor packages. Typically, solder fatigue happens due to the thermo-mechanical stresses at the interfacing contacts resulting from mismatched coefficient of thermal expansions between different materials (which make up the heat flow path) and causes cracking. Thermal transient measurement using Mentor Graphics' T3Ster® hardware is a common characterization method for heat conduction path in power semiconductor packages.

The heat flow path in this type of test can be represented by an equivalent electrical Resistance-Capacitance Cauer-type model. T3Ster uses thermal impedance via "structure functions" as a non-destructive evaluation technique to detect structural defects in the heat conduction path. In this work, junction-to-case thermal resistance R_{thjc} and cracked area, from structure functions, are compared to the cracked and unattached area estimated by Scanning Acoustic Microscopy (SAM) for a conventional 1.2 kV/200 A IGBT power module that is actively power-cycled to degrade the solder at the substrate-base plate interface. SAM imaging was performed at regular intervals for multiple stages of the power cycling test to observe the gradual degradation of the solder layer. The Power Module under test (see Figure. 1) was an off-the-shelf 3-phase IGBT module consisting of three substrate tiles mounted on a copper baseplate with two IGBT chips and two freestanding diodes on each [1].

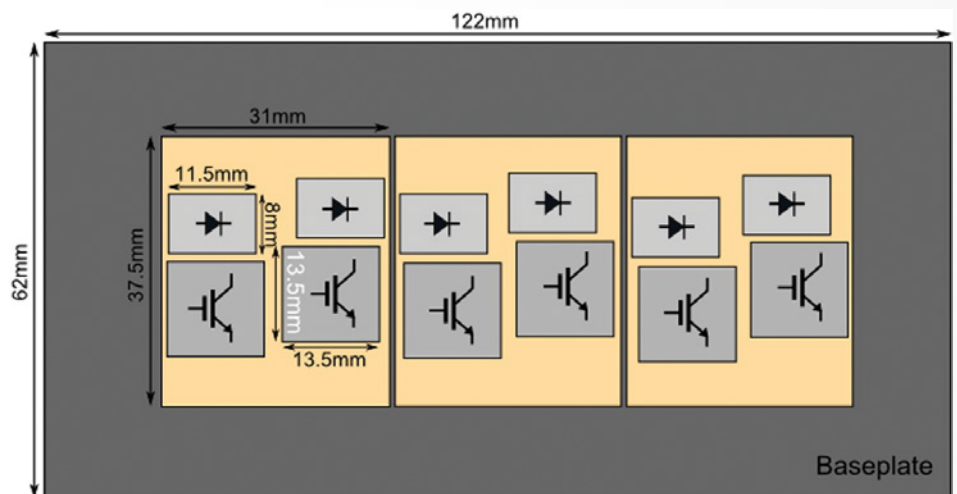


Figure 1. Layout of the Power Module under test (left) with the MicReD Industrial 1500A Power Tester Unit (that contains a T3Ster) used in the Power Cycling Test (right)

The IGBT module was mounted onto a cold plate with a 25 μ m thick Kapton film used as an interfacing material between the cold plate and the baseplate. The purpose of this film was to increase the case-to-ambient thermal resistance in order to achieve a temperature swing at the substrate-case interface and so accelerate the degradation of the substrate mount-down solder layer compared to other failure mechanisms. All IGBTs were biased with a gate-emitter voltage $V_{GE} = 15$ V such that the cycling current I_C as well as the measurement current I_M were shared between the three legs of the module. The collector-emitter voltage V_{CE} is a global measurement across the whole module and therefore, it represents an "average" measurement of the three legs. A

calibration curve $T_J = f(V_{CE})$ at a constant measurement current of $I_M = 200$ mA was used to calculate junction temperature T_J . The cycling current I_C was regulated by the Power Tester to preserve a constant $\Delta T_J = 120$ K with $T_{J \max} = 140^\circ\text{C}$ and $T_{J \min} = 20^\circ\text{C}$ as estimated from VCE with the water temperature maintained at 20°C . The heating time and cooling time were fixed at 50 s, and 60 s respectively. This achieved a ΔT of 70 K at the substrate with $T_{\max} = 90^\circ\text{C}$ and $T_{\min} = 20^\circ\text{C}$. The test started with an initial cycling current $I_C = 236$ A which resulted in a power dissipation $PD = 704$ W. As the thermal resistance increased during the test due to solder fatigue, the cycling current was regulated to keep the ΔT_J constant. Under these conditions, the wire-bond lift-off



Mentor
Graphics

MicReD Industrial
1500A POWER TESTER

mechanism is not the dominant mechanism and the substrate mount-down solder degrades before any wire-bond lift-off is observed. The power cycling was paused regularly every 1000 cycles, at which time a thermal impedance measurement was made of the module in situ by the 1500A Power Tester and this resulted in a total of 17 thermal impedance measurements during the test.

SAM characterization was carried out during the power cycling test using a PVA TePla AM300. Scanning acoustic microscopy is a non-destructive technique that allows us to image the internal features of a specimen and can detect discontinuities and voids of sub-micron thickness. It creates 2D greyscale images from the reflected ultrasonic echoes. Defects at any of the internal layers cause discontinuity in the structure and block the ultrasonic signal preventing it from penetrating through the layers beneath the defected areas. Thus, defects in the substrate solder result in a black shadow appearing in the C scan images taken from the chip level (Figure 2). In this way, the C scan images were used to obtain distinct boundaries between the attached and discontinuous areas. However, the exact location of the defects within the structure can be unclear from SAM images, and therefore, correlative metallurgical cross-sectioning was necessary. The power cycling test was terminated after 17,700 cycles by which time the total junction-to-ambient thermal resistance R_{thja} had increased by 14% from its original value. After examination, all IGBT devices were still electrically functional. Following the final SAM observation, metallurgical cross-sections were prepared and examined under an optical microscope in order to confirm the degradation mode.

The IGBT module was imaged in its original state, i.e. prior to power cycling. No cracks or voids were observed in the internal layers at that stage (Figure 2). The power cycling test was interrupted for SAM imaging at 9100, 10,450, 13,350, and 15,500 cycles. At 17,700 cycles, the test was terminated and a final scan was performed. The percentage of attached area was calculated as $\text{Attached Area (\%)} = \text{Number of White Pixels} / \text{Total Number of Pixels}$. Figure 3 shows the estimated attached area of the solder layer at different cycle numbers during the cycling test. At zero cycles, the attached area was estimated to be 93%. This is because the processing algorithm recognizes the separation lines between different

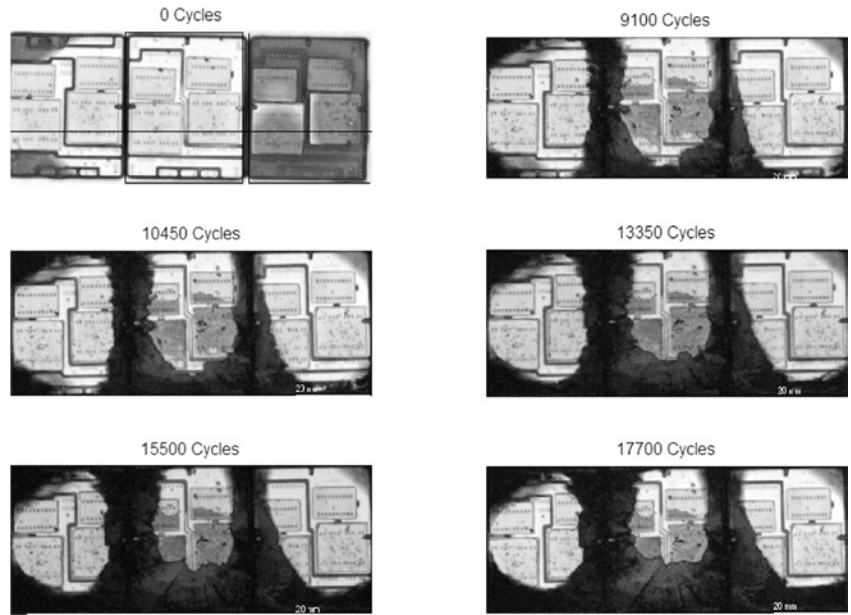


Figure 2. Scanning Acoustic Microscopy (SAM) images at different cycles during the power cycling test.

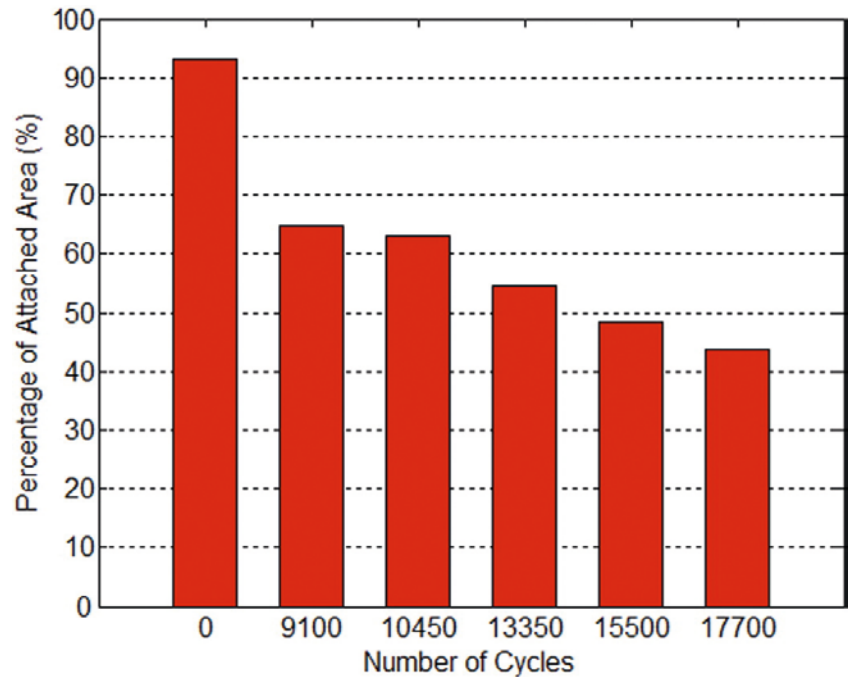


Figure 3. Estimated attached area of solder layer during the cycling test from SAM images.

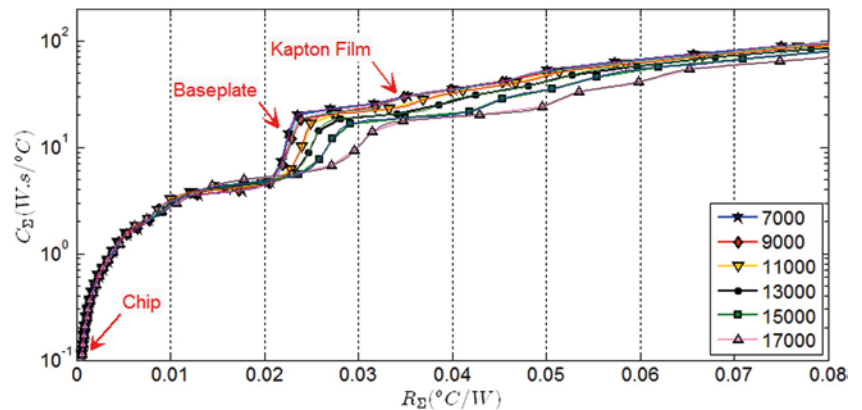


Figure 4. Cumulative T3Ster structure function showing different layers of the thermal stack as number of cycles increase



substrates and between copper traces and the wire bond footprints as black (cracked) pixels. However, this feature does not affect the observed trends as it is persistent in the remaining images. As the number of cycles increases, cracking propagates through the solder causing the attached area to be reduced gradually until it reaches 43% attached area after 17,700 cycles.

Figure 4 shows that a change develops in the structure function as the number of cycles increases. This change appears as an increasing thermal resistance since the curve is shifting to the right over the x-axis with the increasing number of cycles. The change starts at the interface between the base-plate region and substrate where an expansion over the x-axis can be spotted. However, it is difficult to conclude from this plot alone exactly where in the solder interface region the cracking is happening.

The junction-to-case thermal resistance R_{thjc} can be measured from the structure function at the end of the baseplate region and before the start of the Kapton film region. Figure 5 shows R_{thjc} as a function of number of cycles. It can be seen that R_{thjc} stays unchanged until 8000 cycles, and from this point onwards it increases progressively until the end of the test. The total increment in R_{thjc} is about 70% from its original value which is estimated as $0.024^{\circ}\text{C}/\text{W}$. This increment is a result of cracks in the solder at the substrate-base-plate interface which is confirmed by metallurgical cross-sectioning as shown in figure 6.

Figure 5 also shows values of R_{thjc} measured at 7000, 9000, 11,000, 15,000, and 17,000 cycles plotted as a function of the percentage of attached area as estimated from the SAM images of figure 2. It can be seen that as the attached area decreases the thermal resistance increases rapidly. It is also noted in figure 5 that the sensitivity of the structure function for structural defects is dependent on the location of the semiconductor chip relative to the location of the defect. That is, it has higher sensitivity for defects located directly below the chip such that the defect has a direct thermal effect on the chip, whereas a defect located far from the chip would result in lower sensitivity of the structure function for that defect. That is the reason why no change in the structure function is seen until 35% of the substrate-case solder layer is cracked through. Cracking of the solder starts at the corners of the substrate and initially this has little effect on the heat

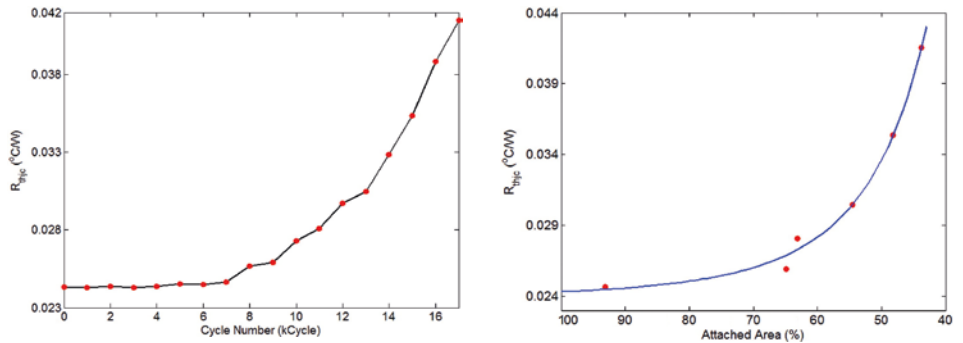


Figure 5. The change in the junction-to-case thermal resistance R_{thjc} during the power cycling test as a result of solder fatigue and how it correlates to the cross sectional attached area of the layer.

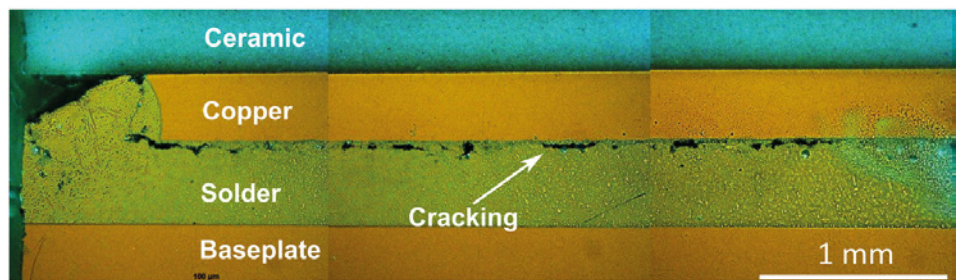


Figure 6. Image of metallurgical cross-section showing the cracking resulting from power cycling at the substrate-baseplate interface.

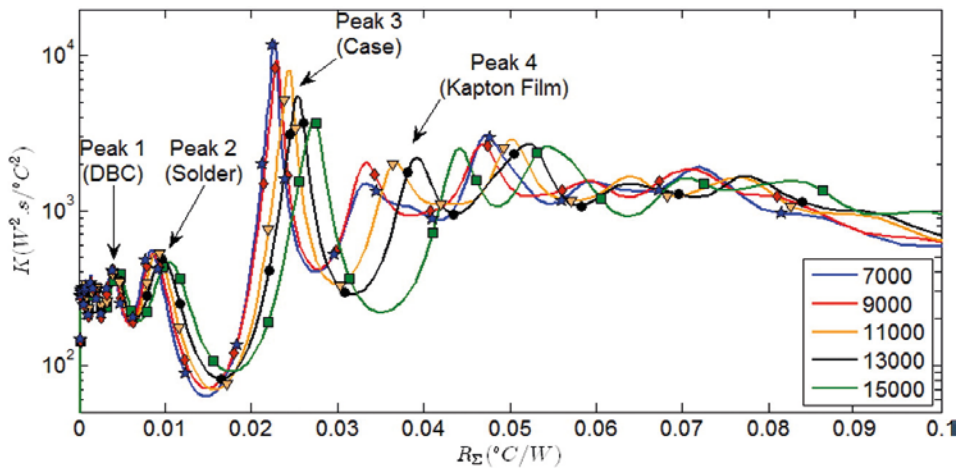


Figure 7. T3Ster differential structure function during the power cycle test. Different peaks indicate different layers (as shown)

flowing from the semiconductor chips towards the heatsink. With propagation of the cracking towards the center of the substrate, the heat flow is obstructed and only then does the structure function start to indicate the presence of a defect. Figure 7 shows the T3Ster differential structure function $K(R_{\Sigma})$ between 7000 cycles and 15,000 cycles. Each peak in this plot indicates a new layer of material with a different cross-sectional area. A decrease in the amplitude of a peak indicates a reduction in cross-sectional area of the layer related to that peak. The shift in the location of the peak along the

x-axis indicates a change in the thermal resistance of this layer. Hence, the thermal resistance of the individual layers can be identified. In addition, the thickness can be identified if the material properties are known. The most significant peak is Peak 3, which is related to the baseplate layer. The other peaks are shown related to the different materials heat is flowing through. The most significant changes can be seen in the amplitude of Peaks 2 & 3, which are decreasing. Peak 1 and Peak 4, on the other hand, remain at almost constant amplitude. This decrease in the amplitude signifies a reduced cross-sectional area of

the solder layer which is at the interface between the DBC substrate and the baseplate. This is accompanied by an increase in the thermal resistance of the solder layer which is indicated by a shift in the location of Peak 2 and Peak 3 along the positive x-axis.

The K-value of Peak 3 (that is, the Case) from the T3Ster differential structure function (Figure 7) can be plotted against the number of cycles and this is shown in figure 8. A decrease in the K-value is clear as the number of power cycles increases, and is indicative of reduced cross-sectional area. In order to reveal the relationship between the two quantities, the cross-sectional area estimated earlier from the SAM images was compared to the K-value given by a differential T3Ster structure function. This is correlated in figure 9 where the K-value can be seen to be linearly related to the cross-sectional area squared. This is in agreement with theoretical relationships we have evaluated [1] and is an important finding of this study.

If we now look at the individual IGBTs in our module under test, all were functional after 17,700 power cycling tests. At this point in the test, the SAM image showed different levels of discontinuity beneath the individual IGBT devices. Therefore, an investigation was carried out to examine whether this non-uniformity in heat flow can be observed in the structure functions for the individual IGBT chips in addition to the module as a whole. For this study, thermal paste was used as the interface material instead of the Kapton film used during the power cycling test. The local thermal impedance of each individual IGBT in the module was measured and the structure function was calculated. The attached area under each individual IGBT is estimated from the SAM image at 17,700 cycles and these are shown in figure 10. The IGBT devices were numbered from 1 to 6 and the area under each IGBT was cropped to calculate the attached area using a MatLab™ methodology [1].

The estimated percentage attached area under each device is shown in figure 11 with values from lowest to highest being Device 4, followed by Device 2, then Device 3, Device 5, Device 6, and finally Device 1. Figure 11 also shows the cumulative structure function for the individual IGBTs. A large difference can be seen between the curves as a result of the different levels of discontinuity in the substrate to baseplate interface area

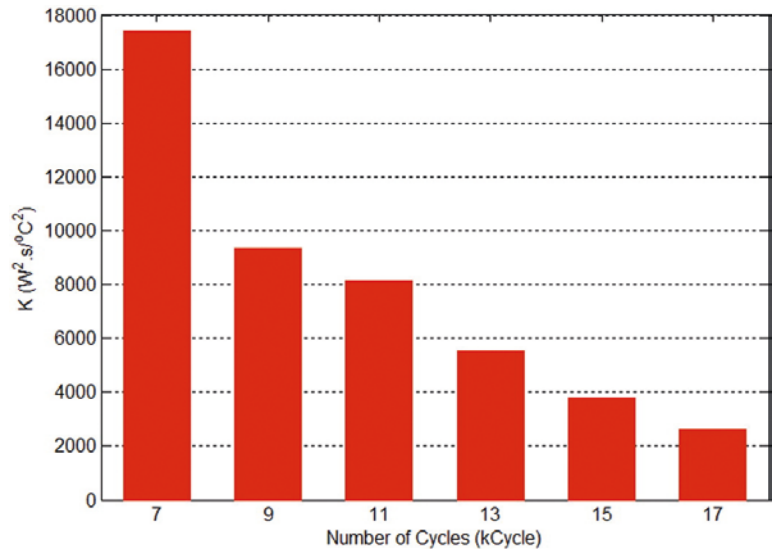


Figure 8. K value of the case region shows a steady decline over the power cycling test indicating a decreasing cross-sectional area.

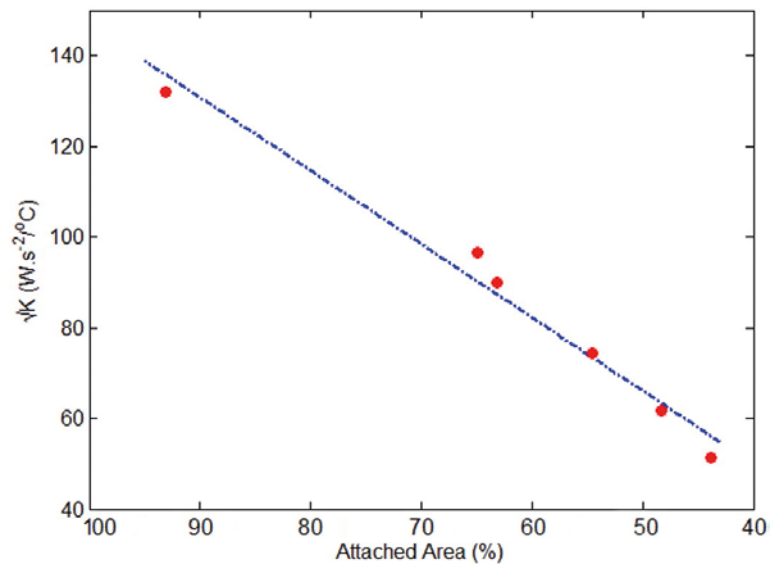


Figure 9. K value given by the differential structure function at the baseplate region – it has a linear correlation to the square of the fractional cross-sectional area of the solder layer.

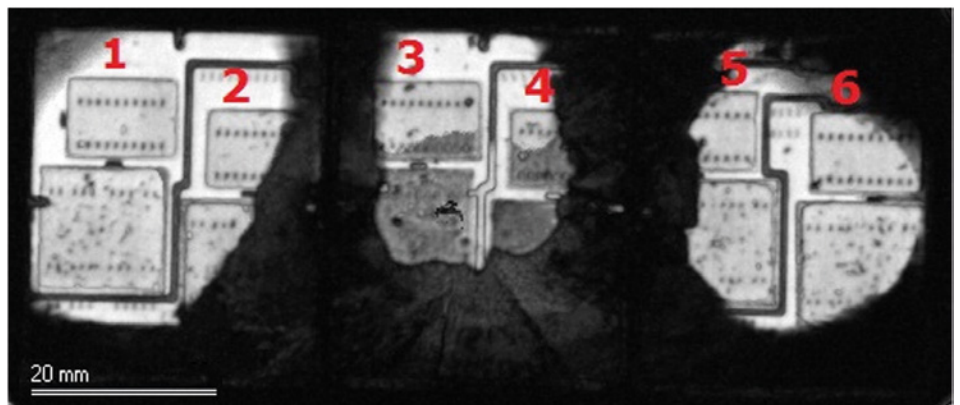


Figure 10. SAM image of the cycled module at 17,700 cycles shows different levels of delamination under the 6 IGBT devices.



below each IGBT. The different thermal layers can be most easily identified on the curves related to Device 1 and Device 6 as they are the least affected by solder fatigue. Features of the different layers in the structure start to disappear as the level of local delamination increases in the other devices. Device 4 is the worst affected by cracking and its different layers' features cannot be distinguished. Hence, we concluded that the junction-to-ambient thermal resistance R_{thja} may be directly compared with the percentage of attached area below the individual IGBTs.

Figure 12 shows R_{thja} of the individual IGBTs as a function of attached area of the solder under each IGBT. Similar to the result shown in figure 5, it can be seen that the R_{thja} can be correlated to the attached area. If we also produce and plot K-value against the square of the percentage of attached area, figure 13 shows yet again a clear linear correlation can be deduced with K-value being a function of the square of the fractional attached area of each individual IGBT.

Conclusions

An evaluation using MicReD T3Ster structure functions within a Mentor Graphics 1500A Power Tester as a non-destructive testing tool for examining the integrity of the heat flow path in high power multi-chip semiconductor modules under repeated cycling has been carried out. A 1.2 kV/200 A IGBT power module (with six IGBTs) was power cycled to activate the solder fatigue failure mechanism at the substrate-baseplate interface. Thermal impedance measurements and SAM imaging were performed at regular intervals during the power cycling test. From this data, the thermal structure function was calculated and the cracked area in the solder layer was estimated. Failure analysis by cross-sectioning confirmed the location of the discontinuity at the substrate-baseplate solder layer. A clear correlation was found in this study between the change in the junction-to-case thermal resistance R_{thjc} estimated from the structure function and the remaining attached area of the solder layer calculated from SAM images. It was shown that the K-value obtained from the differential structure function was linearly related to the square of the percentage of attached area estimated from SAM images. Similar results were found for the structure function calculated from the local measurement of the thermal impedances of individual IGBT devices in the module. Hence, the MicReD 1500A Power Tester

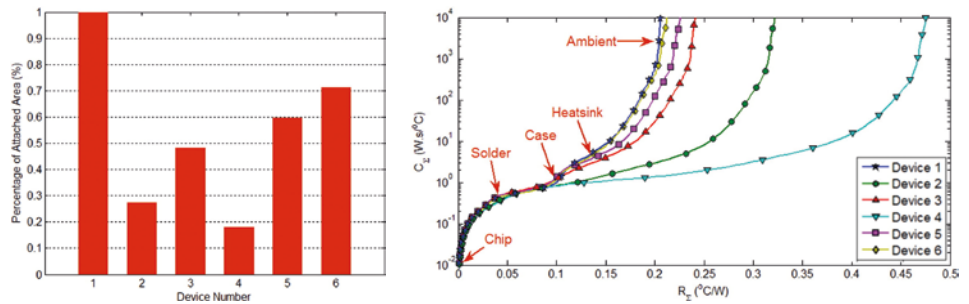


Figure 11. Percentage of attached area local to the IGBT devices and the cumulative structure function of each individual IGBT device after 17,700 cycles.

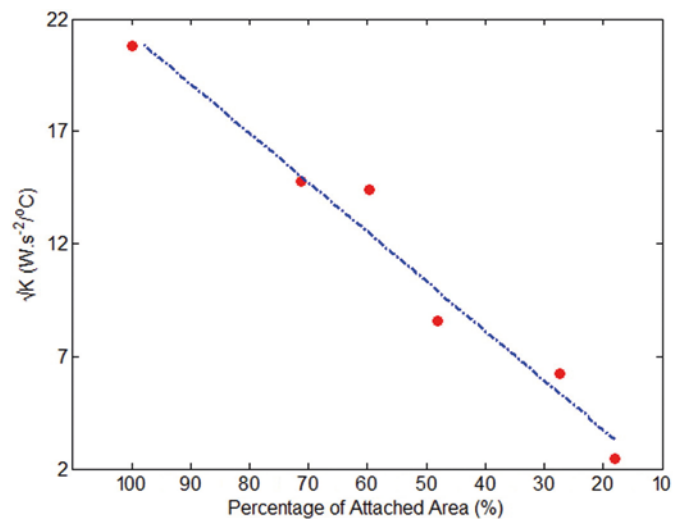


Figure 12. The junction-to-ambient thermal resistance R_{thja} of the individual IGBTs after 17,700 cycles as a function of the attached area below each IGBT.

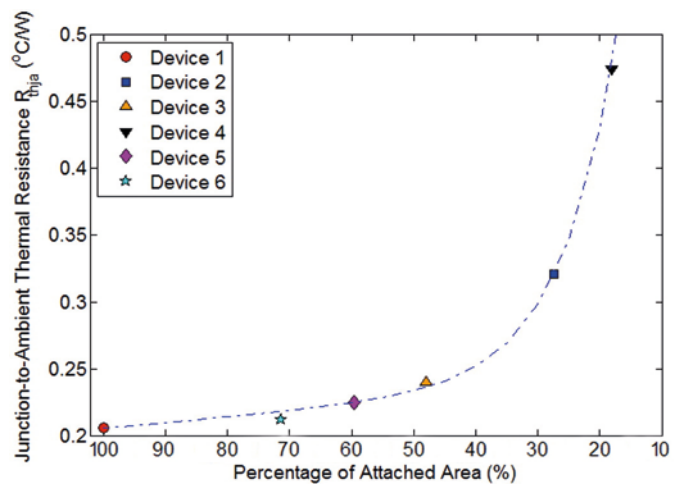


Figure 13. K-value as a function of the square of the fractional attached area of the individual IGBTs.

and its structure functions can be used to estimate degradation in specific layers of a power module and individual devices non-destructively. Consequently, it can be used as a primary inspection tool to rapidly test the integrity of heat flow path in power modules before deciding whether further, but potentially time-consuming alternatives like SAM, or destructive analysis is required.

References

- [1] M.A. Eleffendi, et al., "Quantification of cracked area in thermal path of high-power multi-chip modules using transient thermal impedance measurement", *Microelectronics Reliability* (2015), <http://dx.doi.org/10.1016/j.microrel.2016.01.002>





Early Stage Analysis of Electric Vehicle Power Electronics Liquid Cooling System Designs

By Heesung Park, Associate Professor, Department of Mechanical Engineering, Changwon National University, Korea

The desire for the automotive industry to shift to more fuel efficient and environmentally friendly technology has grown significantly in recent years. While several innovations have taken the industry to a better place of lower emissions and fossil fuel consumption through the development of hybrid electric and plug-in electric vehicles, technically the market is moving towards vehicles that could satisfy the demand for zero hydrocarbon emissions and not require an external electrical power supply for charging. This goal is currently being pursued through the use of fuel cells to generate the energy needed to get our society where it wants to go both literally and figuratively.

The idea of fuel cells is nothing new; it is simply harnessing the electricity that is generated by the chemical energy from the reaction of hydrogen ions with oxygen. The challenge is implementing this technology on a scale that can generate enough energy to move a vehicle safely and efficiently. One aspect that is of particular concern is the heat generated due to the inefficiencies involved with the process. Considering a vehicle that is powered up to 100kW with a typical conversion efficiency of 90% in the power electronics, this would require up to 10kW of heat to be handled by the cooling system so that there aren't any issues. Traditional air cooling devices have been used in low heat dissipating electronics successfully but when faced with electronics that have high energy densities, another form of cooling is required.

For these designs, liquid cooling has an advantage over air, due to its higher heat capacity and thermal conductivity. As a

result, significant research has gone into different methods to enhance the cooling performance of liquid systems. When looking at liquid cooling there is a need to evaluate not only the cold plates that will be directly extracting the heat from the electronics but the entire system. Since it is a closed system the performance will also depend on the pressure drop through piping and fittings, performance of the pump, and the fluid and thermal characteristics of the radiator. For this reason a combination of three dimensional (3D) and one dimensional (1D) Computational Fluid Dynamics (CFD) software was used to analyze systematic cooling performance. The approach is especially effective and informative during the early stage of the conceptual design before other design decisions have been made.

In fuel cell electric vehicles the electrical flow is sent through several different power electronics, each of which needs to be cooled. For the analysis, each of the power electronics has its own cold plate and the estimated heat rejection was based on a 100kW vehicle with 90% efficiency. The components include: a high voltage junction box (HVJ), a motor control unit (MCU), an auxiliary control driver (ACD), high and low voltage DC/DC converters (HDC, LDC), and a motor. The cooling system comprises cold plates for each electrical component, a coolant pump, a radiator, and piping. The heat dissipation rates and thermal design points for each of the electrical components are shown in Table 1.

The need to design a cooling system to meet the heat dissipation requirements of the power electronics is best carried out using a 1D CFD tool such as Flowmaster, since its focus is on system level performance. However, to accurately model a system in 1D CFD, the software requires performance characteristics of the different components that make up the system. There are several sources for generic loss or heat transfer data, but since the design information for the components was available, the use of 3D CFD meant a potentially more accurate solution if the two were combined.

For this reason each of the electrical components (Figure 1) were run through a series of steady state analyses with heat transfer to characterize the pressure drop (Figure 2 (a)) and maximum temperatures as a function of liquid flow rates (Figure 2 (b)). The pressure drop was then converted to a loss coefficient for use in Flowmaster. The same process was followed for the piping, though this was assumed adiabatic, and for the radiator. For the pump, the performance curve was plotted by measuring the pressure

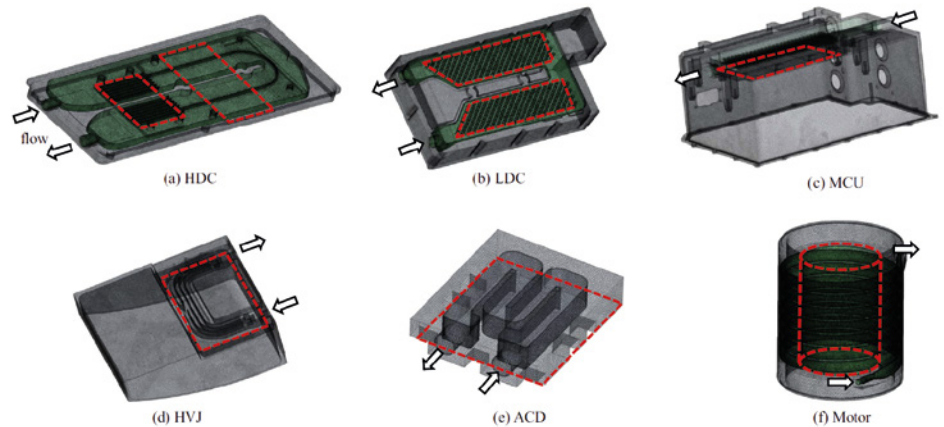


Figure 1. Geometries of the electrical components. The dotted lines indicate the thermal boundary conditions to simulate the heat generations

	HDC	LDC	MCU	HVJ	ACD	Motor
Heat dissipation rate (W)	650	320	1800	450	500	6600
Heat flux (W/cm ²)	3.3	6.4	12.7	0.6	4.3	5.7
Thermal design point (°C)	85	85	85	85	85	120

Table 1. List of the maximum heat dissipation rates and thermal design points of the electrical components

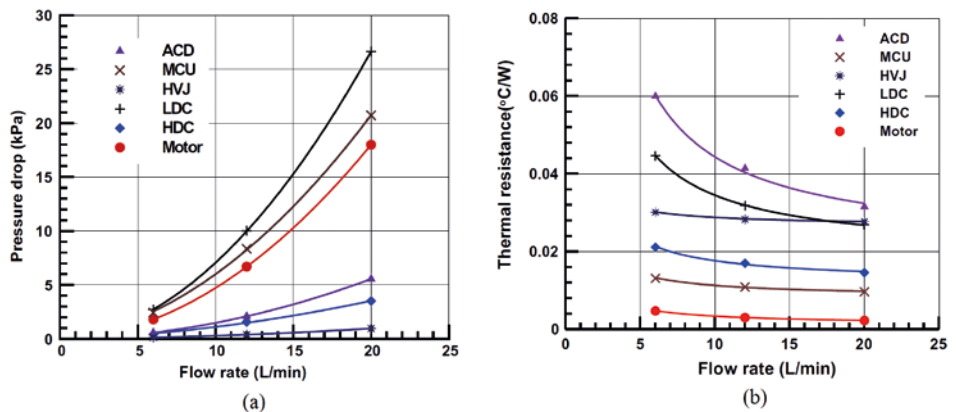


Figure 2. The calculated pressure drops of the cold plates (a) and the calculated thermal resistances of the electrical components (b) with respect to the flow rates of 6, 12 and 20 L/min.

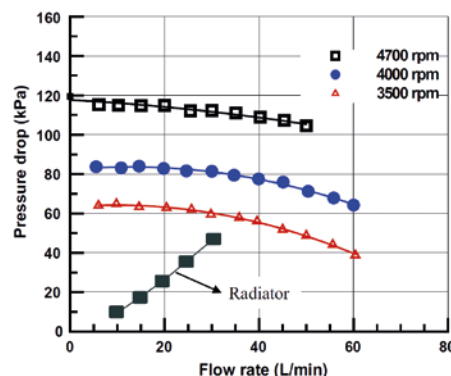


Figure 3. Characteristic curves of the liquid pump and radiator.

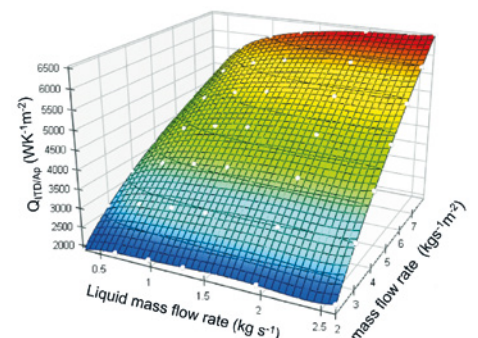


Figure 4. Cooling performance surface map of the radiator.



rise versus volumetric flow rate at three different rotational speeds and is shown in Figure 3 with the radiator pressure drop. For the thermal characterization of the radiator, a surface map of (q_{TDA}/A_p) versus coolant flow rate and air flow rate was entered into Flowmaster which can be seen in Figure 4.

With the characteristic data for the components available, it allowed different potential configurations to be analyzed. In Figure 5, there are three cases that were studied. Case 1 was a single loop with all components in series of each other, while in Cases 2 and 3 there are parallel coolant paths with the main difference being the order of the electrical components. This allowed for three different pump speeds, two different inlet air flow rates, and one inlet air temperature for each of the physical configurations.

Investigating the results using the maximum pump speed of 4700RPM and maximum inlet air flow rate of $8 \text{ kg s}^{-1} \text{ m}^{-2}$, Figure 6 shows the calculated flow rates and pressure drops for all of the cold plates. Figure 7 shows the maximum resulting temperatures and inlet liquid temperatures of the electrical components and it can be seen that the highest cooling performance can be obtained using the Case 3 configuration. The temperatures can also be used to theorize other configurations that could be more optimal such as placing the higher heat dissipating MCU and motor downstream of the cooling system to minimize the inlet liquid temperature rise of the cold plates.

It is also important to note the heat rejection capabilities of the radiator in the system in this study, 9.0, 9.5, and 10kW for Case 1, 2, and 3 respectively. This value is significant since the power of an electric vehicle fuel cell is limited by its capacity for rejecting the heat of the electronics. Figure 8 shows the effect of the heat rejection from the radiator for each of the cases. As seen, a cooling system that cannot handle the required heat rejection of the electronics can actually act as a bottleneck for the vehicle.

The use of 1D-3D CFD meant the cooling system for this electric vehicle fuel cell could be evaluated early in the design phase so that decisions could be made before any physical prototypes or testing needed to be done. We were able to eliminate a potentially costly failing design and focus time and resource to optimizing a solution for the cooling systems.

Reference:

[1] Numerical assessment of liquid cooling system for power electronics in fuel cell electric vehicles Heesung Park, Research and Development Division, Hyundai Motor Company, 104, Mabuk-dong, Yongin-si 446912, South Korea

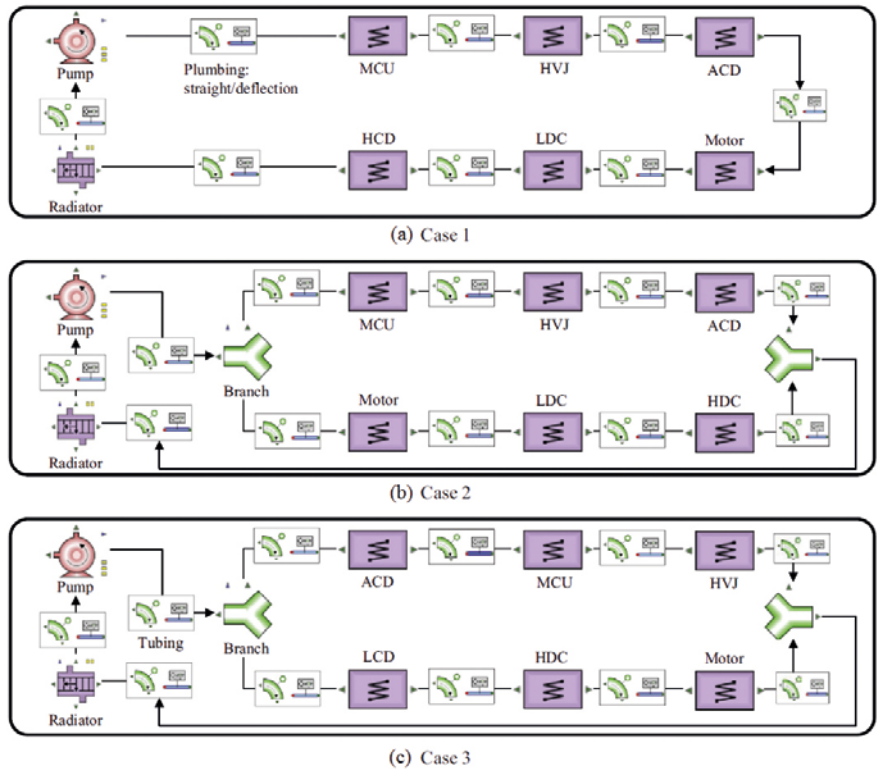


Figure 5. Flowmaster configurations of the liquid cooling loops.

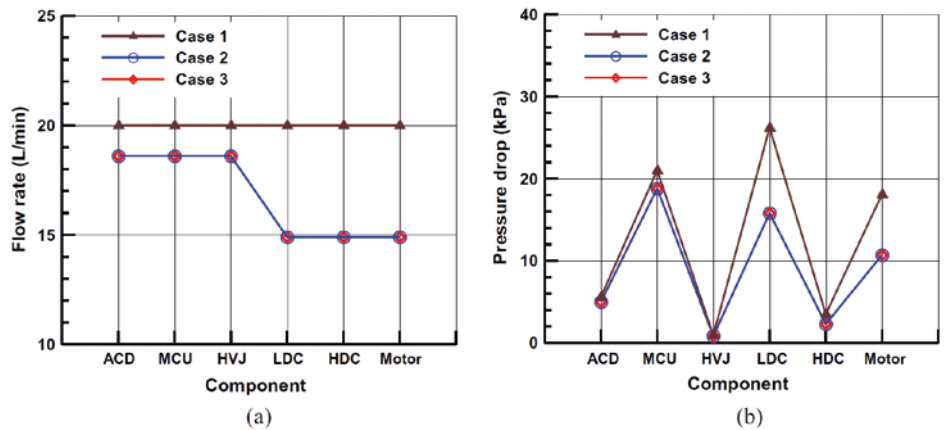


Figure 6. 1D numerical simulation results for the flow rate (a) and the pressure drop (b).

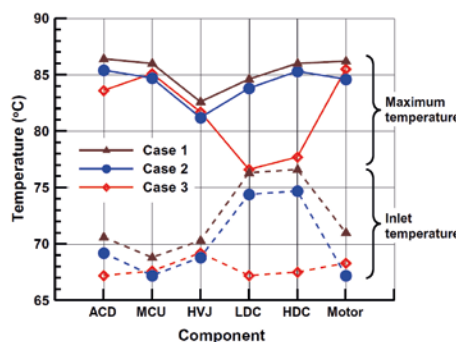


Figure 7. Maximum temperatures of the electrical components as predicted by the 1D and 3D numerical simulations.

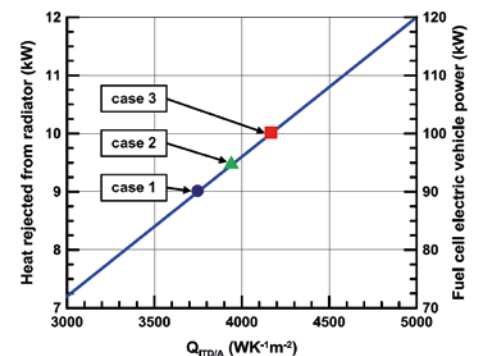


Figure 8. The limited power of fuel cell electric vehicle induced by heat rejection capacity of the radiator.

Simplifying Modeling Challenges in Complex Networks



By Katherine Tupper, Application Engineer, Mentor Graphics

In Flowmaster® it is possible, and often beneficial, to simplify a many component network and still maintain the physical phenomena. The user should carefully consider which areas can be simplified and which areas of the system need to be modeled in detail.

For example, in processing plants the long complex pipelines can be modeled in various ways and the most appropriate method will depend on what effects the user is looking into. For those looking at the pressure surge after a valve shut off, it is important to model the pipes in the network elastically.

Flowmaster uses the 'S' criteria to determine which pipes to model elastically where:

$$S = \frac{L}{a\Delta t} \geq 3$$

L is the pipe length, Δt is the timestep and a is the pipe and fluid wavespeed [1].

Building a detailed network with all the pipes and fittings that are present in the plant, an example of such a network is shown in Figures 1 and 2 and contains 315 components.

With this detailed network a small timestep, of the order 0.0007s is needed to ensure Flowmaster treats all the pipes as elastic. This meant that the simulation time was greater than 30 minutes and created a result file larger than 2GB. With such a large results size, running multiple simulations with this network would quickly fill a database.

In some transient cases it can be appropriate to increase the "file write interval", which is an option in "Output Control" under the "Simulation Data" tab. This functionality means the user can store every nth iteration

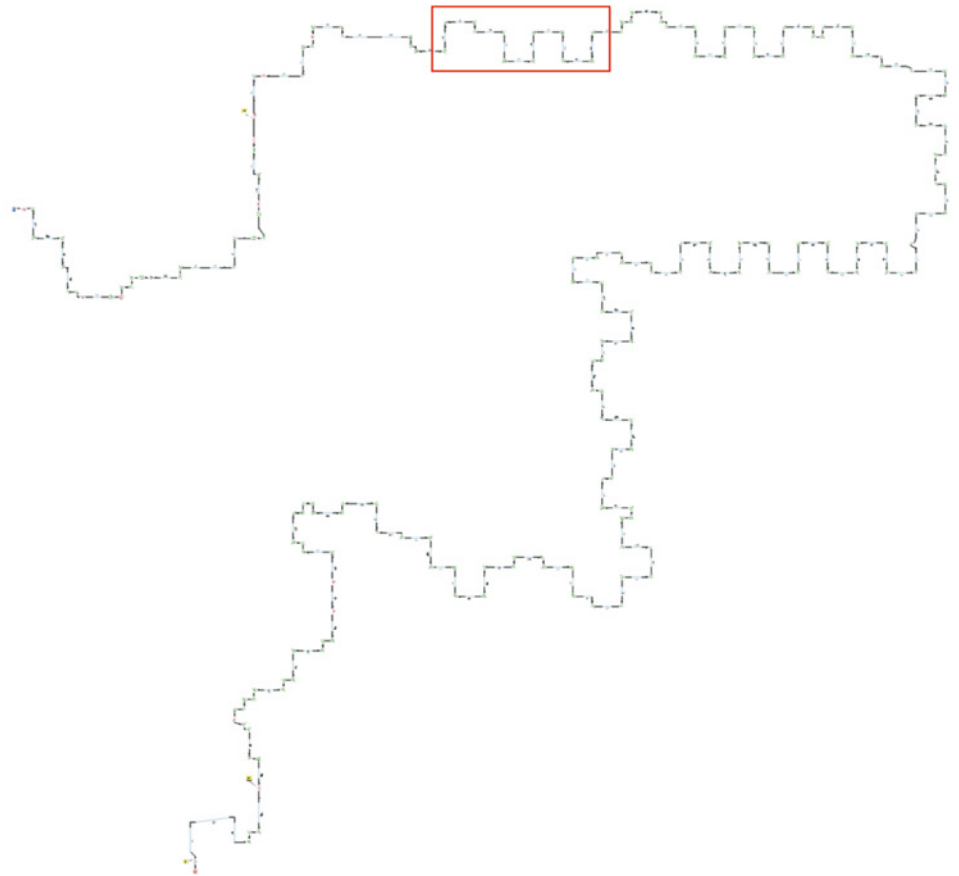


Figure 1. Detailed Network

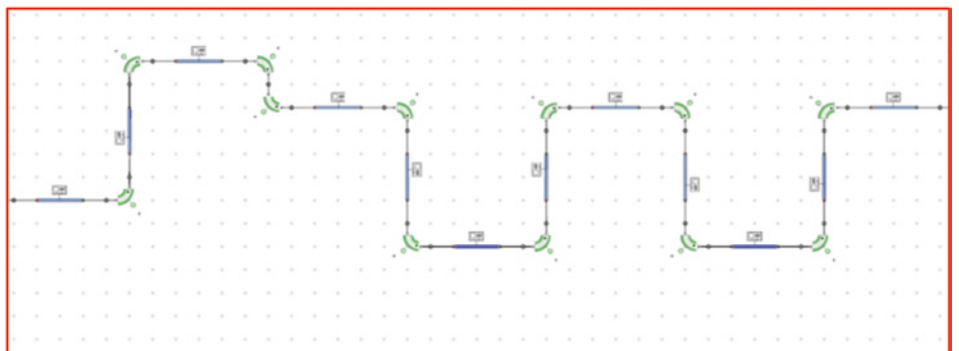


Figure 2. Close up of highlighted section of pipeline

result and thus reduce the results file size. However, caution must be exercised as it is possible to miss important results or the finer detail in a rapidly fluctuating system. If the maximum pressure in a system occurs at a timestep that is not stored, it is not possible to recover this information.

If you were to increase the file write interval to 10 or 100 then the simulation time reduces to four minutes and two minutes respectively, with results file sizes of 0.2GB and 0.02GB. The peak pressures reported in this system are reduced with the change in file write interval, see figure 3.

Therefore for systems such as the plant line, simplifying the network will yield a smaller results set and quicker simulation time.

A large section of the pipeline (pipes and bends) can be replaced with a single pipe of equivalent length. Figure 4 highlights the section that is replaced by the single pipe, with the simplified network shown in figure 5. When using a single pipe to represent all pipes with fittings, it is necessary to increase the roughness settings of the pipe to take into account the bend losses.

In Flowmaster it is possible to insert pipe points along the length of a pipe and manipulate the shape of the individual pipe so that it resembles the complex pipe and bend system as shown in figure 6.

This simplified network has only 85 components so there are automatically less results to store. Having the longer pipes means the timestep can be increased whilst maintaining the elasticity of the pipes. With less components and a 3.5 time larger timestep, this simulation takes one minute to solve and the results file size is less than 0.2GB, without losing the detail of the pressure fluctuations. Figure 7 shows how the results compare between the detailed and simplified networks. There is a difference in the pressure surge behavior between the two models, which leads the user to check if the physical effects are being accurately modeled in each network.

In both the detailed and simplified networks, Flowmaster's auto-vaporization capability is used to show where cavities form and collapse. However, if there is a cavity when the simulation initializes there is not enough information for Flowmaster to model this correctly, which is the case here as there is a high point of the loading arm. The assumption is that the initial volume is zero and that the cavity is growing. In the processing plant, the cavity would drain the arm from the high point until the residual

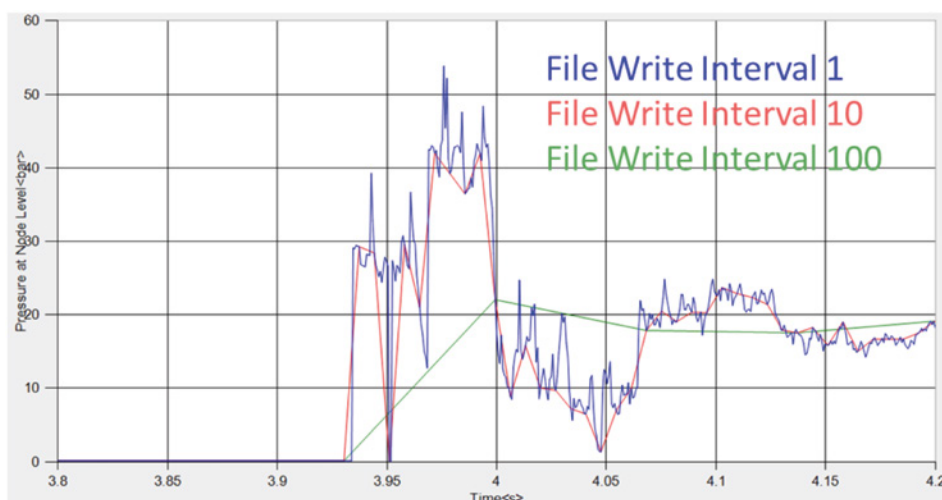


Figure 3. Pressure results

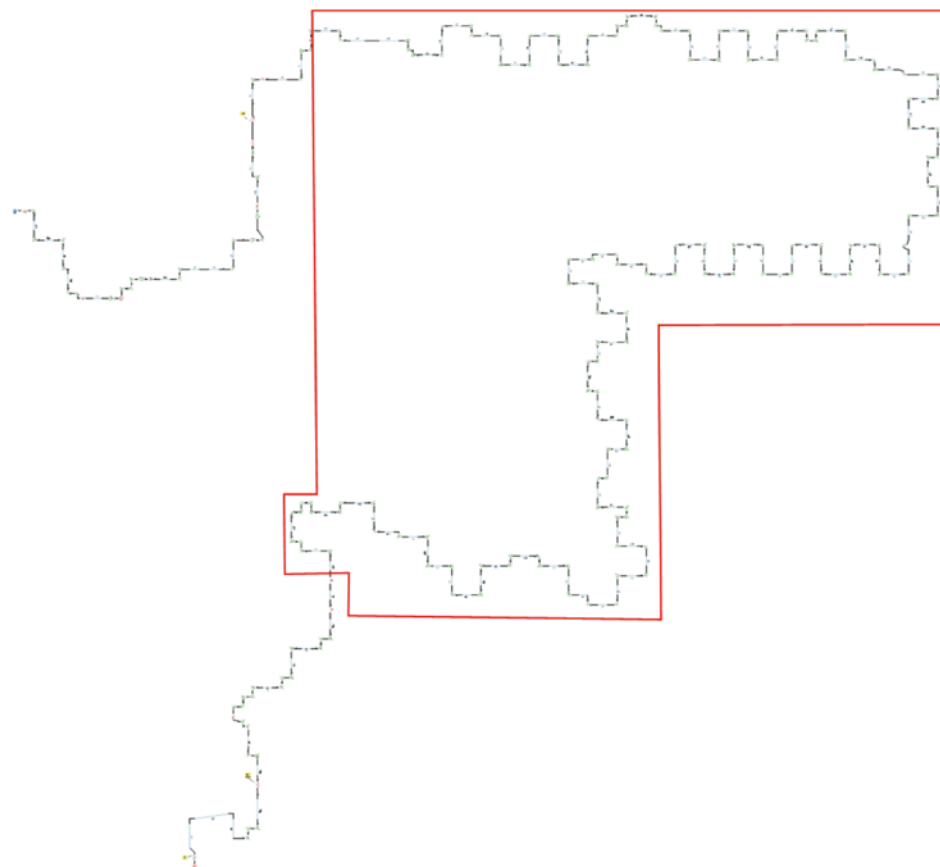


Figure 4. Section to be replaced

head was just enough to maintain the same flow out of the arm as is entering it.

In this pipeline the pressure surge due to the collapse of this cavity, after a valve closure, is the worst case scenario for the processing plant. Therefore the cavity collapse needs to be modeled more accurately by giving Flowmaster corrected initial conditions. A gas admission valve is added to the

simplified network, with an initial gas volume which matches the cavity volume. A valve with blank end is also needed as the gas admission valve cannot be attached to a node with auto-vaporization but auto-vaporization is required at this high point of the loading arm, in order to set the pressure correctly at the start of the simulation. Figure 8 shows the original loading arm set-up and the modified network.

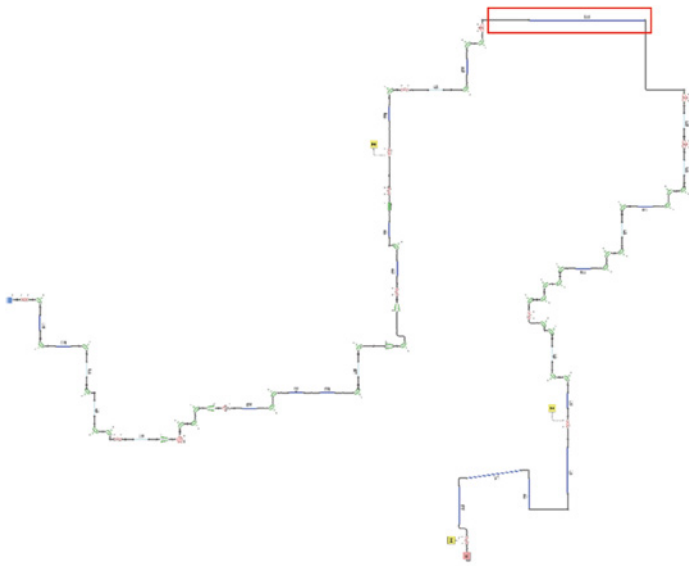


Figure 5. Simplified Network

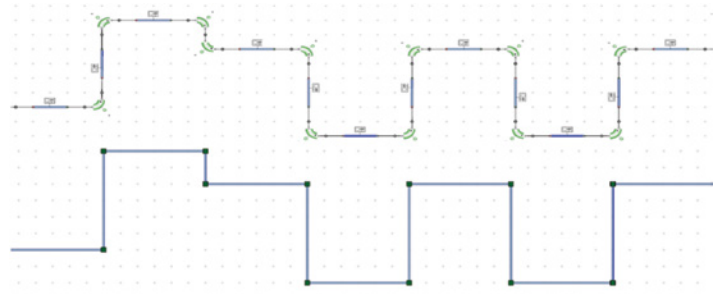


Figure 6. Pipe configuration

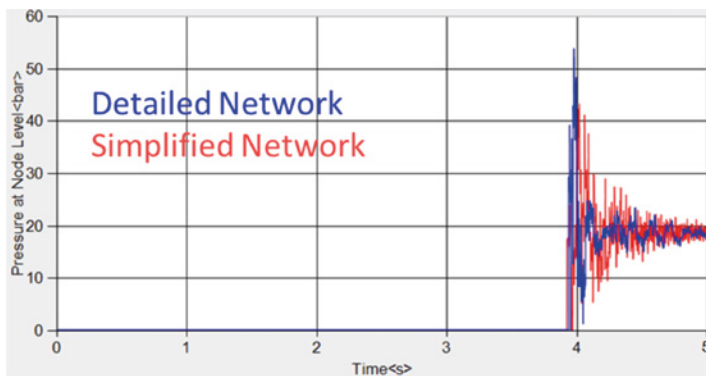


Figure 7. Pressure Results

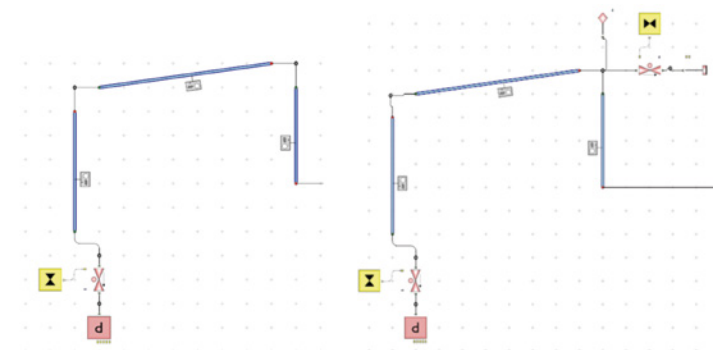


Figure 8. Loading Arm

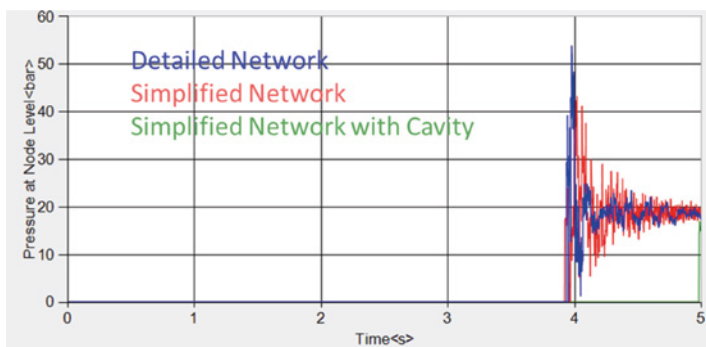


Figure 9. Pressure Results

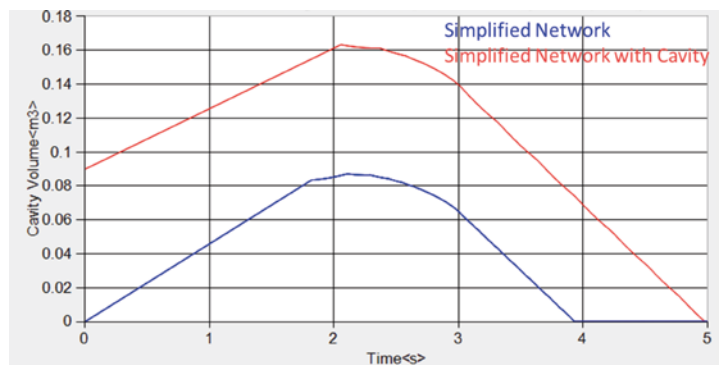


Figure 10. Cavity Volume

The pressure results from this simplified network with cavity modeling are shown in comparison with the previous network results in Figure 9. The peak pressure is reduced and delayed compared to the networks without the gas admission valve. More accurate modeling of the initial cavity collapse gives the pressure surge as it would occur in reality.

Simplifying a processing plant pipeline from many pipes and bends into a single pipe allows the user to focus on accurately modeling the area of the system where the highest pressure peaks are experienced. In this case the run time of the network is over 10 times quicker and the results size is 10 times smaller, giving the user more time to analyze the results and run multiple design scenarios.

References:

- [1] 'Fluid Transients in Systems', Wylie & Streeter, Published by Prentice Hall 1993, (ISBN 0-13- 322173 -3.)



Consumer Electronics Miniaturization:

Thermal Analysis of a Small Outline Package Mounted on a PCB Using Computational Fluid Dynamics

By Robert Day, Senior Application Engineer, Analog Devices; and Prasad Tota, Application Engineer, Mentor Graphics Corp.



The trend towards miniaturization in the consumer electronics industry has driven package component sizes down to the design-rule level of early technologies. Crucial in integrated circuit (IC) package technology is that it must deliver higher lead counts, reduced lead pitch, minimum footprint area, and significant volume reduction. As a result, this has led to semiconductor manufacturers developing the small outline package (SOP), surface-mount memory packaging.

SOP packages consume one-third to one-half of the volume of earlier packaging alternatives and are a logical choice for the small form factor of handheld electronics, portable communication devices, laptop and notebook PCs, disk drives, and other applications. Power SOP (PSOP) packages, when combined with a heat spreading thermal mass (copper slug), make the resulting dimensions an ideal good choice for office automation, industrial controls, networking, and consumer applications that generate internal heat and are exposed to stressful temperature conditions.

To simplify board layout PSOPs can be placed much closer together and to other components as they are designed with their leads located on the long side of the package, leaving two sides of the package open. The open sides of the package can be used to route traces under the component, conserving board layers.

Thermal power density increases when IC packages are downsized, driving the need for heat-transfer path from the die to the external ambient to be optimized to allow for maximum possible power dissipation at the die while ensuring the die temperature is under the maximum allowable value.

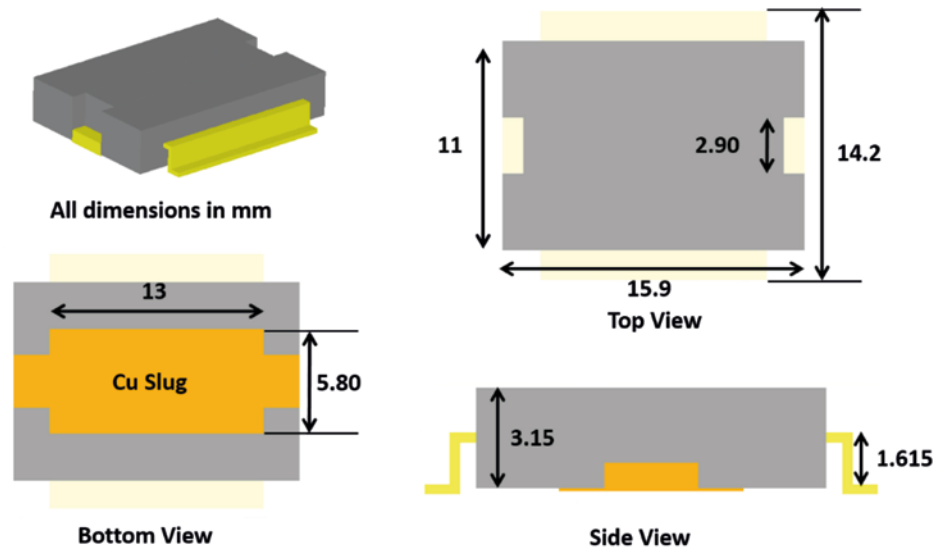


Figure 1. The PSOP dimensions in millimeters, with the copper slug on the bottom.

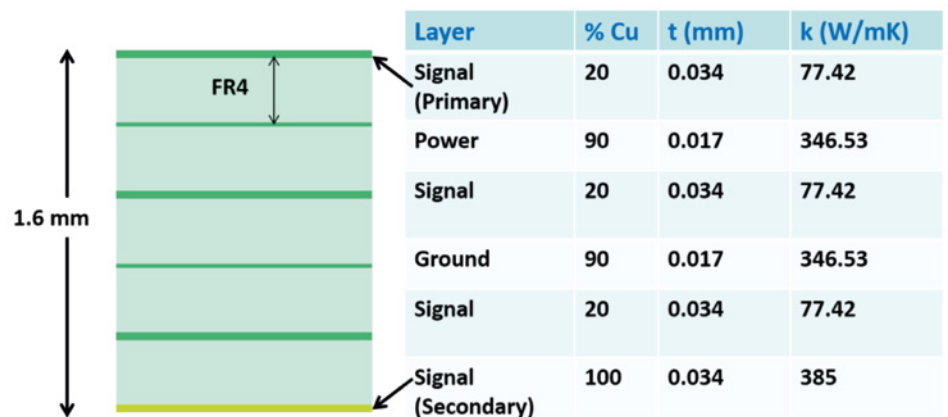


Table 1. Board stack-up and percent of copper coverage.

PSOPs undergo tests for reliability under various stress conditions at the manufacturer, and it would be time-consuming and expensive to physically test or design test boards to test a package in all its possible applications and configurations. This is

where Computational Fluid Dynamics (CFD) software is useful as it can simulate and estimate the junction temperature (T_j) of the IC when attached to the PCB under various conditions. FloTHERM from Mentor Graphics enables a mechanical or electrical

engineer and/or IC designer to quickly see the effect of design changes from a thermal management perspective both qualitatively and quantitatively.

Analog Devices used FloTHERM to perform a computational thermal analysis of a High Speed, High Voltage, 1A Output Drive Amplifier, the ADA4870-1 PSOP mounted on a PCB [1]. Specifically, the goal was to identify the maximum power that could be dissipated on the die active area while keeping the T_j at less than 150°C. Analog Devices studied various environments to estimate this maximum power, for example, changing the board area, adding thermal via, and attaching a heatsink.

Depending on the direction of the formed leads, the package can be surface-mounted on the board either slug down or slug-up, (Figure 2). In a slug-down configuration, the component is surface-mounted on the primary side of the board where the copper slug is soldered to the top side of the board. In a slug-up configuration, the leads are soldered to the primary side of the board. For the experiment, Analog Devices used a slug-down configuration; first with no heatsink, and then with a heatsink attached to the secondary side of the board with thermal grease between the board and the heatsink base.

For the CFD simulation, the test board used was a six-layer board, with dimensions of 59 x 61 mm with the assumption that the copper coverage for each of the conducting layers was smeared uniformly within the layer's volume. Based on this, the thermal conductivity (k) of each layer was calculated as a volume average based on the percent of copper coverage within an individual layer (Table 1).

To accurately predict the value of the junction temperature, it is recommended to discretely model each of the conducting layers with orthotropic conductivity for the entire thickness of the board. Modeling the layers discretely, rather than with a lumped model, captures the effect of heat spreading within the board more accurately for various heat-transfer paths.

Thermal Simulation without a Heatsink

The first set of simulations were conducted to study the thermal behavior of the PSOP mounted on the primary side of the board where the copper slug was soldered to the board, keeping the board horizontal with respect to gravity in an ambient temperature of 85°C.

To emulate real working conditions, heat was applied to two-thirds of the top of the die.

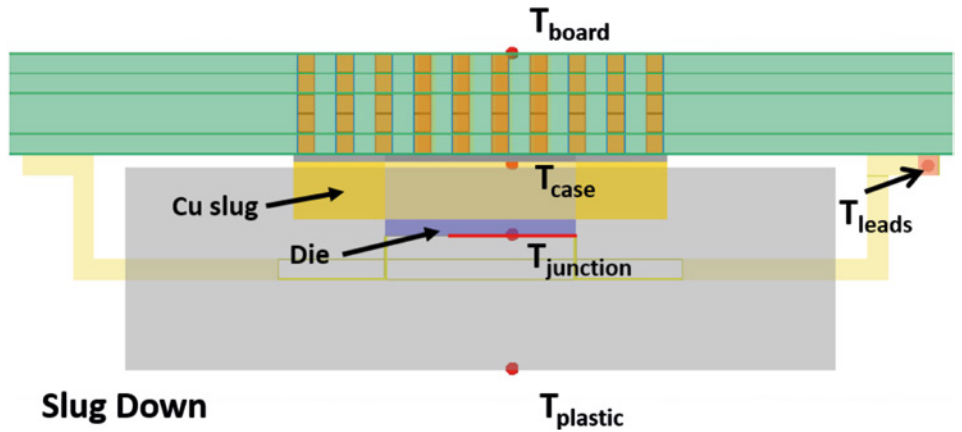


Figure 2. Temperature measurement locations.

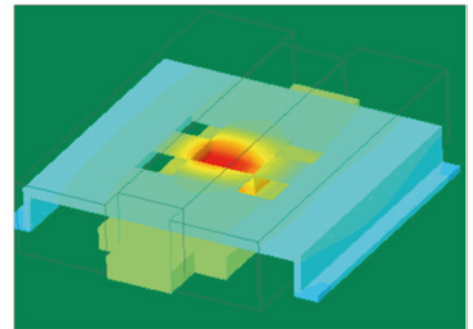
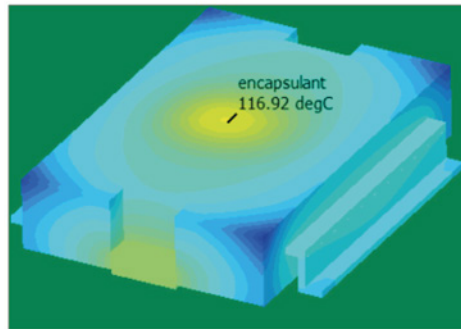
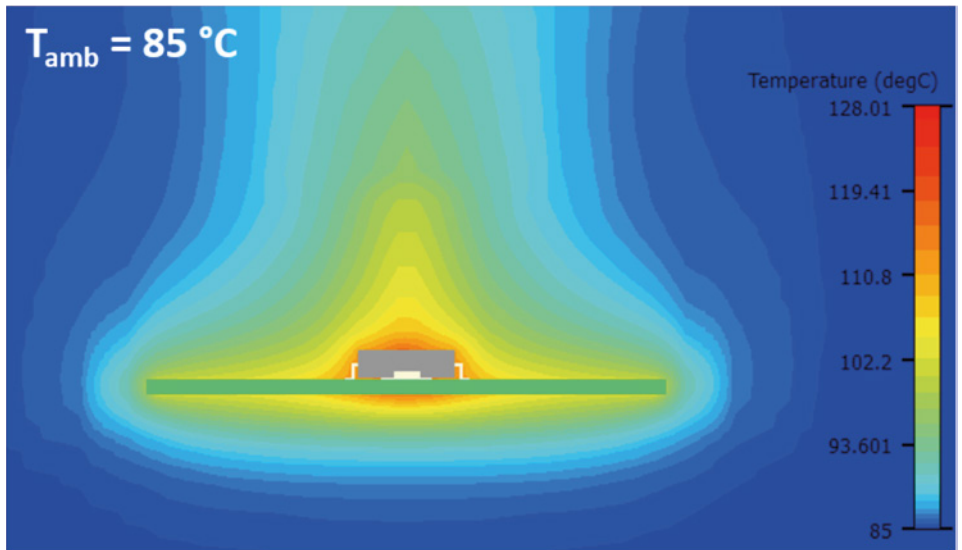


Figure 3. Temperature plots for the package in still air at 85 °C.

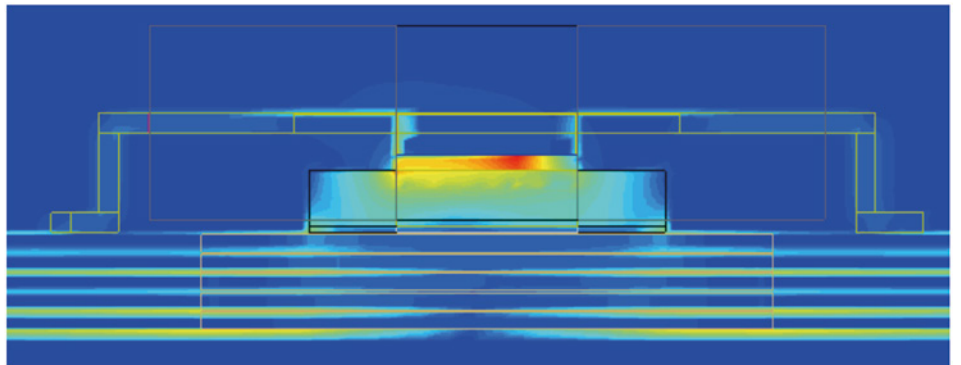


Figure 4. Heat-flux plots for a plane cutting through the package.



The junction temperature (T_j) was measured in the simulation at the geometric centroid of this area, and case temperature (T_c) was measured at a point in the copper slug just above the soldered interface (Figure 2). It is also possible to monitor the temperature of the leads, plastic surface, or any given position to validate the computational results with available test data.

Thermal vias were added under the slug to provide a more conductive path from the copper slug into the board. The vias were placed directly under the copper slug as the numerical investigations revealed a small advantage of adding vias beyond the slug area. This also helps lower board manufacturing costs.

Two possible scenarios for thermal vias were investigated where:

1. Inner layers were isolated; and
2. Inner layers were stitched together.

Stitching the inner layers lowers the junction temperature as a fraction of the heat entering the slug can spread in inner layers; however, including the inner layers raises the core body temperature of the board. Depending on the application, the inner layers could be isolated or used for thermal management. In this study, the secondary side of the board was completely covered with copper.

Figure 3 shows the temperature plots for the package in still air at 85°C and thermal power $P = 2W$ with die-attach material of $k = 1.6 W/mK$ [watts per meter kelvin]. The die-attach was replaced with a more conductive material, $k = 50 W/mK$, which significantly reduced the junction-to-case thermal resistance (θ_{jc}) of the package from 6.61°C/W (celsius per Watt) to 1.12°C/W.

Thermal Simulation with a Heatsink

A heatsink was soldered to the back side of the board to increase the power dissipation through the package, using thermal grease between the board and heatsink. Adding the heatsink significantly reduced the junction-to-ambient thermal resistance (θ_{ja}) from 16°C/W to 5.73°C/W. Heat-flux plots for a plane cutting through the package show the heat spreading over a larger surface area hence reducing the junction temperature for a given value of thermal power (Figure 4).

Table 2 shows the results for maximum power (P_{max}) allowed in the slug-down configuration in still air with and without a heatsink for the two die-attach materials.

Slug-Down Configuration: Still Air at 85 °C				
	Die Attach	θ_{jc} (C/W)	θ_{ja} (C/W)	P_{max}
Without heatsink	Ablebond	6.61	21	3.11
Without heatsink	Cookson	1.12	15.95	4.10
With heatsink	Ablebond	6.78	10.63	6.11
With heatsink	Cookson	1.11	5.73	11.34

Table 2. Thermal resistance for different die-attach materials.

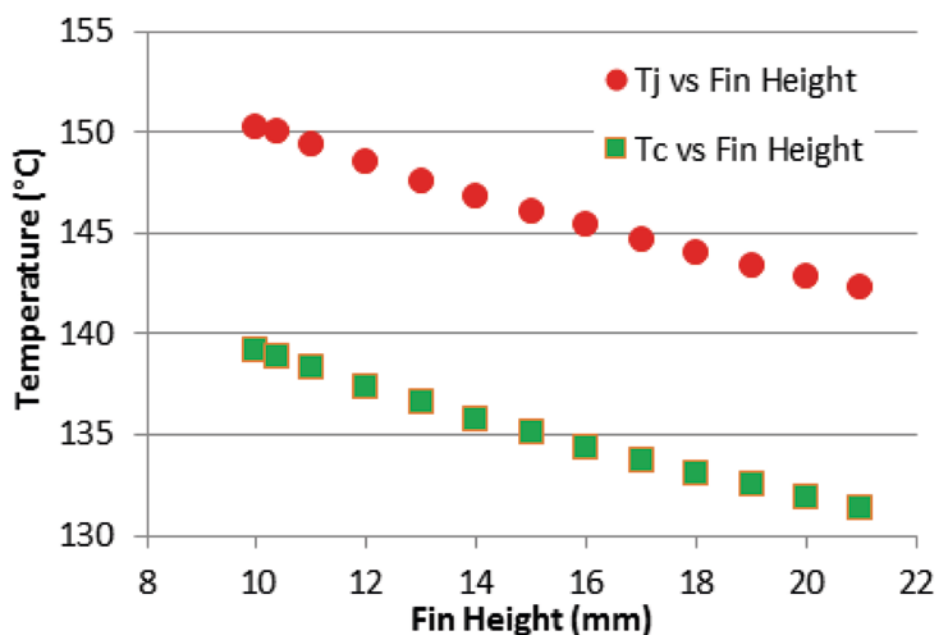


Figure 5. Junction temperature (T_j) and case temperature (T_c) for different heatsink fin heights.

Using the results, the focus of the next study was to use a more conductive die-attach material (Cookson) to find the shortest heatsink sufficient to dissipate 10W of heat at the die. FloTHERM's parametric study capability enabled the team to quickly set up and solve for different scenarios [3]. The variable parameter in this case was the heatsink fin height. The results in Figure 5 show junction temperature (T_j) represented by circles and case temperature (T_c) by squares. It was found that a heatsink with fin height of 10.36mm is sufficient to dissipate 10W.

A further investigation to find P_{max} that could be dissipated if there were tighter constraints on the size of board and heatsink was conducted, thereby reducing the size of both to 30 x 30mm. As well as this the team also studied the effect of different fin heights on junction-to-ambient thermal resistance, θ_{ja} (Table 3).

With forced airflow, the junction-to-ambient thermal resistance could be further reduced,

Board and Heatsink Base: 30 x 30 mm		
Fin Height (mm)	θ_{ja} (C/W)	P_{max} (W)
21	11.82	5.50
15	12.98	5.01
10	14.48	4.49
5	17.12	3.80

Table 3. Thermal resistance vs fin height in still-air environment.

allowing higher powers to be dissipated and T_j to be kept under 150°C. Figure 6 shows the package simulation in a forced-air environment. Table 4 shows the results for heatsink optimization in forced air. Note that, with forced airflow of 2 m/s, the package could dissipate over 20W of heat for a fin height of 21mm and 17W with fins just 10mm high.

A similar parametric study was done for the smaller heatsink with a base of 30x30mm for different fin heights in forced air (Table 5). The smaller heatsink with 10mm high fins (lighter weight) offered the same performance as a larger heatsink with 5mm fin height.

Several parameters affect the thermal conductivity of the board in the region of the vias [4]. Creating a test board for every possible thermal via configuration and testing in a lab is practically infeasible. FloTHERM can be used to perform sensitivity studies of thermal performance to various via parameters, such as the pitch, plating thickness, and fill material (Figure 6). Such computational studies reduce the number of prototypes needed for testing or validation.

In a CFD program, it is computationally intensive to model each and every via discretely, so a lumped approach was used, the region of vias was replaced with a block of orthotropic conductivity that had in-plane conductivity (k_x) and through-plane conductivity (k_z). The board-import tool in FloTHERM was used to calculate the k_x and k_z of this via block, but values could have been calculated analytically [2, 5].

Thermal vias with an outer diameter of 0.3mm were studied. Figure 7 shows the sensitivity of thermal conductivity of via block to pitch and plating thickness (t). The dielectric material used in this calculation was FR4 ($k = 0.3 \text{ W/mK}$), and the fill material was pure copper ($k = 385 \text{ W/mK}$).

Thermal simulations were conducted for PSOP in still air, based on the conductivity values of the via cuboid (Figure 8). The results show that when plating thickness t is 75 μm or higher, even sparsely populated vias are sufficient. However, at low plating thickness, 25 μm or lower, the vias need to be populated densely to ensure the component does not experience thermal failure.

Validating Simulation Results

Laboratory experiments were conducted to validate the CFD model results. The IC inside the PSOP package is capable of dissipating 10 Watts of power and has an integrated temperature monitor. The relationship of the voltage at monitor-to-die temperature is not an absolute temperature indicator. However, the change in voltage versus temperature is a reliable indicator of relative changes in die temperature. Calibrating the temperature-monitor voltage versus temperature function was the first step in understanding die temperature used to determine thermal resistance.

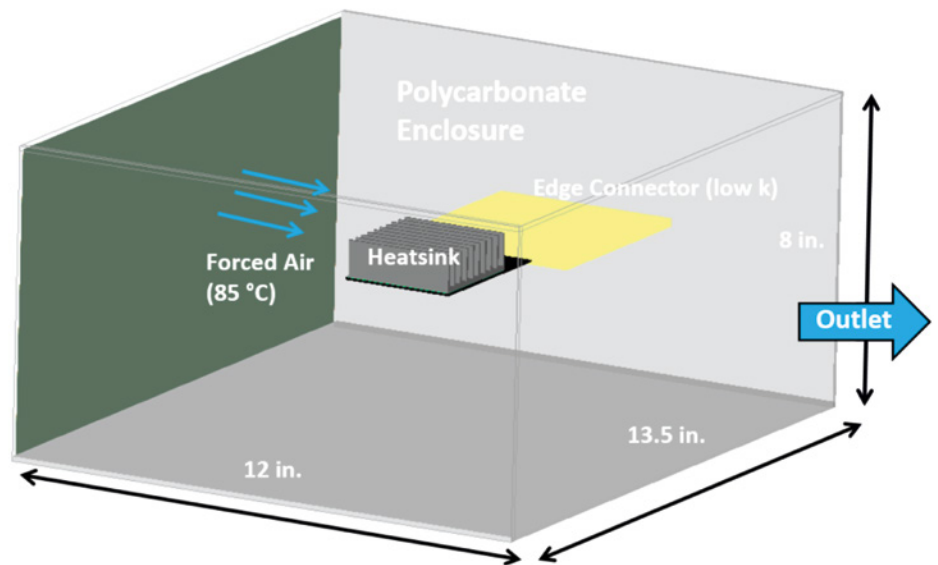


Figure 6. Package with heatsink in a forced-air environment

Forced Air, Heatsink Base 61 x 59 mm				
	1 m/s		2 m/s	
	θ_{ja}	P_{max} (W)	θ_{ja}	P_{max} (W)
21 mm	3.59	18.1	3.18	20.4
15 mm	3.95	16.5	3.42	19.0
10 mm	4.46	14.6	3.8	17.1
5 mm	5.36	12.1	4.49	14.5

Table 4. Thermal resistance versus fin height in forced air. θ_{ja} : junction-to-ambient thermal resistance, P_{max} : maximum power.

Forced Air, Heatsink Base 30 x 30 mm				
	1 m/s		2 m/s	
	θ_{ja}	P_{max} (W)	θ_{ja}	P_{max} (W)
21 mm	4.4	14.8	3.62	18.0
15 mm	4.85	13.4	3.95	16.5
10 mm	4.46	11.9	4.42	14.7
5 mm	6.48	10.0	5.3	12.3

Table 5. Thermal resistance and maximum power for forced air. θ_{ja} : junction-to-ambient thermal resistance, P_{max} : maximum power.

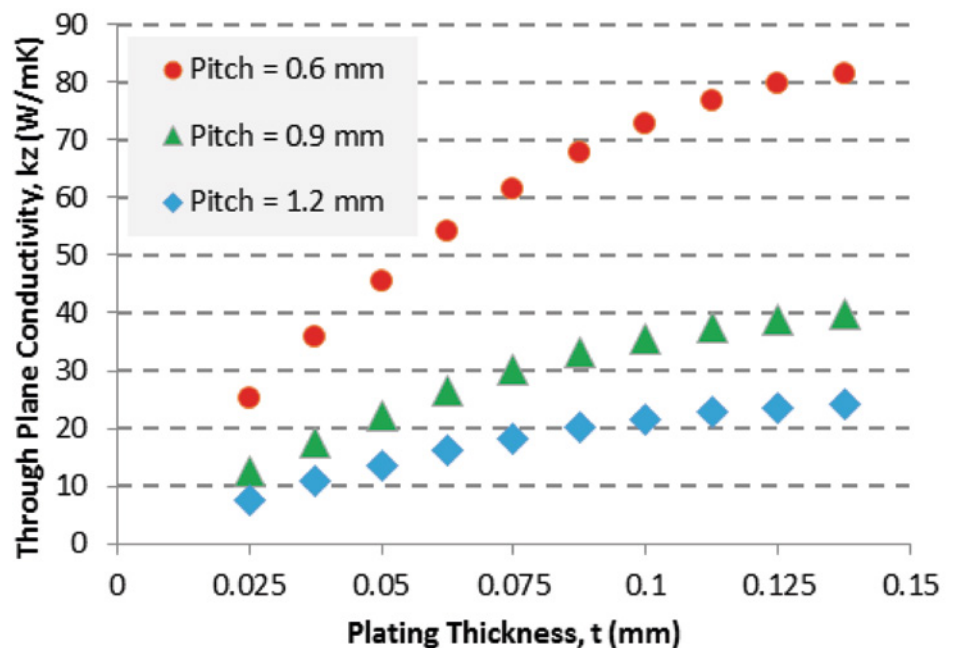


Figure 7. Sensitivity to via pitch and plating thickness. k_z : in-plane conductivity

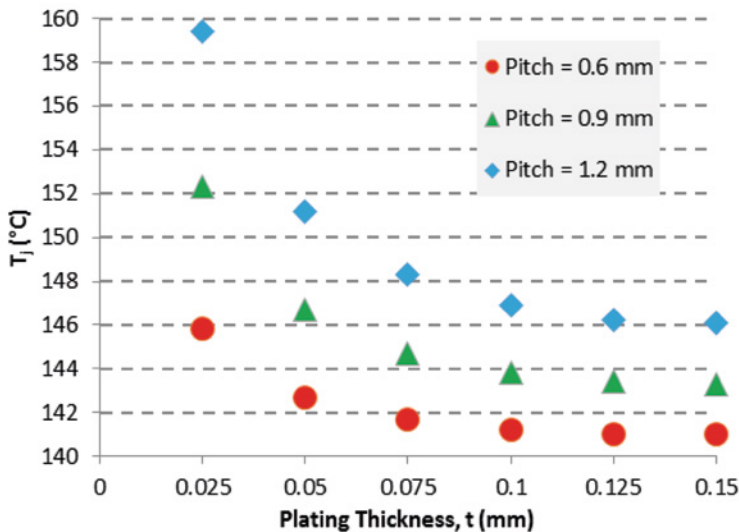


Figure 8. Junction-to-ambient thermal resistance (θ_{ja}) to via pitch and plating thickness in still air.

The PCB used in the lab was FR4-grade with six layers of copper and exposed copper planes, onto which the ADA4870-1 PSOP package was soldered and heatsinks were mounted. Copper-filled thermal vias were used to conduct heat from the IC side to the bottom of the board where a precise temperature sensor was soldered directly below the thermal slug of the PSOP package onto the back side of the PCB. A heatsink was bolted to the back side that straddled the sensor using silicon grease as a thermal interface material between the heatsink and the PCB.

The PSOP assembly was placed into a still-air chamber using automated instruments and power supplies and allowed to soak overnight without any power applied. The ADA4870-1 IC and temperature sensor were then both turned on and measurements of the PSOP temperature-monitor voltage and sensor-trimmed PTAT (power sub-threshold proportional to absolute temperature) current were made immediately. The temperature-monitor voltage measurement was related to the absolute temperature indicated by the temperature sensor. This process was repeated at several temperatures to develop a calibration of the temperature-monitor voltage to absolute temperature (Figure 9).

Using a linear fit to the curve ($T [^{\circ}\text{C}] = \text{TM} [\text{V}] - 1.93/0.003$), the voltage was converted to temperature. Additional steady-state tests were done to reveal the practical limits of power dissipation (maximum power) as a function of the applied heatsink. As shown in Table 6, large heatsinks are necessary when operating at the limits of power dissipation for the tested IC. It was calculated the junction-to-ambient thermal resistance (θ_{ja}) from the measured data by the following relationships

$$\text{at steady state: } \theta_{ja} = \Delta \text{ TM (V)} - 1.93 \text{ (V)} - 0.003 \text{ V/}^{\circ}\text{C} \Delta \text{ Power (W)} = ^{\circ}\text{C/W.}$$

The results showed the FloTHERM CFD simulation to be in good agreement with the lab test results with a heatsink mounted, where the dominant heat-transfer path is from the die into the heatsink. There is a higher difference for simulations with no heatsink, where an appreciable fraction of the total heat travels through bond wires and leads into the top layer of the PCB. This difference can be attributed to assumptions in simulation made in modeling the leads and bond wires in the simulation.

Conclusion

With these experiments, Analog Devices found that FloTHERM is a complimentary tool to laboratory testing, enabling quick parametric and design optimization studies in the thermal design. Such data is useful for studying electronics in harsh environments with increasing demands on power. The next step would be to analyze the transient behavior of the package and thermal characterization using structure functions generated by hardware testing, such as the Mentor Graphics T3Ster. A transient thermal simulation validated by test data would go a long way in simulating the transient response of a package for various powering conditions and reduce the number of laboratory tests needed.

References

- [1] Analog Devices, High Speed, High Voltage, 1.A Output Drive Amplifier ADA4870, <http://www.analog.com/media/en/technical-documentation/data-sheets/ADA4870.pdf>
- [2] Bornoff, Robin, Blackmore, Byron, Parry, John, "Heatsink Design Optimization using the Thermal Bottleneck Concept,"

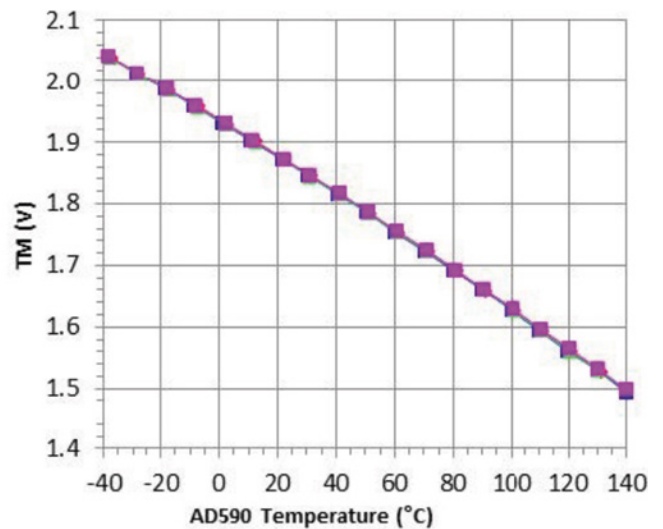


Figure 9. Temperature monitor (TM) volts versus sensor temperature.

Package Mounted in Slug-Down Configuration				
Test Case	Test Data		CFD Data	
	θ_{ja}	P_{max} (W)	θ_{ja}	P_{max} (W)
25°C no heatsink	12	10.42	16	7.81
25°C w/ VHS-45	7	17.86	8.87	14.1
85°C no heatsink	12	5.33	16	4.1
85°C w/ VHS-45	7	9.14	7.81	8.35
85°C w/ VHS-95	6.2	10	5.73	11.34

Table 6. Thermal testing versus simulation results. θ_{ja} : junction-to-ambient thermal resistance, P_{max} : maximum power.

Proceedings of 28th IEEE SEMI-THERM Symposium, San Jose, CA, March 2011, pp.76-80.

[3] Li R.S., "Optimization of thermal via design parameters based on an analytical thermal resistance model," Thermal and Thermomechanical Phenomena in Electronic Systems, 1998. ITherm 1998, pp 475-480.

[4] Incropera, F., Dewitt, D., et al., Fundamentals of Heat and Mass Transfer, John Wiley and Sons (New York, 1993), pp. 65-67.

How To...

How to characterize heat exchangers

BY Mike Gruetzmacher, Technical Marketing Engineer, Mentor Graphics



Ever wondered why birds' feet don't freeze on cold surfaces, for example birds on cold branches or ducks on frozen lakes? The answer is not that they produce sufficient energy to warm up their feet. This would need too much energy and their feet might stick on the ice [1]. The solution is they keep their feet temperature at almost the same level as the ground by using a heat exchanger system in their legs. The heat is exchanged between the vein and the artery, so the cold blood coming back from the foot is heated by the hot blood moving to the foot which cools down simultaneously. It's a perfect energy saving system. What nature successfully applies man can also use. Heat exchangers are used in a variety of designs in all industries.

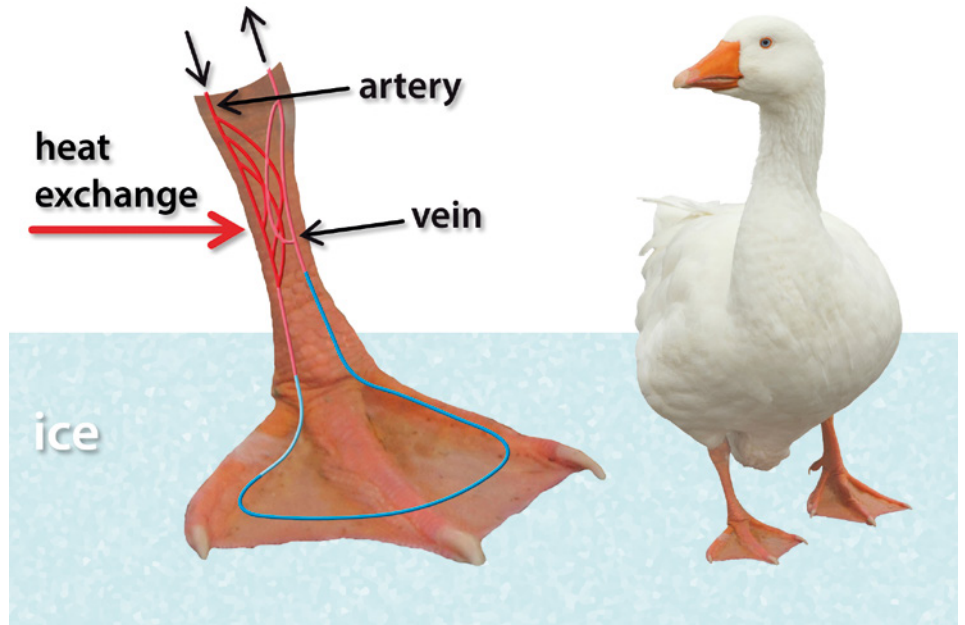


Figure 1. Natural example of a heat exchanger

Fundamentals

In most cases indirect heat exchangers are used where two streams are separated by a wall. Explaining all types of heat exchangers would go beyond the scope, so we'll focus on one general example. There is no energy source, so the heat is only exchanged between the two fluids. In addition heat losses into the ambient are neglected. In industrial applications, usually efficient insulation is provided. If losses are to be taken into account, the engineer takes into account a performance reserve depending on the ambient conditions.

A couple of basic equations to explain the fundamentals:

The total heat flux (W) applied to each fluid is defined by:

$$\dot{Q} = \dot{m} \cdot c_p \cdot \Delta T$$

Where \dot{m} = mass flow rate (kg/s), c_p = heat capacity (J/kgK), and ΔT = temperature difference between inlet and outlet (K). If losses are neglected, the amount of heat flux for both fluids has to be equal. This equation is applicable for a heat balance examination but it does not give any geometrical information.

Furthermore, the exchanged heat duty is defined as (which considers geometrical information):

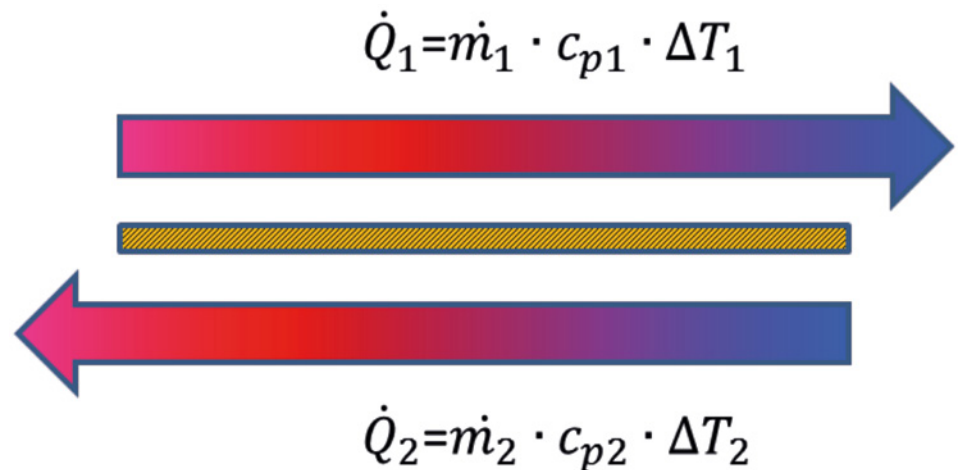


Figure 2. Heat flux for each fluid (index 1 and 2 for fluid 1, 2 respectively)

$$\dot{Q} = k \cdot A \cdot \Delta \vartheta_m$$

Where k = overall heat transfer coefficient (W/m²K), A = heat transfer surface area (m²), $\Delta \vartheta_m$ = logarithmic mean temperature difference (K)

$$\Delta \vartheta_m = \frac{\Delta T_1 - \Delta T_2}{\ln(\Delta T_1 / \Delta T_2)}$$

The easiest way to increase the performance is to increase the area A , but unfortunately this is often the most expensive way and leads to device enlargement. The temperature difference is

defined by the process data requirements. Another remaining opportunity is to optimize the overall heat transfer coefficient k .

$$k = \frac{1}{\left(\frac{1}{\alpha_1} + \frac{s_w}{\lambda} + \frac{1}{\alpha_2}\right)}$$

Where α_1, α_2 = heat transfer coefficient for fluid 1 and fluid 2 (W/m²K), s_w = wall thickness (m), λ = thermal conductivity of the material (W/mK)

Remark: The formula symbols can vary between countries and special applications for example for heat exchanger or civil

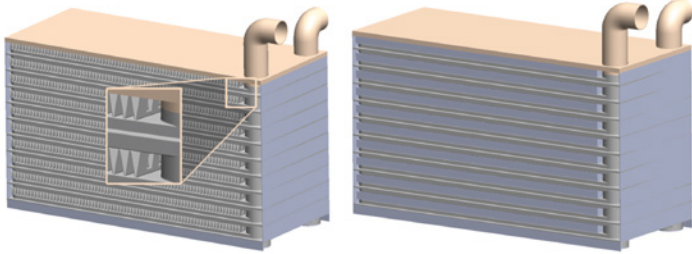


Figure 3. Automotive Heat Exchanger Example

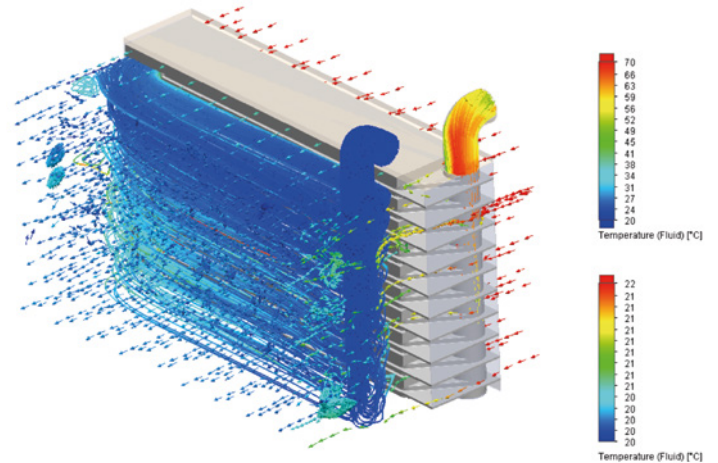


Figure 3a. Liquid and Airflow Vectors

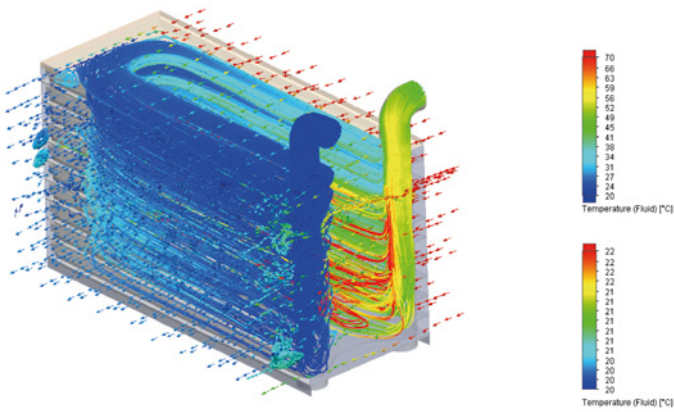


Figure 3b. Detailed Flow Fields

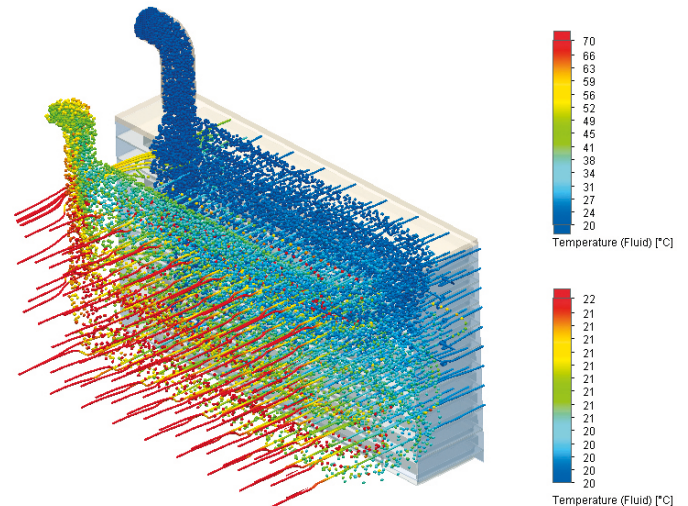


Figure 3c. Particular Flows

engineering. U can be used instead of k , h instead of α and so on.

Application

To improve the performance, the heat transfer coefficient α , can be increased by increasing the turbulence inside the flow. However, this leads to an increasing pressure drop at the same time which requires higher energy consumption for fans or pumps. This is the most challenging and appealing goal for the engineer during the design process. The engineer has to determine the factors to design the most thermally efficient device. The main considerations are: mass flow, temperature difference, and pressure drop in each case for both flows. For instance, the mass flow and inlet temperatures are given and specific outlet temperature ranges

are required with the constraint that the pressure drops remain below a target value for various load cases. At worst, insufficient performance or excessive pressure drop can result in contract penalties.

Example

Figure 3 shows a generic automotive heat exchanger. This is a representative example for a wide range of heat exchanger types. The inside flow medium is water, the outside medium is air. To increase the heat exchange area, plate-fins are arranged in the air side. We will use the porous media capability as a surrogate material because a detailed simulation of these thin structures would result in an extensive calculation time. The water side has two passes in a U-shape without any installations inside the passage.

For this example we investigate the following four sheet metal variations (Figure 4): The first step is to characterize the examples in terms of pressure drop and heat transfer rate. A section of the overall model (Figure 5 a+b) is calculated using the FloEFD parametric study for several inlet velocity variations with constant inlet temperature (for example 100°C).

From the parametric study we get the pressure drop and the enthalpy difference, from which we calculate the heat transfer coefficient, depending on the mass flow rate. The flow and heat balance has to be applied on the inlet and outlet of the heat exchanging structure or a section within it. The results are shown in figure 6.

Version 00 shows the lowest pressure drop but also the lowest heat transfer coefficient. Version 03 shows the highest heat transfer coefficient but also the highest pressure drop. This opens the opportunity to downsize the device and reduce the needed space but resulting in higher pressure drop and energy consumption.

These characterized curves for the pressure drop and heat transfer coefficient in combination with the geometric sheet metal properties can now be used to define the porous media properties in the FloEFD engineering database. With this porous media as surrogate material, the overall heat exchanger can be simulated in an acceptable time. One engineering goal might be to ensure a specific air outlet temperature for given volume flow rates. This can lead to an operational diagram as shown for example in figure 7. The figure shows also the results of a variation without any sheet plates which of course shows the highest air outlet temperature.

As shown in figure 7 the air outlet temperatures for Version 02 and 03 differ only slightly. So for this operating condition the version with the lower pressured drop (Version 02) might be the more efficient choice.

Summary

These investigations are particularly important in today's design world processes, as energy consumption and space requirements are becoming increasingly important factors for engineers to consider. Particularly with regard to industries like automotive or aerospace where every gram counts and a reliable operation for several load cases must be ensured at the same time. Nature has often developed the most efficient solution. Adapting nature's solutions is good, but sometimes just imitating is not sufficient and we need to apply further considerations.

References

[1] <https://bybio.wordpress.com/2014/11/14/cold-weather-and-one-legged-birds/>

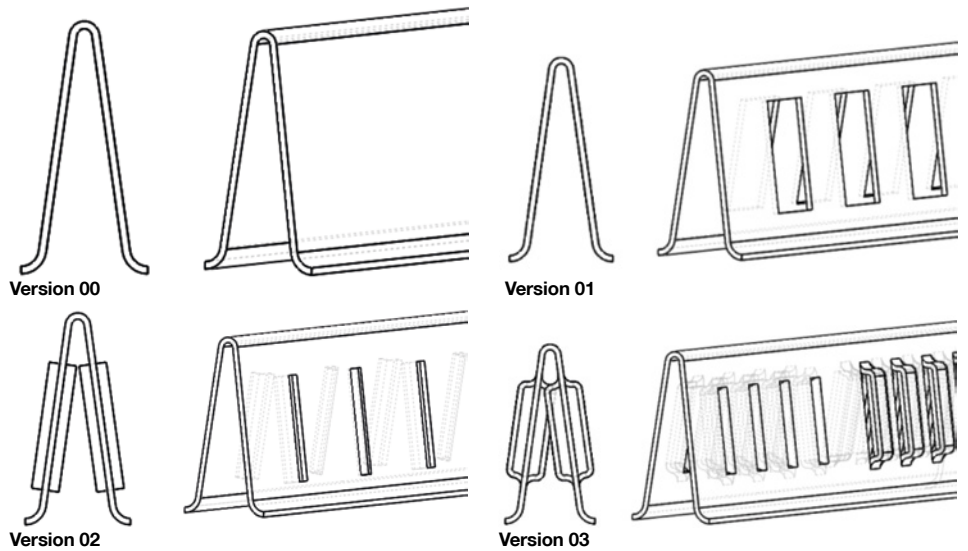


Figure 4. Sheet Metal Variations

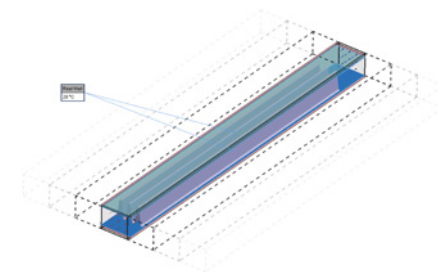


Figure 5a. Model Section Heat Exchanger

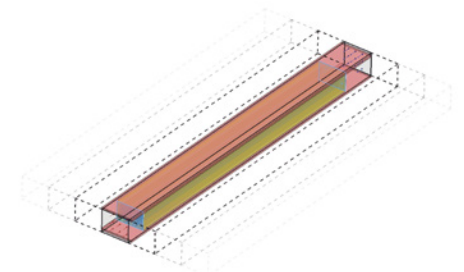


Figure 5b. Model Section (Porous Media)

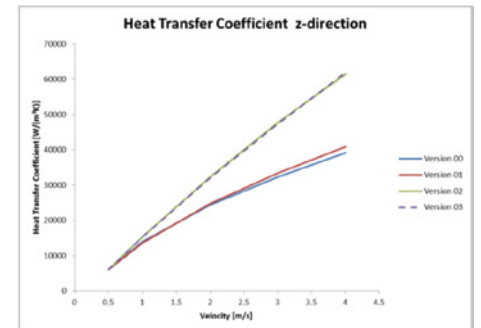
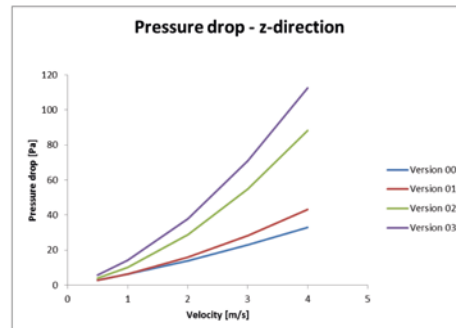


Figure 6. Pressure Drops and HTCs for versions 00 to 03

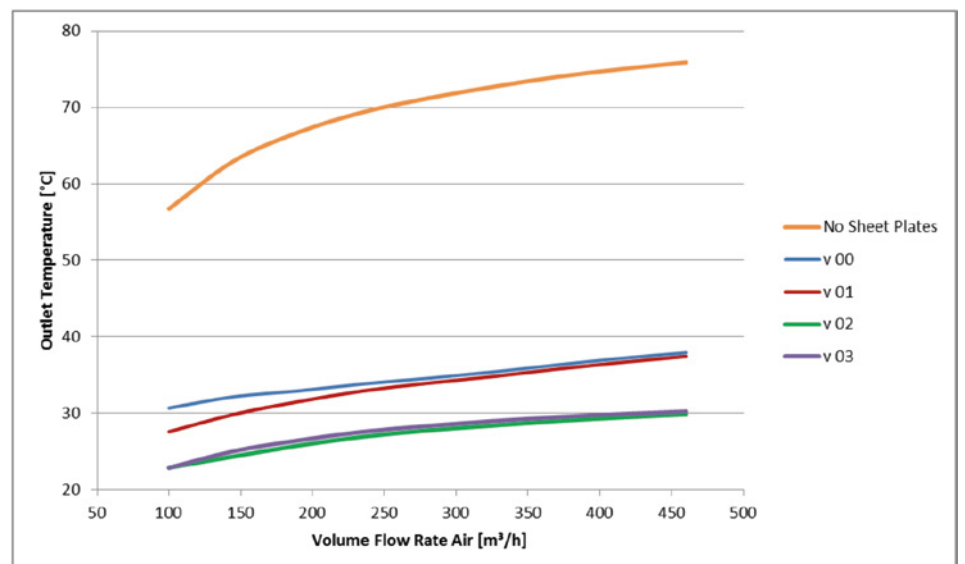


Figure 7. Example Results Diagram



Making Light Work of Lifting

Liebherr-Werk Nenzing GmbH use FloEFD™ for Creo™ in their Mobile Harbor Crane Designs

Interview Kolio Kojouharov, CFD Expert, Liebherr-Werk Nenzing GmbH, by Thomas Schultz, Application Engineering Manager, Mentor Graphics

Liebherr Werk-Nenzing GmbH, manufacturer of maritime cranes, crawler cranes and foundation equipment, demonstrates the importance of modern “Frontloading” simulation tools which go far beyond classic FEA-Analysis within the heavy duty industry.

From your experience how is the heavy duty simulation world doing at present?

The simulation world is more than ever dominated by strict regulation due to emissions, performance and comfort. It has become more and more important over the years to think beyond the classic FEA-Analysis, which most people immediately associate with our industry and applications.

Recognizing the potential for FEA-Analysis, how does CFD fit?

From a simple hydraulic block to a full power pack there is an almost infinite number of tasks waiting to be analyzed. The large number of potential cases which might consume needless power has been realised over the past years. However, external simulation services to solve this soon turned out to not be efficient enough and too expensive. At Liebherr we have high standards, so finding the tools to meet them was not an easy process and took a long time.

Why was FloEFD chosen?

As a company we were aware of FloEFD™ and indeed the concurrent approach of the technology. The over-riding reason was the strong pre-&post processor in combination with the efficient meshing. Alongside the advantage of full CAD-integration into our CREO environment, allowing quick analysis of full power packs in our own CAD system. This gives me the ability to analyze more projects at the same time, something competitors are not able to achieve.

How does FloEFD help with the complex structure of power packs?

Power packs basically contain everything below

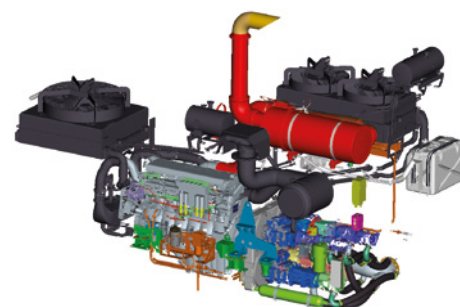
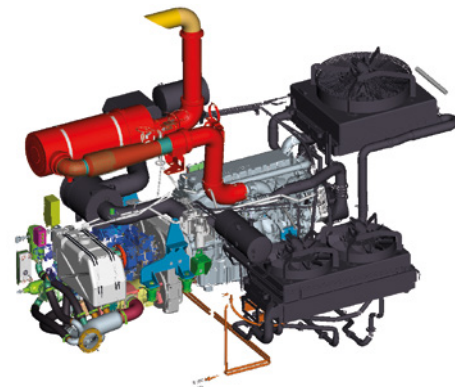


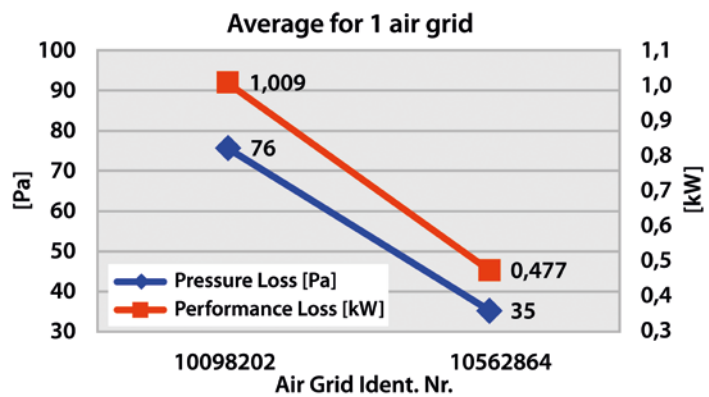
the engine hood, and typically include many devices such as cooler (diesel, water, air and oil), fans, exhausts, and hydraulics. This means that our CAD models can be rather large, with up to tens of thousands of components including all screws.

The requirements on the CFD software are therefore tough and it became apparent that most commercially available codes were not able to handle this kind of complexity, hence our need to turn to FloEFD.

The whole development cycle is influenced by this and the flexibility FloEFD allows, means that I can make decisions before, and not after, when it is too late.

There are many examples, a practical example of how FloEFD has helped with our mobile harbor crane, the LHM 550 and the inlet section of the power pack. I wanted to look at the efficiency and optimization of the protective grids. The basic inlet hood contains two rows of baffles to avoid unwanted particles such as dust or rain being inhaled by the engine. On the other hand, a set of baffles means that we have a potential performance loss between the environment and the engine. The idea is that we can save energy when we reduce the resistance.





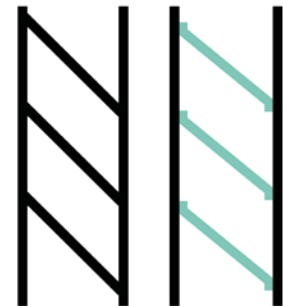
Did you use the full CAD-crane model to set up the FloEFD project?

Theoretically with FloEFD we could, but in this context it was not required. For the first step it was sufficient to have the coolers with two fans and the grids. The exhaust system was also integrated to see thermal effects near the sheet metal walls. We soon realized that the angular position of the baffles was not optimal, so we needed to locate the optimum. We used FloEFD's parametric study feature to let the software find the best angle position with the lowest pressure loss. However, always with respect to an acceptable protection against particles.

We also removed the middle beam which obviously represents a barrier for the airflow. The whole process including meetings, documentation, and decision-making, took two working days.

Are you experienced in transferring such geometry and generating the mesh?

No, not really. However, unlike the other CFD tools I experienced, FloEFD follows a completely different approach by being CAD embedded which allows me to fully skip the transferring geometry step. With regard to the mesh, people typically struggle with body fitted meshes and its manual creation of boundary layers etc. Indeed it takes much less time for the mesh generation compared to classic

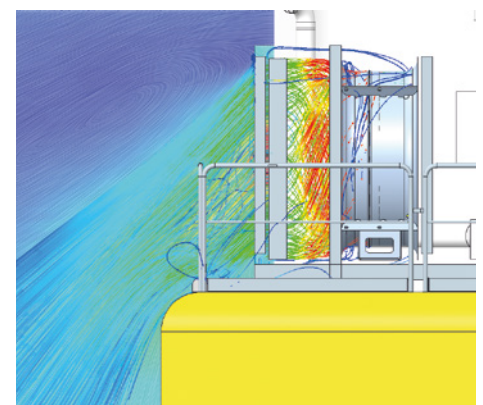
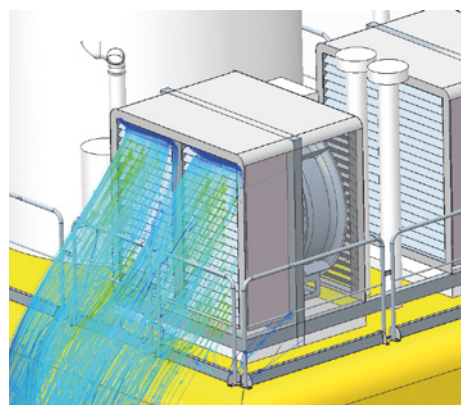


CFD-approaches. It saves us not just hours or days but weeks, this in turns gives us the benefit of not only saving time but money too. The amount we save with the reduction of man-hours spent on the project can be easily put into numbers. Not to mention the manufacturing cost savings per unit and year.

The target of increasing the performance and reducing emissions was achieved. A very welcome side-effect was that we automatically improved and simplified our manufacturing process which saves further costs. We now glue the baffles onto the frame instead of welding them.

Did you face any problems following this change in design?

We didn't face any real problems, other than the assembly team told us that removing the beam from the middle results in one single baffle for each row, instead of the initial two, so now the team has to carry double the weight while mounting.





A Lesson Learned

Rockwell Collins Improve simulation processes for Commercial Aircraft Avionics

By Mike Croegaert, Industry Vertical Manager, Mentor Graphics

**Rockwell
Collins**

Rockwell Collins is a leading manufacturer of aircraft avionics systems for both commercial and military markets. They have a staff of highly experienced thermal analysts that utilize FloTHERM® Electronics Thermal Analysis Software for upfront simulation to predict the thermal performance of these products early in the design process and make design decisions around thermal management. Some of the analysts have over 20 years' experience using FloTHERM, so when for a particular product, the results of thermal testing were significantly different than the results of their analysis, there was a great deal of surprise. Even after updating the FloTHERM model to better match the final design, the results still did not correlate in a non-conservative way to the test data to one key test scenario. This caused them to kick off a lessons learned exercise to better understand what was causing the discrepancies.

The product in question is the data processing element of a cockpit display system for a new, large commercial aircraft. The product is forced-air cooled; designed to meet Aeronautical Radio, Incorporated (ARINC) Standard number 600. It comprises a top-level chassis or Line Replaceable Unit (LRU,) that dissipates approximately 100W with several subsidiary LRUs or modules inserted into it. The system had a requirement to operate for 180 minutes after the loss of the aircraft supplied cooling air; termed a Loss of Cooling or LoC scenario. It was this scenario where the CFD analysis failed to correlate to test.

In this particular case, the preliminary thermal analysis included an up-front Computational Fluid Dynamics (CFD) analysis using preliminary mechanical and electrical design information to model the thermal situation inside the unit

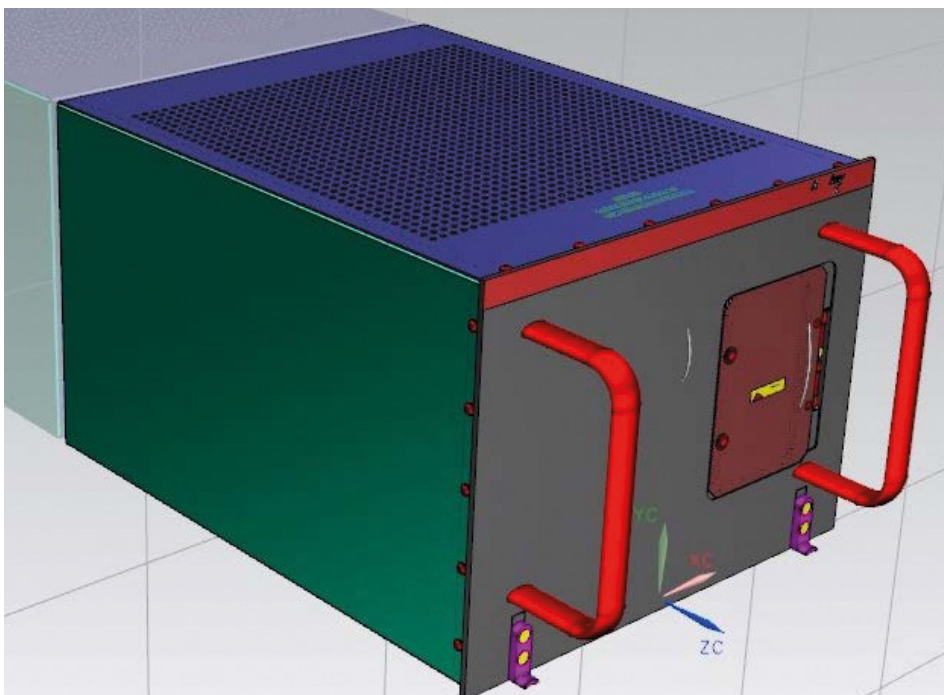


Figure 1. Chassis Model Mechanical Overview

using FloTHERM. The results of this analysis were utilized to establish an initial thermal design strategy for the chassis, which included heatsink design and airflow management. The thermal design plan included a subsequent thermal survey on a fully instrumented early engineering unit, developed to account for the results of this initial thermal modeling. Both the thermal modeling efforts and the thermal survey testing addressed three operating environments: Normal Flight Operating (NFO), Normal Ground Operating (NGO), and Loss of Cooling (LoC). The Loss of Cooling environment required stabilization under Normal Flight conditions followed by operation with no forced-air cooling for 180 minutes. This environment largely drove the design of the system as the

COTS components were very near to their upper engineering temperature limits. The custom heatsinks implemented in the unit were optimized for best performance across the various environments using the CFD tool.

During the LoC test portion of the thermal survey, the unit suffered functional failures and many of the temperature predictions were as much as 20°C below the corresponding test data. These discrepancies between analysis and testing gave rise to late design modifications. A quick review of the thermal model indicated that the model was constructed fairly well and seemed to be reasonably representative of the final configuration of the product. There were

some areas where the model fell short, such as where component parameters weren't available, as the part had not yet been fully designed, so their power was spread over the Printed Wiring Board's (PWB's) surface. In general, the model was built to the usual standards. Correcting the obvious few small shortcomings did not completely rectify the errors that were seen in the result.

In order to maximize the efficiency and knowledge benefit of the exercise, the original team of engineers that performed the thermal analysis and heatsink optimization was pulled together. The investigation was run as a small engineering project. The goals defined for the study were to try to understand where the initial modeling effort had fallen short, find, and then document the requisite changes in modeling approach to improve the prediction accuracy of future modeling efforts for a chassis of this type.

The first task undertaken in the review was to revisit the initial thermal model used to evaluate the thermal situation which drove the heatsink and airflow metering strategy for the chassis. The model was updated to match the geometry and component thermal details as they were tested in the thermal survey without significant changes to the modeling assumptions used in its construction. Two specific sets of test data were chosen to pursue correlation that then drove, by necessity, two separate CFD models. The two tests chosen were identified as the most representative of the chassis final configuration with only small, known exceptions that could be modeled separately for each (e.g. presence or absence of heatsinks added in the given test.). The goal for this effort was not so much to accurately model the final configuration of the chassis as it exited the testing but, rather, to get to a correlated model that made engineering sense and that matched each set of thermal test results for each of the two operational configurations.

This chain of events was fortuitous because, as the correlation effort progressed, it became clear that the effort would require two quite dissimilar models in order to get correlated results for each operational situation. The LoC model ended up being different from the NFO model in ways that exceeded just the differences in unit configuration between the two test scenarios.

From these tests several Lessons Learned were obtained. The two models that came out of this effort uncovered a number of nuances to the modeling of this type of chassis and environment that the team was not aware of at the outset. The lessons learned will facilitate modeling efforts on future programs with similar

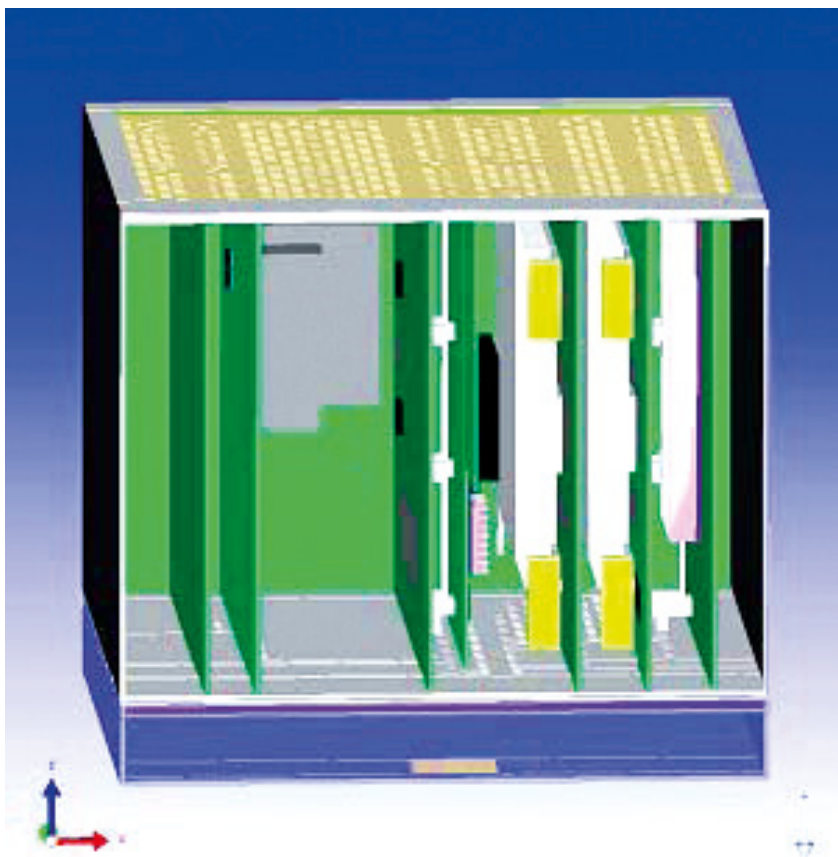


Figure 2. Final NFO CFD Model

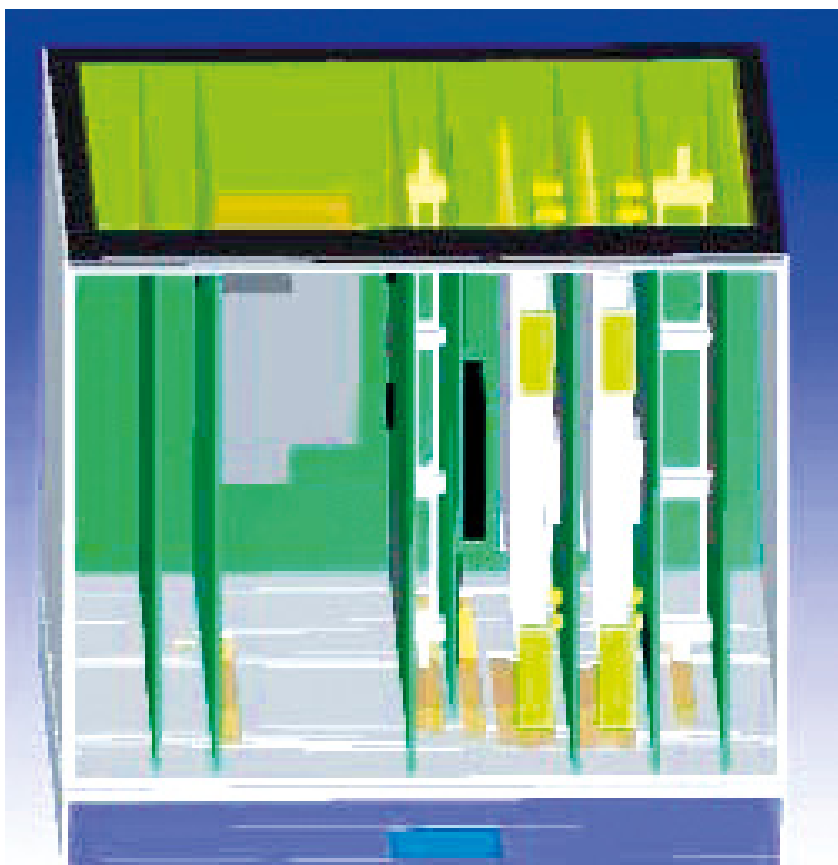


Figure 3. Final LoC CFD Model

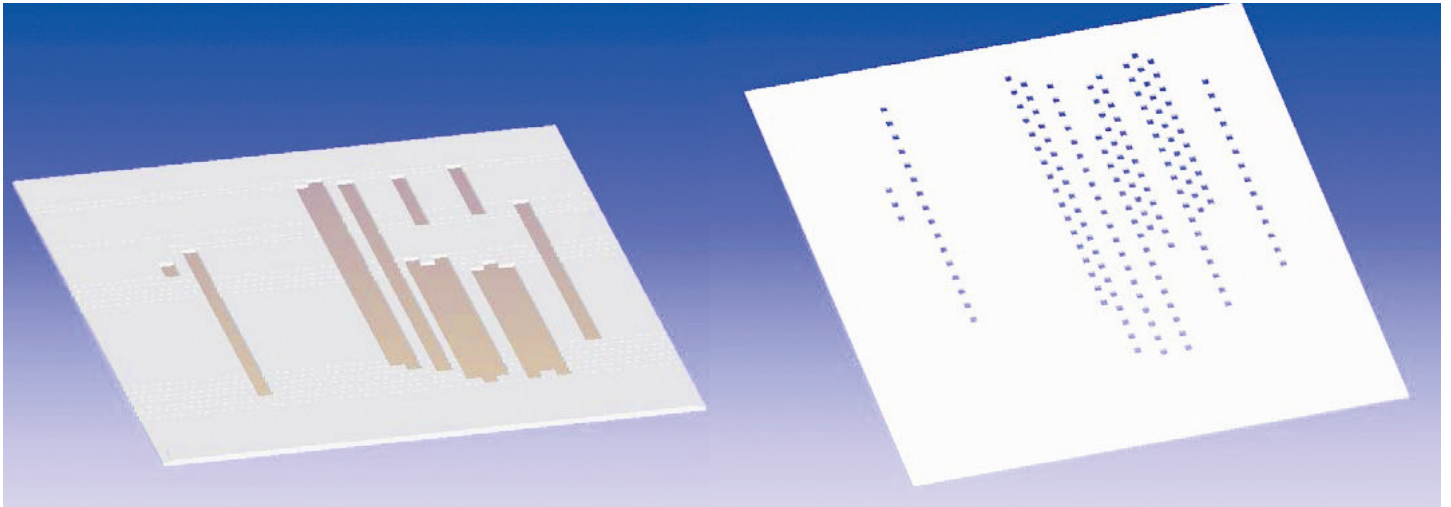


Figure 4. Final NFO (left) and LoC (right) Metering Plates Comparison

chassis designs. Here are some of the more significant findings:

- Both scenarios required refinements of the modeling approach to the inlet conditions for the chassis:
 1. For the NFO case, the original model had utilized correctly sized openings with perforated sheet components with percentage open parameters set to agree with the expected metering plate design. A fixed flow was then imposed on the openings that would provide the required mass flow per the system design. This resulted in a nearly pure vertical flow through the chassis. During the follow-up investigation, the temperatures could not be made to correlate across the entire chassis with this configuration. Two modeling changes were required to fix this issue. The first was to add a detailed model of the plenum used in the test setup. This accurately modeled the airflow within the plenum and introduced lateral and fore to aft flow variations that allowed the model to correlate better. Also for the NFO case, the rows of metering plate holes were modeled as long thin perforated sheet strips, which allowed faster model convergence, but the percentage open had to be adjusted downward to account for the interaction between the inner and outer chassis perforations. See Figure 2.
 2. For the LoC case, the inlet plenum also had to be modeled in detail. Further, getting the mass flow drawn into the chassis by natural convection required that it be monitored and controlled in the simulation. A fixed resistance simulating the test chamber inlet ducting was added and adjusted to match

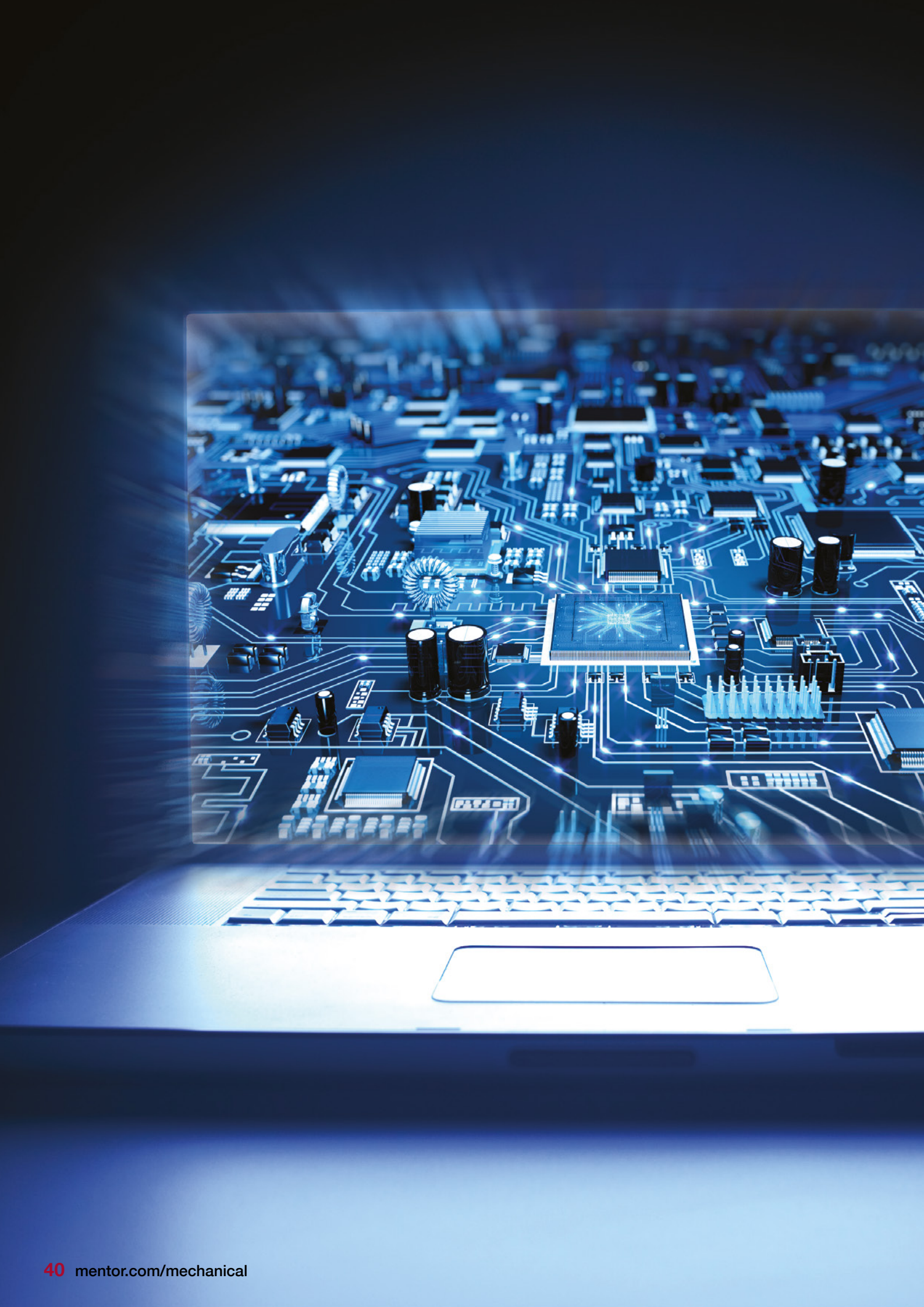
the very low inlet mass flow measured during the LoC tests. While using long thin, perforated sheet strips for the inlet worked well under force air conditions, for the LoC case, this approach did not allow for accurate correlation of the two models. In this case, each metering plate inlet orifice had to be modeled individually, as the velocity profiles across the rows of orifices were not uniform. See Figure 3 and Figure 4.

- The exhaust configuration for both chassis was modeled initially using perforated plate components in FloTHERM. This was found to also not accurately model the exhaust conditions for the LoC case. Ultimately for LoC, the best results were achieved when the chassis top was also modeled as a grid of small orifices below the previous perforated sheet component.
- The LoC model is a steady state model, thus, it produces the temperatures at infinite time. The temperatures used to correlate the model had to be adjusted upward from those measured in the 180 minute LoC test. This was possible to do analytically as the test data was exponential in the last several minutes of the test and a high confidence prediction of the temperatures at infinite time was easy to make. This was a small detail but the error associated with not making this adjustment was greater than the desired 2°C error for predicted temperatures on the hottest components.
- On average, a general component's power dissipation was overestimated under NFO conditions by 20 to 40%. The NFO model, thus, generally overestimated component temperature rises.
- The non-linear thermal behavior versus temperature of several components resulted

in their correlated power dissipations being significantly higher than those found in the correlated NFO model. This demonstrated that having a correlated NFO model, which is then run without airflow to simulate the LoC case, would severely underestimate component temperature rises of all these components.

- In general, the initial power dissipation estimates used to construct the original CFD model ended up matching the correlated power out of the LoC test data. It was found, however, that the final correlated power supply component power dissipations averaged approximately 50% higher than the original estimates. This was attributed to the increased system power required to drive the components that were exhibiting non-linear power increases with temperature.
- The initial model was missing several components because the data for them was not available and some turned out to be key to the heat generation. Some of these components ended up driving specific thermal decisions later, during the appraisal tests. Key point here is to have as many components modeled as early as possible in the process.

This Lessons-Learned project uncovered a number of facets of the original analysis work that go beyond a simply flawed analysis approach. Several of the usual assumptions for this type of CFD modeling proved to be inadequate and/or incorrect. As a side benefit of this effort, a procedure for quickly and reliably correlating a large complex thermal model to measured thermal data was developed and refined. The results presented here are applied on and will improve the results of all follow up development projects.





A Study of Electrolytic Capacitor Thermal Conductivity, Behavior & Measurement

Lenovo™

By Zhigang NA,
ThinkPad Development Lab, Lenovo

Electrolytic capacitors are widely used in electric circuits, and their durability is an important contributor for the entire lifespan of an electric device. Usually, each supplier would have their own lifetime calculation method. For example:

$$L_x = L_0 \times 2^{\frac{T_0 - T_1}{10}} \times 2^{\frac{\Delta T_0 - \Delta T_1}{10}} \quad [1]$$

Where: L_x = Expected life at temperature T_1 °C
 L_0 = Guaranteed life at temperature T_0 °C
 T_0 = Maximum operating temperature (°C)
 T_1 = Actual operating temperature (°C)
 ΔT_0 = Internal temp raise under maximum ripple current (°C)
 ΔT_1 = Actual internal temp raise (°C)

According to Eq.1, a 10°C temperature raise (either ambient temperature or internal temperature) will degrade the lifetime of the capacitor by 50%. In order to devise an adequate cooling solution to prevent the electrolytic capacitor from overheating or even burning, the thermal designer needs to completely understand the component's thermal characteristics.

Due to the constraints of the capacitor corking principals and measurement conditions, it is very difficult to heat a capacitor with an accurately known power. It is also challenging to accurately measure the capacitor internal temperature. Computational Fluid Dynamics (CFD) simulation is a major asset for this type of study. When coupled with real sample tests, CFD can be used to verify key results to ensure the overall accuracy of the study.

Heat Exchange of a Capacitor on PCB Heat Exchange Model

When a capacitor is mounted to a PCB, the PCB acts as a heatsink. From a heat transfer point of view, heat is exchanged between the capacitor, PCB, and the ambient air. The heat transfer modes include conduction, convection, and radiation.

Figure 1 (overleaf) illustrates the heat transfer mechanisms. A thermal resistance network model can also be used to represent this. Since this study was focused on a forced convection system, the effect of heat radiation is ignored because it has very little affect on heat transfer due to the relatively low temperature of the capacitor.

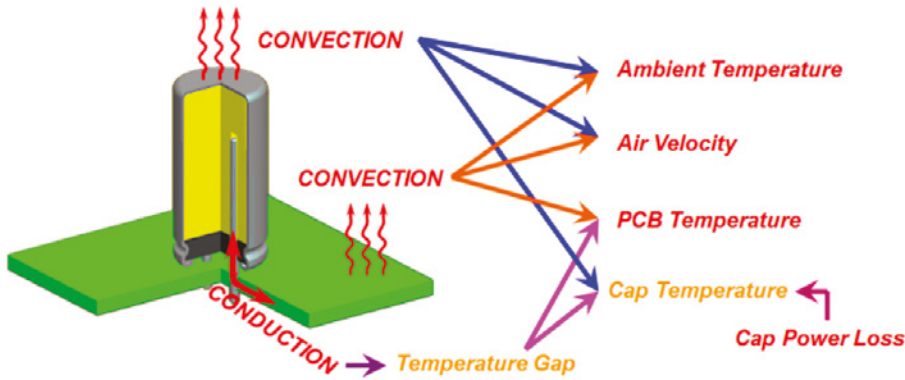
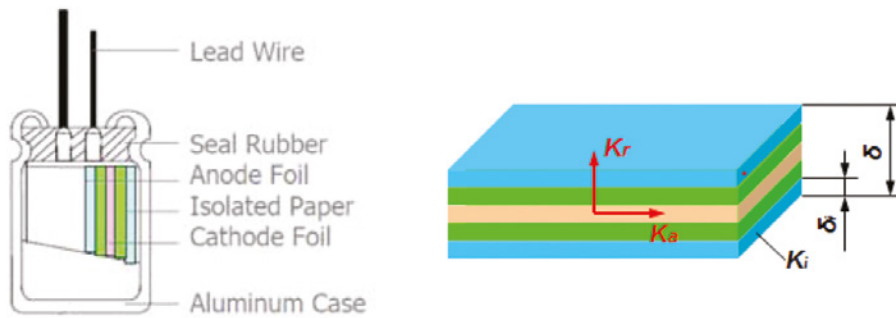


Figure 1. Heat exchange modes of a Capacitor on PCB



(a) Capacitor structure [1]

(b) Simplified winding structure

Figure 2. Capacitor structure and simplified winding structure

Heat Transfer Boundary Conditions

From Figure 1, the ambient temperature; air velocity; and PCB temperature impact at least one heat transfer mode in this system, and so they are all boundary conditions for heat exchange of the capacitor.

Since the capacitor is a heat source, generating a certain amount of heat, the capacitor's power loss is also a boundary condition. Meanwhile, the PCB can be treated as a heatsink in the system, as it has much bigger thermal mass than the capacitor. The impact caused to the final result by this treatment can be ignored.

Modeling of a Capacitor Internal Structure of Electrolytic Capacitor

Figure 2(a) shows the internal structure of an electrolytic capacitor. In an actual capacitor, the Anode/Cathode Foil and Isolated Paper are wound together to form many layers.

Conductivity Equation of the Winding Structure

By using FloTHERM® Electronics Thermal Simulation software, the thermal designer can set up a capacitor model following the actual structure, but this kind of model is not always

recommended, since it won't make the simulation more accurate. Instead, this kind of model increases both the grid density and cell count. A larger grid will result in a longer solve time.

To avoid these issues, the winding structure can be simplified while still retaining the model's accuracy. For this winding structure, if the layers were unwound, the internal structure can be simplified to a stacked structure as shown in Figure 2(b). Based on this simplified structure, the conductivity of the internal winding layer can be calculated by:

$$K_r = \frac{\delta}{\sum_{i=1}^n \frac{\delta_i}{K_i}} ; K_a = \frac{\sum_{i=1}^n K_i \cdot \delta_i}{\delta}$$

Eq.2 refers to the effective conductivity of multiple objects combined in series and in parallel. In Eq.2, K_i is the conductivity at radial direction, and K_a at axial direction. Obviously, the internal winding structure is anisotropic in terms of conductivity.

If the Anode Foil and Cathode Foil are made with Aluminum ($K=180W/m\cdot K$), and the Isolation Paper is a typical material which $K=0.035W/m\cdot K$, then $K_r=0.08W/m\cdot K$, and $K_a=90.02 W/m\cdot K$. In case of a different foil

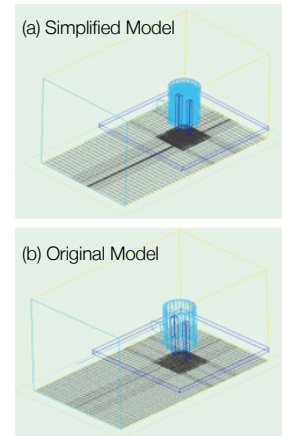


Figure 3. Grid of simplified model and original model

	Simplified Model	Original Model
Cell Quality	141,584	1,790,246
Max Aspect Ratio	7.33	35.10
Number of Iterations	350	750
Residual/Convergence	1 / Convergent	>10 / Divergent
Solving Duration	13m:55s	58m:21s

Table 1 Difference between simplified and original models

material, such as Tantalum, the capacitor's conductivity can be calculated accordingly.

Comparison of a Simplified Model and an Original Model

The simplified model is much better for solving than the original. The differences are illustrated in Figure 3, which also shows the grid of both models. Table.1 confirms the simulation parameters comparison, it is clear to see that the original model has a longer solving time and eventually becomes divergent.

CFD Model of a Capacitor

With the calculated conductivity of the internal winding structure, a capacitor with a PCB CAE model can be set up as shown in Figure 4. This model is used in the following study.

Capacitor Cooling Simulation

Based on the study earlier, the capacitor's power loss, PCB temperature, air velocity, and ambient temperature all impact the capacitor temperature. The following study verifies how each boundary condition impacts the capacitor temperature. The initial conditions are set to: power loss = 0.3W, PCB temp = 80°C, air velocity = 1m/s, ambient temp = 45°C.

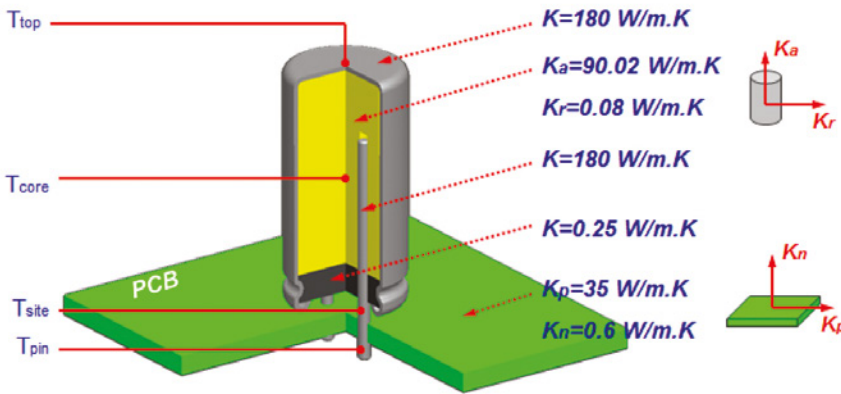


Figure 4. CFD model of a capacitor

In total, four scenarios were studied. In each scenario, three of these four conditions are held constant, while the other is variable so as to show how this condition impacts the capacitor temperature.

Figure 5 shows the solution domain for this study, a DIP (Dual In-line Package) type capacitor with a piece of PCB is placed in a wind tunnel, air flow in the wind tunnel is perpendicular to axis of the capacitor.

As a heat conductor and also heat source, temperature distribution on the capacitor body is not uniform, so the temperature of multiple points on the capacitor are monitored in the study, as follows: T_{top} , T_{core} , T_{side} , T_{pin} (Figure 4). T_{core} is the internal temperature of the capacitor so it is one of the key parameters for the capacitor lifetime evaluation, but T_{core} could not be measured in a real system. So T_{top} , T_{side} , T_{pin} are monitored, and temperature differences between core and top (ΔT_{ct}), core and side (ΔT_{cs}), and core and pin (ΔT_{cp}) were studied.

Variation in Capacitor Power Loss

The power loss was to vary from 0.2W to 1.2W, and the temperature trend of each monitor point was noted.

Figure 6(a) shows temperature trends of each point, T_{core} increases in accordance with the increase in power loss, but T_{pin} is not impacted by the power loss increase at all. T_{side} shows a slight change but keeps within a small range ($<5^{\circ}\text{C}$), T_{top} has an obvious increase and the trend is very similar to that of T_{core} .

Figure 6(b) shows the temperature difference trend between the core and other points. It results in ΔT_{ct} only has very slight change ($<1^{\circ}\text{C}$), while ΔT_{cs} and ΔT_{cp} have obvious change.

Variation in PCB Temperature

The PCB temperature was set to vary from 50°C to 100°C , and then the temperature trend of each monitor point was verified.

Figure 7(a) shows the temperature trend of each point, it appears all four points have obvious increases corresponding with the PCB temperature increase. This means the PCB temperature heavily impacts the capacitor's lifetime, directly conducting heat into the capacitor.

Figure 7(b) shows the temperature difference trend between core and other points. It results in ΔT_{ct} having a very slight change ($<1^{\circ}\text{C}$) while ΔT_{cs} and ΔT_{cp} have obvious decrease with the PCB temperature increase.

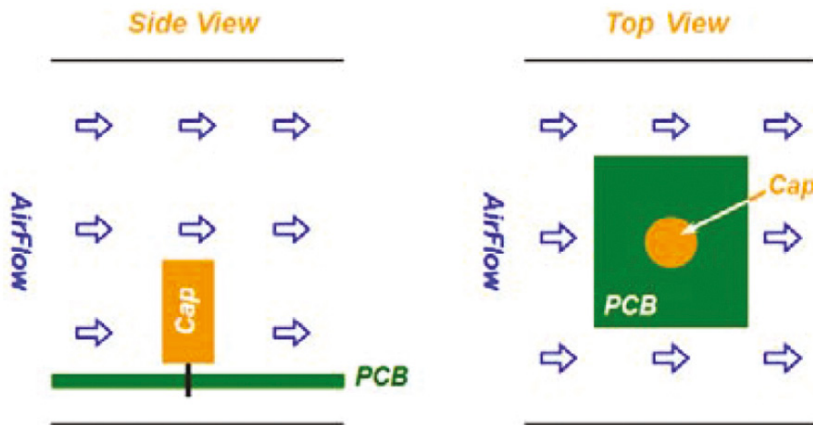
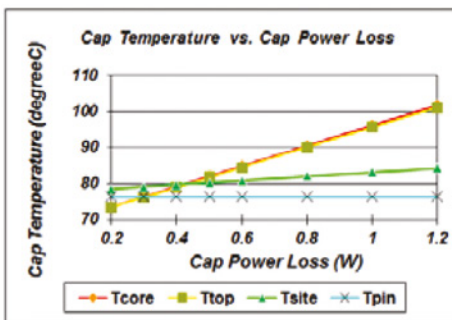
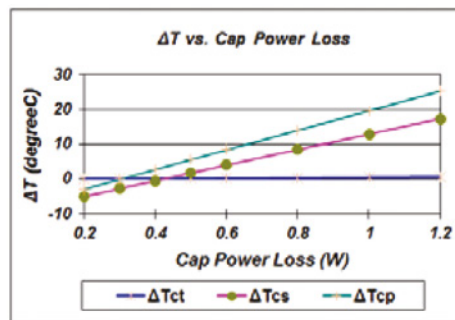


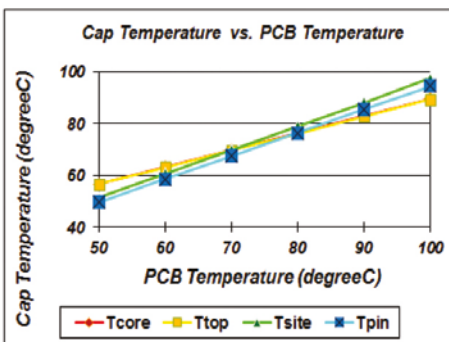
Figure 5. CFD simulation scenario



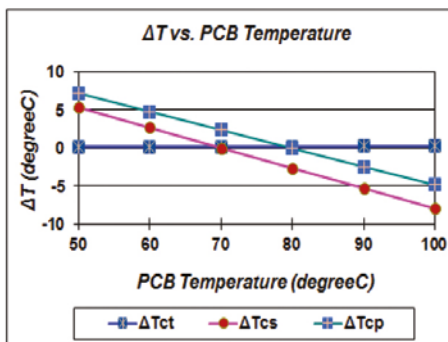
(a) Trend of temperature
Figure 6. Variable capacitor power loss



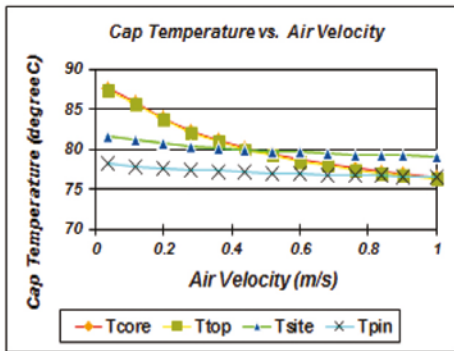
(b) Trend of temperature difference



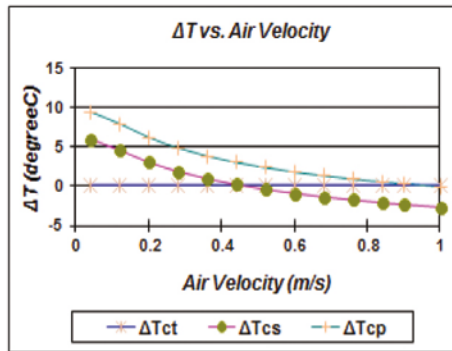
(a) Trend of temperature
Figure 7. Variable PCB temperature



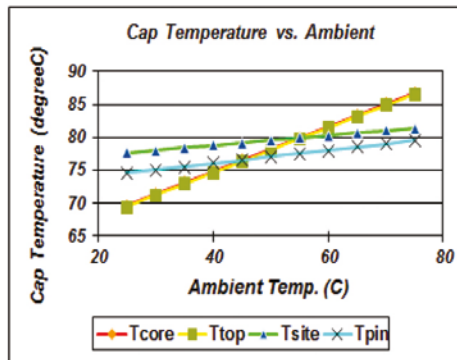
(b) Trend of temperature difference



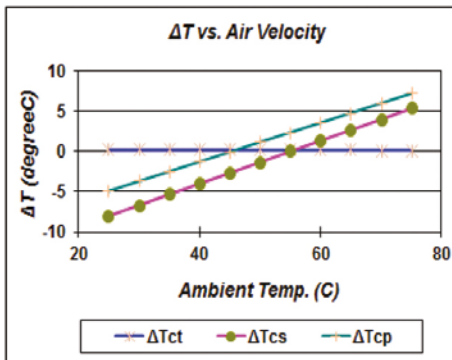
(a) Trend of temperature
Figure 8. Variable air velocity



(b) Trend of temperature difference



(a) Trend of temperature
Figure 9. Variable air velocity



(b) Trend of temperature difference

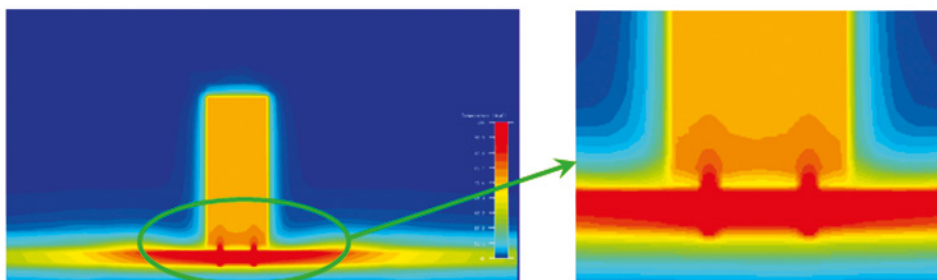


Figure 10. Capacitor temperature field in the FloTHERM simulation

Variation in Air Velocity

Air velocity was set to vary from 0.05m/s to 1m/s, and then the temperature trend of each monitor point was verified.

Figure 8(a) shows the temperature trend of each point, it appears T_{top} and T_{core} decreased in accordance with the air flow velocity increase. While T_{pin} and T_{site} slightly decreased.

Figure 9(b) shows the temperature difference trend between core and other points. It results in ΔT_{ct} also slightly changing ($<1^\circ\text{C}$), while ΔT_{cs} and ΔT_{cp} have obvious decrease with air velocity decrease.

Variable Ambient Temperature

Ambient temperature was set to increase from 25°C to 75°C, and then the temperature trend of each monitor point was verified.

Figure 9(a) shows the temperature trend of each point, it appears ambient temperature impacts the temperature of all points.

Figure 9(b) shows the temperature difference trend between core and other points. It results in ΔT_{ct} also slightly changing ($<1^\circ\text{C}$) only, while ΔT_{cs} and ΔT_{cp} have obvious increase with ambient temperature increase.

Temperature Measurement Point Study

In a real system, only the outside surface temperature of a capacitor can be measured, while, internal temperature is required for lifetime evaluation. So a proper measurement point which has a small deviation from internal temperature needs to be found.

Traditionally, some capacitor manufacturers recommend measuring pin temperature (T_{pin} in Figure 4) for a DIP type capacitor, as the pin is a high thermal conductor and is in contact with the capacitor internally. However, according to this study, the temperature difference (ΔT_{cp}) is not constant, so the pin temperature should not be used to reflect internal temperature. Figure 9 shows a capacitor's temperature field in the FloTHERM simulation. In this case the PCB temperature is higher, so the pin temperature (T_{pin}) will be also higher than internal temperature (T_{core}).

Figure 10 Capacitor temperature field in the FloTHERM simulation

According to the study, the temperature at the top of the capacitor case (T_{top}) is almost constant when boundary conditions change, so the top of the case is the best measurement point in the case where the airflow pattern is same as shown in Figure 4.

Conclusion

This study developed a simplified capacitor model for use in a CFD simulation. This simplification can improve grid density and quality in the simulation model, and thus improve the accuracy of the simulation. This study also identified all boundary conditions that impact the capacitor's cooling, and then verified how each boundary condition impacts the capacitor temperature. Referring to this study, the thermal designer can improve the capacitor cooling solution by optimizing boundary conditions.

Finally, the top case temperature (T_{top}) was determined as the best point to reflect the capacitor's internal temperature (T_{core}). Across the range of boundary conditions tested, the temperature difference between top and internal is constant and only around 1°C , so the system designer can easily convert the top case temperature to an internal temperature.

References

[1] GDDL, Cap lifecycle calculation template



**Alberto Deponti, Product Manager,
EnginSoft SpA**

Q. Tell us about EnginSoft and what the company does?

A. EnginSoft is an Italian company active in the field of simulation based engineering and science. In this framework we support companies in different industries that want to innovate their designs and production processes. Through vehicle prototyping, in particular, we collaborate with customers to find the best solutions for their problems. EnginSoft has over 120 highly qualified engineers and a global presence in countries across Europe and the US.

Q. What would you say are EnginSoft 's core strengths?

A. Aside from our global presence, we have a portfolio of around 42 engineering software solutions covering different industry sectors. However, I think that the most important strengths EnginSoft has, is represented by the competence of the people, as I said EnginSoft has more than 120 highly qualified engineers who each are able to solve problems in different industry sectors and across disciplines. I am indeed convinced that a complex problem can only be analysed with a multi-disciplinary approach.

Q. Which project, that EnginSoft has been involved with, are you most proud of?

A. Well this year we began a training course for the joint research centre of the European Commission. The aim of the project was to help the customer to implement a model for a uranium enrichment cascade. The complexity of the problem really pushed me to study a completely new topic and to find new techniques and innovative solution.

What makes me really proud of this project is the resulting consequences. The results of the simulation will help the Inspector of International Atomic Energy Agency

to detect any potential illegal diversion of nuclear material that could be very hazardous for nuclear weapon proliferation. This work has to do with the safety of us all.

Q. In the time you have been involved with simulation what is the biggest change you have seen?

A. Over the years, I have seen the computational power of hardware increase as well the capabilities of software but at the same time the complexity of systems has changed from a geometrical point of view, in the sense that systems are getting bigger. For example from a physical point of view, we have to face problems that have complex physics in systems of systems, taking into consideration the interactions between different systems. So we need to take a multi-physics approach as the complexity of the physics is increasingly becoming more multi-faceted.

Q. What emerging system simulations areas are you seeing in the industries you serve?

A. I would say that the study of mutual interaction between fluid and mechanical systems is the area I can see the most challenging requests and promising applications.

Q. What industry do you see that could benefit most from product simulation?

A. Well in my opinion, really every industry sector faces day-by-day challenges that can be analyzed and solved with simulation. Speaking about system level simulation, I would say that wherever there is a system, there is an opportunity for simulation. Consider any system, be it a

small engine cooling system in a vehicle or a huge distribution system that may be several kilometers long, each one could be part of or contain other systems, each of them can be analyzed and simulated in increase their efficiency, productivity, capacity, etc.

Q. Where do you see CFD going?

A. I can see two main emerging trends. One is to be able to simulate the complexity of the real world using a multi-physics approach. And two, customization. I think that there is an emerging desire from customers to have tailor-made solutions capable of modeling very specific problems easily and quickly.

ABOUT ENGINSOFT

EnginSoft was founded in 1984 and is a premier consulting firm in the field of Simulation Based Engineering Science (SBES) with a global presence. Throughout its long history it has been at the forefront of technological innovation and remains a catalyst for change in the way SBES and CAE technologies in general are applied to solve even the most complex industrial problems with a high degree of reliability.



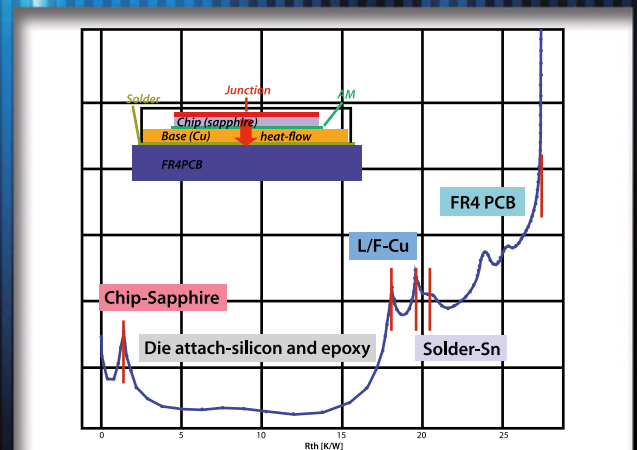
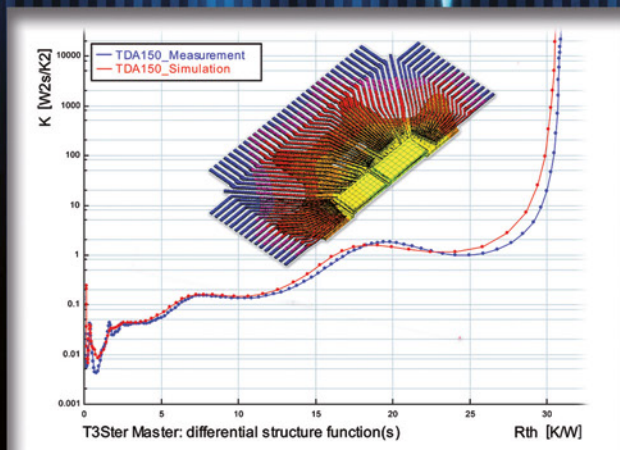
EnginSoft employs qualified engineers, with expertise in a variety of engineering simulation technologies including FEM Analysis and CFD, working in synergic companies across the globe. They have a global presence with offices present in Italy, France, Germany, the UK, Sweden, Turkey and the U.S.A. and have a close partnership with synergetic companies located in Greece, Spain, Israel, Portugal, Brazil, Japan and the U.S.A.

EnginSoft works across a broad range of industries that include the automotive, aerospace, defense, energy, civil engineering, consumer goods and biomechanics industries to help them get the most out of existing engineering simulation technologies.

More Information: enginsoft.com

T3Ster®: World Leader in Thermal Characterization of Electronics

ΔTSP recording



- **Rapid Thermal Transient Testing of Single and Stacked Die Packages and LEDs**
- **Non-destructive Component Failure Analysis**
- **Reliability Testing with Power Cycling and Subsequent Structure Function Analysis**
- **Connects to market-leading electronics cooling CFD simulation software, FloTHERM®**

JEDEC JESD51-14 compliant
 JEDEC JESD51-52 compliant
 MIL-STD 750E compliant



Mechanical Analysis





Layer by Layer

battenfeld-cincinnati use FloEFD™ to Model High-spec Extrusion Pipes

By Heinrich Dohmann and Carsten Bulmahn,
battenfeld-cincinnati Germany GmbH

battenfeld-cincinnati is a global extrusion systems manufacturer with production facilities in Bad Oeynhausen and Kempen (Germany), Vienna (Austria), Shunde (China) and McPherson, KS (USA).

Energy efficiency, conservation of resources and reduction of material consumption are topics that battenfeld-cincinnati has long been focusing on. As a member of the VDMA's Blue Competence Initiative [2] they play a part in promoting sustainable economic development. Their aim is to provide "leading solutions" to their customers, both in terms of performance and energy efficiency.

battenfeld-cincinnati manufactures energy-efficient, high-performance extruders and complete extrusion lines according to customers' specifications and has found practical, innovative solutions for developing components and tooling. battenfeld-cincinnati is the market and technology leader in Polyolefin (PO) pipe extrusion, particularly for large diameter pipes. Numerous projects for lines with diameters of up to 2.6 meters at a wall thickness of 100 mm have already been realized and successfully placed in the field. Other products include extrusion lines for smaller pipes which are used in telecommunications, where the smallest dimensions can be up to a diameter of 4mm at a wall thickness of 0.5 mm with an extrusion speed of up to 200 meters per minute, building services (such as underfloor heating), and automotive applications, among others. These can have several different layers and various color stripes.

For over a decade FloEFD 3D Simulation Software has supported battenfeld-cincinnati engineers in their product development. We met with Heinrich Dohmann (Head of R&D Pipe Heads and Mechanical Engineering Downstream) and Carsten Bulmahn (Mechanical Engineering Pipe Heads) from battenfeld-cincinnati. "The current short project lead times between ordering and hot-commissioning require the use of advanced simulation tools like FloEFD," explains Heinrich Dohmann.



Figure 1a. battenfeld-cincinnati supplies large diameter pipe lines with diameters up to 2.6 m (photo © battenfeld-cincinnati)

Designing and building large diameter pipe heads is a huge challenge. battenfeld-cincinnati is driven by a customer-centric approach to design solutions, whereby customers can select the most suitable pipe head for their specific application from a wide range of tooling options. In the early days, battenfeld-cincinnati used FloEFD for melt distribution optimization. The increasingly complex geometries could not be calculated with the available, reliable tools anymore. Hence, the implementation of a 3D simulation tool became necessary. In addition, a confidential development project in co-operation with an established pipe manufacturer was successfully developed with the usage of FloEFD. Since then, battenfeld-cincinnati has applied FloEFD to a wide range of applications to achieve a uniform velocity distribution in the annular gap at the melt die outlet. The challenge here is to optimize the pressure drop simultaneously. This can amount to up to 400 bar for the entire line and thus has a significant impact on the overall efficiency and the installation space required. The shear flow and the material dwell times have to be considered accurately at the same time.

One of battenfeld-cincinnati's innovative products is the high performance "helix VSI-T+" pipe die. With its two-step distribution concept, it is a highly efficient solution that has proven itself in more than 600 dies worldwide. It consists of a spiral mandrel and a lattice basket distributor element,

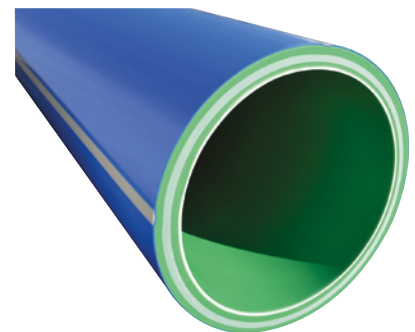


Figure 1b. battenfeld-cincinnati offers a variety of co-extrusion solutions and multi-layer pipe heads for special applications. Pictured: 4-layer PP-RCT-Pipe with glassfibre reinforced centre layer (photo © battenfeld-cincinnati)



Figure 1c. 5-layer PE-RT pipe with EVOH oxygen barrier layer (photo © battenfeld-cincinnati)

for which battenfeld-cincinnati holds the patent. Thanks to the two-step concept the melt is ideally distributed and optimally homogenized. This allows a smaller design for the distribution component, while at the same time ensures excellent pipe quality

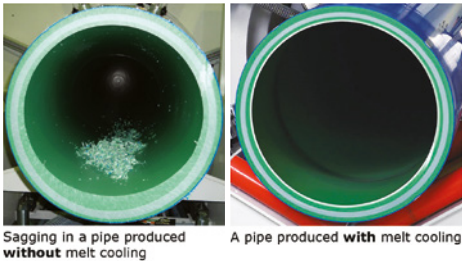


Figure 2. (© battenfeld-cincinnati)

and high outputs. With the help of PTC Creo embedded FloEFD, the battenfeld-cincinnati engineers give the pipe heads their ideal dimensions. Material flow channel and steel parts are designed compactly and efficiently. battenfeld-cincinnati's helix VSI-T+ die features active internal melt cooling to reduce melt temperatures already in the die and a reduced sagging effect, which is a big advantage in producing pipes with large wall thicknesses and a high line output.

The pipe head is one of the key factors for the customers. Its design and features ensures the production of large pipes with even wall thickness distributions and reduced pipe ovality. It also reduces sagging significantly (see figure 2). The efficient cooling concept allows for shorter cooling lengths in the line and thus enables space savings. The complete line components are custom-made and produced at battenfeld-cincinnati's manufacturing facilities.

Another application for the FloEFD flow simulations is in the development of multi-layer (co-extrusion) tools. In this process, several different layers are produced. In direct extrusion up to seven layers and in coating up to five layers can be produced. Various color stripes can be introduced into the pipe. The quality requirements are also very high in this case. Even the slightest deviations of the tone and thickness of the color stripes are not accepted. "In addition to the time optimization the simulation supports us in terms of product quality and reliability, such as at the color stripes. The detailed engineering is carried out within our development processes in the same team," says Carsten Bulmahn.

With CAD embedded FloEFD the battenfeld-cincinnati engineers can directly use the native 3D CAD data. The fluid space is automatically captured and the mesh is generated automatically from just a few settings within the software. Special calculation models for non-Newtonian fluids are applied for the simulation of the used materials. In this specific case the Carreau model is applied. The parameters for the non-Newtonian fluid model are determined on the basis of customer supplied material samples.

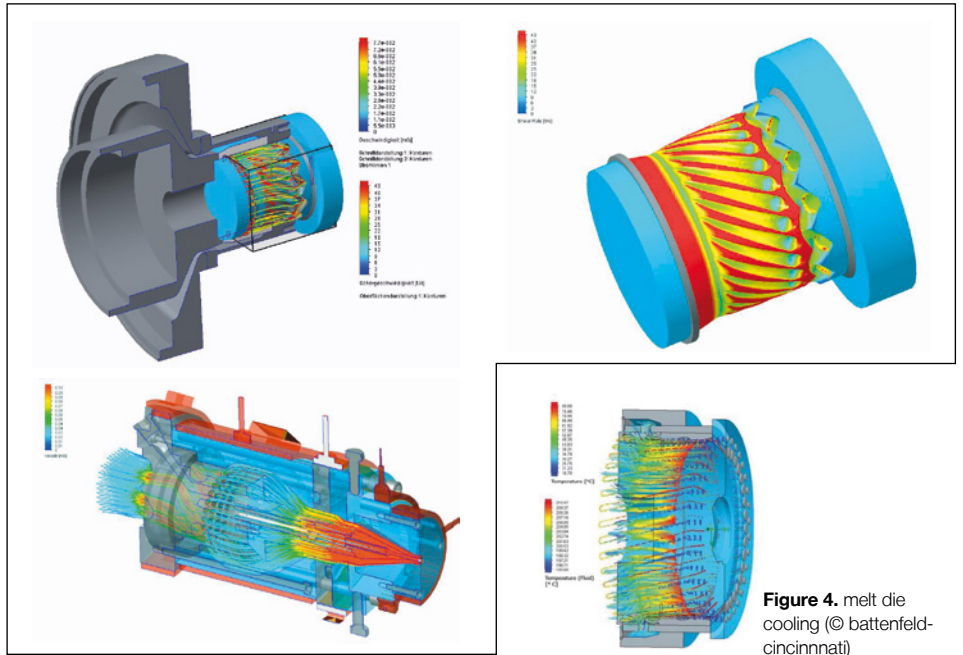


Figure 3a, b, c. melt flow through the melt die (© battenfeld-cincinnati)

Figure 4. melt die cooling (© battenfeld-cincinnati)

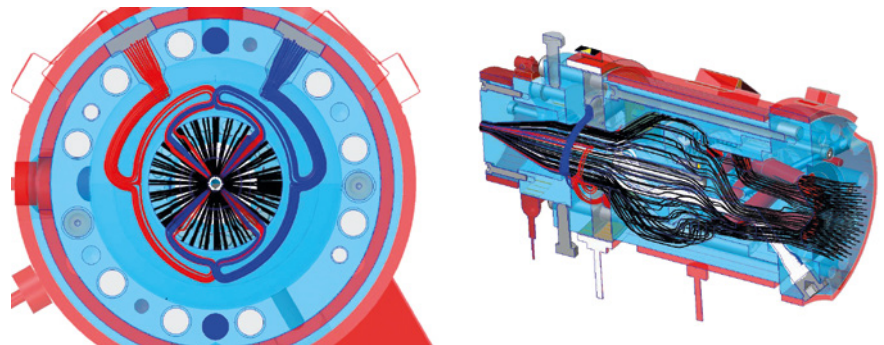


Figure 5a, b. Inner layer, middle layer (grey and black) and two color stripes (blue and red, depending on operating status) (© battenfeld-cincinnati)

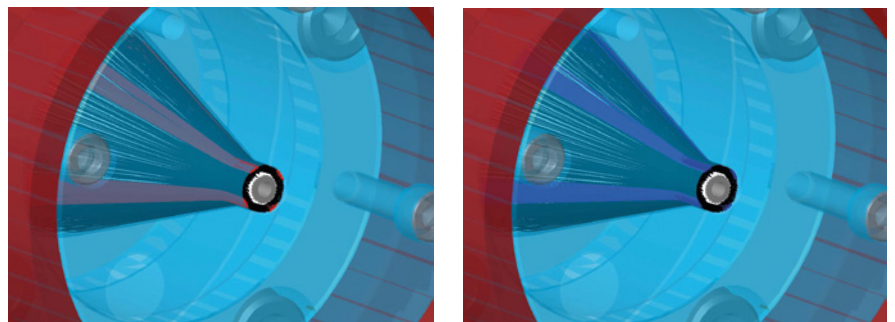


Figure 5c, d. melt distribution at the die outlet

Future conceivable applications where FloEFD might be used, are granulate preheating and pipe cooling. Both are examples of the energy optimization of the overall process. For granulate preheating the waste heat can be re-used in the process. The pipe cooling can already be ensured, but there may be potential for a further reduction of energy consumption and thus increasing overall efficiency in future.

early in the development process. Efficiency means savings of electricity and raw materials simultaneously.

References:

- [1] www.battenfeld-cincinnati.com
- [2] www.bluecompetence.net
- [3] <https://www.youtube.com/watch?v=vef7MvrOvt4>

In all of these challenges, FloEFD supports battenfeld-cincinnati's development engineers



Chongqing Changan Motors Optimize an Automotive Engine Lubrication System for a Variable Valve Lift System



By Boris Marovic, Automotive Industry Manager, Mentor Graphics.

As regulations drive the automotive industry to reduce emissions and fuel consumption, new technologies such as gasoline direct injection, turbocharging and variable valve lift (VVL) gain increased interest in automotive OEMs and Tier Suppliers. In particular the VVL meets the requirements for the control of the airflow at different engine revolution speeds and torques by reducing throttle pump loss, improving volume efficiency, optimizing in-cylinder gas flow, speeding up the combustion rate and many more advantageous behaviors.

As Wu Lifen and Yang Kun from Chongqing Changan Motors Powertrain Development Center work on optimizing the engine lubrication system with Flowmaster, they performed three studies with changes in the lubrication system of the original design. The project was conducted on a 1.6L 4-cylinder engine with a VVL system upgrade. The introduction of the VVL technology must not affect the engine lubrication so that an adequate oil pressure can be ensured for normal operation of the hydraulic VVL mechanism, as well as delivering sufficient lubricating oil to the bearing surface and enabling functions such as the hydraulic lash adjuster (HLA) and variable valve timing (VVT). This made the requirements of the engine lubrication system more stringent and an optimization essential in order to meet the requirements both for lubrication and for hydraulic driving.

Wu and Yang found that the space limitations for the oil passage of the cylinder head represented a major challenge. In order to maintain the lubrication of the bearing and the chain tensioner, as well as the normal operation of the VVT, HLA and VVL. Therefore multiple optimizations were made, including the addition of a throttle valve, change to the layout of the external circuit, adjustment to

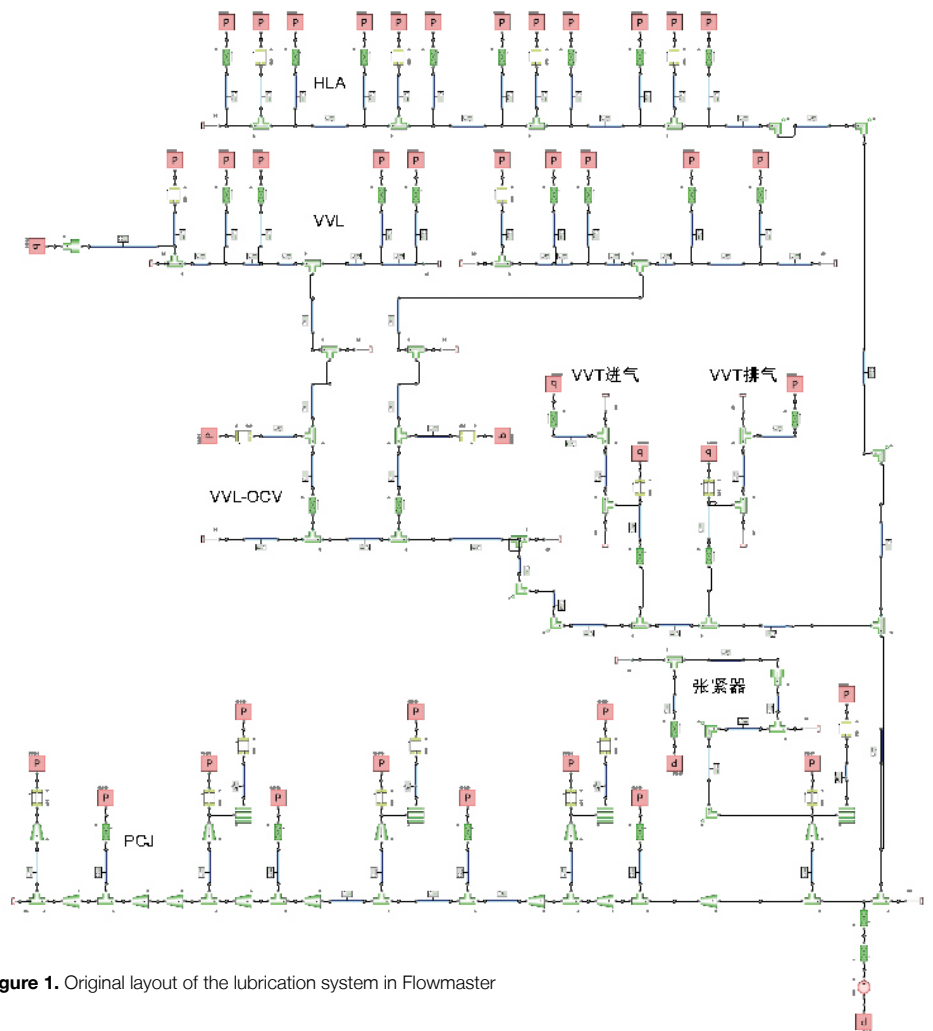


Figure 1. Original layout of the lubrication system in Flowmaster

the oil provision for the camshaft bearing, adjustment for the piston cooling jet (PCJ) opening pressure, adoption of the electronic VVT and optimization of the VVL control. This allowed the lubrication system to meet various requirements using the existing oil pump. The original layout of the simulation model in Figure 1 included a range of technologies such as the dual VVT intake and exhaust

system, the VVL intake system and the HLA. The system has to provide a certain pressure and flow rate through the oil passages from the oil sump and the oil pump to the oil filter, bearings, PCJ, VVT system, HLA, chain tensioner and VVL system. The simulation model considered simultaneous operation of the hydraulic system of the HLA, VVT and VVL with help of a 1D Flowmaster® model.

The two-stage VVL system uses a hydraulic drive to make the switch between high and low lift by changing the status of the locking pin. The default status of the locking pin of the system is the unlocked stage, which is the high-lift stage. In order to open the locking pin, a relative pressure of 1.75 bar is needed. In the initial VVL control strategy, the high-lift stage is from idling to 1,000 RPM and maintaining the high-lift stage from 1,000 RPM to 3,500 RPM. The dual VVT intake and exhaust system requires the phase locking pin to be turned on at a certain revolution speed, in order to withstand the internal friction torque of the VVT and the camshaft torque resistance, while adjusting the speed to meet the requirements. Once the engine is in hot idling mode, the internal check valve opening pressure of the HLA is reached.

Original Design

The simulation was conducted with SL5W30 oil at 130°C and each bearing clearance was set to the maximum clearance size. The initial evaluation of the original lubrication system in Figure 2 shows the HLA oil pressure requirement (orange) and the minimum VVL oil pressure requirement (red) as dashed lines. The original system does not meet the required pressures for the HLA at 750 RPM and also the oil control valve (OCV) inlet pressure at 1,000 RPM is not sufficient to drive the VVT into operation. The VVL inlet pressure is far below the 1.75 bar required.

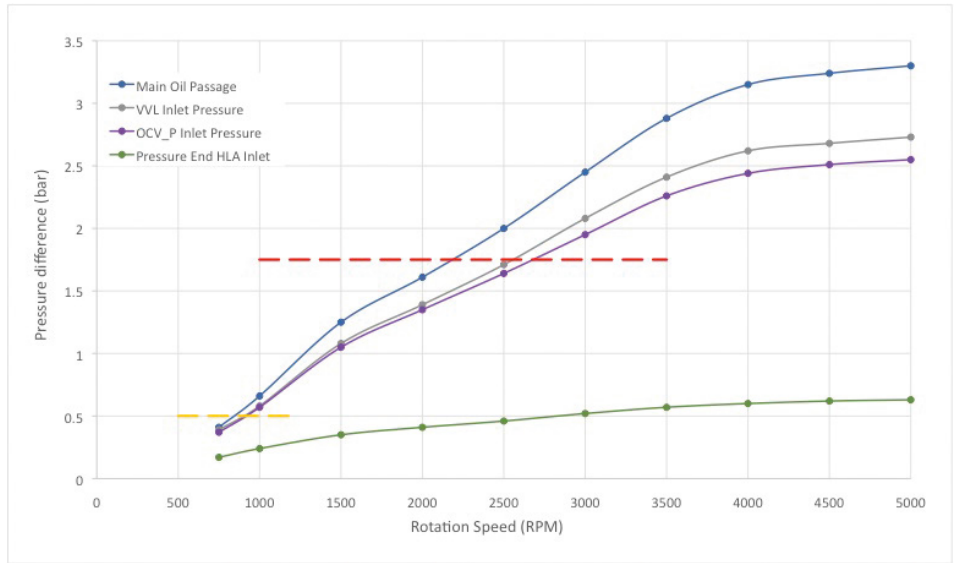


Figure 2. Oil Pressure of the Original Lubrication System



Figure 3. Showing 4-way pipe (left), Camshaft bearing oil provision (middle) and cylinder head oil passage fluid volume

The maximum pressure difference between the main oil passage and the VVL is approximately 2.5 bar. The overall VVL flow rate reaches 9 L/min when the pressure reaches 3 bar. This causes significant leakage and is also the cause of excessive low pressure at the VVL inlet end. The analysis showed that optimizations are required to reduce the flow rate through the VVL and reducing the pressure loss between VVL and the main oil passage.

Design 1

The Optimization Design 1 was achieved by introducing a 4-way pipe to the VVL for direct oil provision from the main oil passage, an optimized layout of the camshaft bearing feed to provide oil to the intake camshaft by the exhaust camshaft cover, the individual VVL test performance was updated and a 2.5 mm diameter hole (10 mm in length) was introduced into the exhaust camshaft inlet manifold to reduce the exhaust camshaft flow rate.

In the evaluation of the new design (Figure 4), the pressure at the HLA at 750 RPM

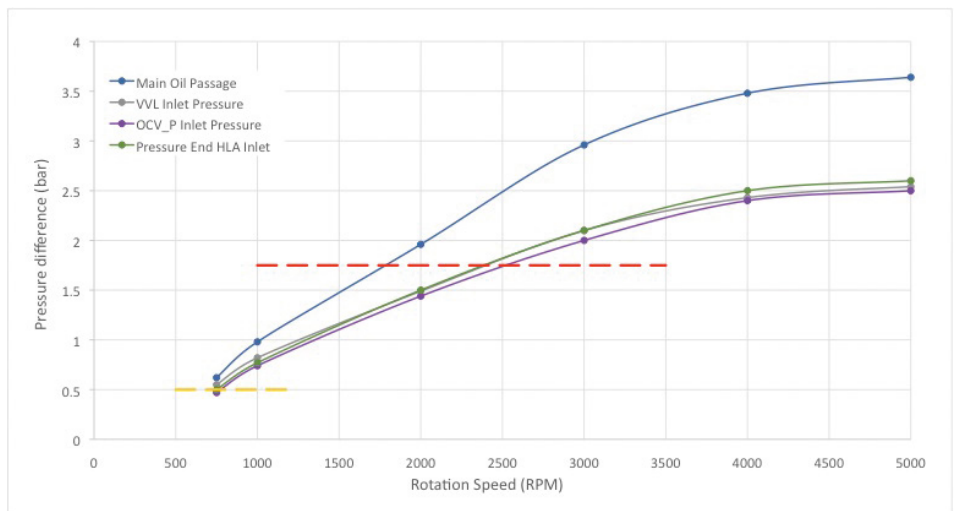


Figure 4. Lubrication system oil pressure in Optimized Design 1

meets the nominal operating conditions but the OCV pressure at 1,000 RPM is still not sufficient to drive the VVT into operation and the VVL pressure is also far below the 1.75 bar minimum to drive the VVL system into operation. The maximum flow rate through the external pipe reaches 9 L/min which is

equal to a pressure drop of 1.5 bar from the main oil passage to the VVL solenoid valve. The analysis also shows that the slotted design of the intake exhaust camshaft causes excessive camshaft leakage through the bearing clearance. Moreover, the oil fed through the exhaust camshaft journal



slot to the intake camshaft leaves room for hysteresis risk. The simulation clearly indicates room for more optimization of the lubrication system.

Design 2

In the Optimized Design 2, an integrated cylinder head cover was implemented to supply oil directly to the intake camshaft based on Optimized Design 1, the slot bearings were changed to bore bearings and the 4-way pipe was changed to a bolt hole oil passage as shown in Figure 5.

The evaluation of the simulation for the second optimization shows in Figure 6 that the HLA inlet pressure does not meet the operating requirements and also the OCV inlet pressure is not sufficient to drive the VVT into operation. The VVL inlet pressure reaches 1 bar at 1,000 RPM which is still below the 1.75 bar baseline and therefore unable to drive the VVL system into operation.

Design 3

Since the optimization of the lubrication system piping was unable to meet the pressure requirements of the VVL system in the first two design optimizations, a new strategy was introduced. For the new strategy the initial PCJ spray pressure was adjusted to 2 bar, the VVT system was upgraded to an electronic controlled system and the oil pressure setting of 1.75 bar was increased to 1,500 RPM to meet the requirements of the VVL control strategy.

The simulation results in Figure 7 shows that the HLA inlet pressure is sufficient to drive the HLA into operation and the VVL pressure reaches 1.9 bar at 1,500 RPM, which surpasses the 1.75 bar requirement and is therefore able to drive the VVL system into operation.

The simulation with Flowmaster and its ability to quickly implement design changes enabled Wu and Yang to find the optimum design with only few changes. It was found that the slotted design of the intake and exhaust camshafts causes excessive leakage through the bearing clearance and that changing the slot to a bore bearing will reduce the reliance on an oil pump. It also showed that an external oil passage with an elongated design will cause a high pressure loss for high flow rates. With some adjustments of the system such as the PCJ spray pressure, the adoption of an electronically controlled VVT and the VVL control strategy, the new design will significantly impact the performance.

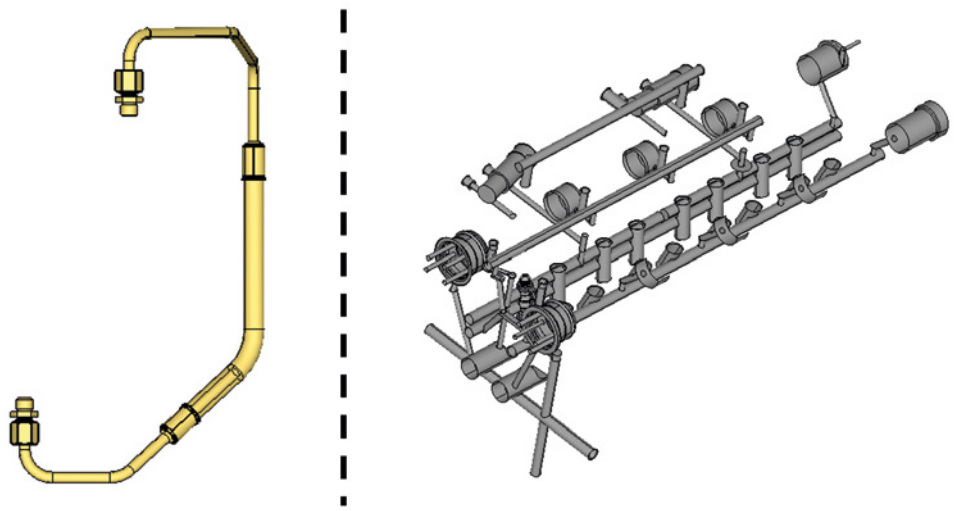


Figure 5. Showing bolt hole oil passage (left) and the changed oil feed in the cylinder head fluid volume.

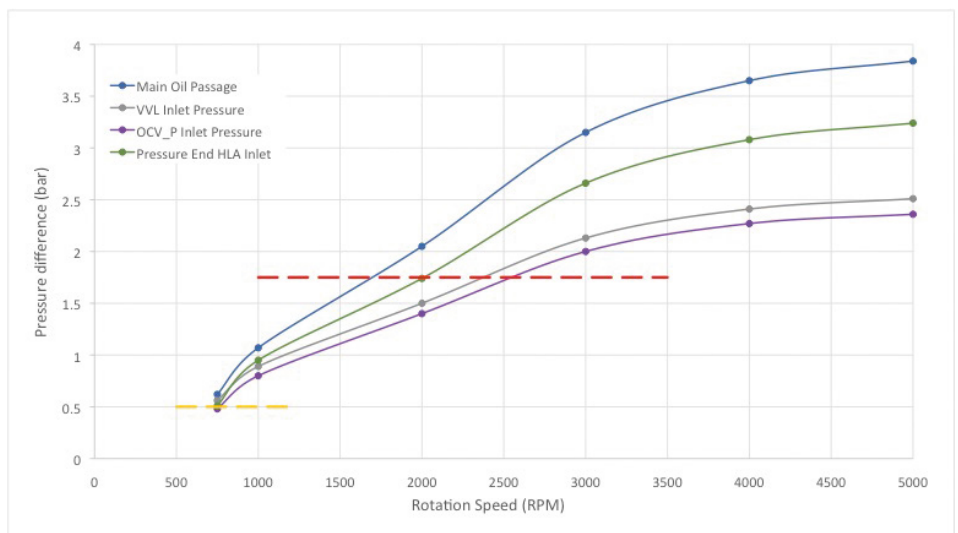


Figure 6. Lubrication system oil pressure in Optimized Design 2

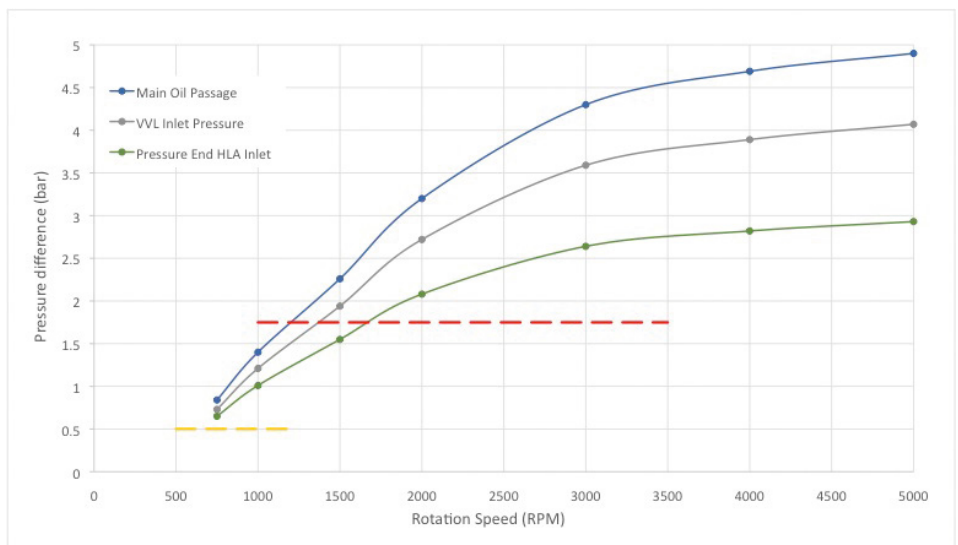


Figure 7. Lubrication system oil pressure in Optimized Design 3

Dynamic Compact Thermal Model Development within ROHM Semiconductor



By John Wilson, Technical Marketing Engineer, Mentor Graphics.

It is commonly accepted that two of the trends in the electronics industry are miniaturization and the electrification of all things. As a result electronics today are deployed into dynamic and sometimes harsh environments. As the environments have changed, so have the requirements for the system integrators. Today, companies need IC package models that can accurately predict dynamic thermal performance.

Currently there is no standardized methodology for developing a dynamic compact thermal model (DCTM) though there are important elements that exist. At ROHM Semiconductor Co., Ltd. well established standards and processes have been extended to meet the needs of their customers. They are able to provide validated DCTM models that facilitate more robust designs in a shorter amount of time. ROHM is coordinating with JEITA to provide a standardized approach to DCTM development.

Measure and Calibrate

The initial step in the process is to accurately measure the transient behavior of the IC device to calibrate a detailed thermal model. The T3Ster[®] Thermal Tester and FloTHERM[®] CFD Thermal Analysis software both from Mentor Graphics, were used to measure and calibrate the thermal model. Figure 1 compares the Structure Function of the measured device with the FloTHERM analysis

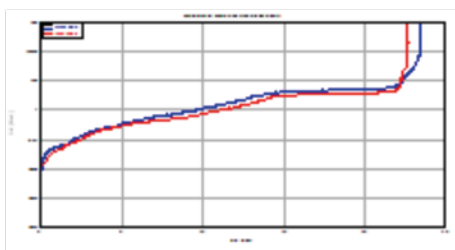


Figure 1. Structure Function Comparison IC Model

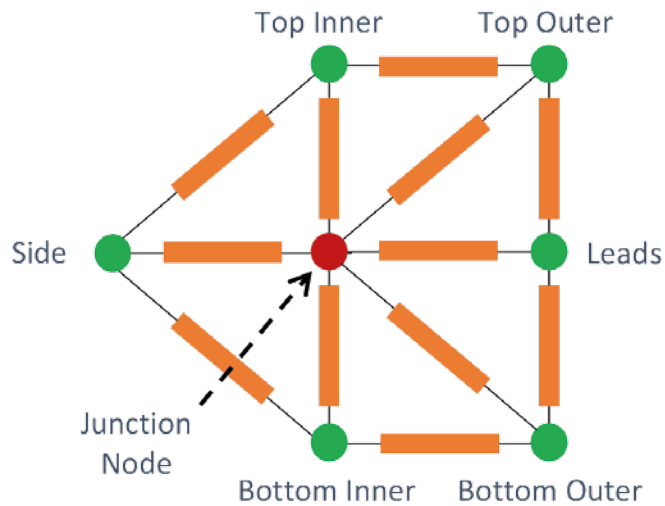


Figure 2. DELPHI Resistor Network of an IC model

model. The Structure Function is derived from the transient thermal measurement and represents the thermal resistances and capacitances along the heat flow path. A model calibrated against the Structure Function is valid for any transient scenario.

DELPHI Compact Thermal Model

Though the detailed model provides value to ROHM Semiconductor for internal design processes it doesn't represent the preferred method for use in system level thermal design. Detailed IC models represent a significant computational expense and also expose internal packaging details. The calibrated detailed model was used to develop a DELPHI compact thermal model (CTM). FloTHERM PACK was used to develop the DELPHI model from the calibrated detailed model. Figure 2 shows the DELPHI resistor network of the HTSSOP-B24 with the node locations shown in figure 3.

Modified DELPHI CTM Development

The DELPHI CTM was tested in an environment and was determined that representing the die with one node wasn't sufficient to capture the

local heating present on the die. A modification to the network was made as shown in figure 4. With the additional resistors the accuracy in junction temperature prediction was reduced from 33% to within 1%.

Modified DELPHI DCTM Development

The final step in the development of the DCTM was to add capacitance to nodes within the network. Capacitance was added at the nodes, shown in figure 5, and were based on the physical properties on the detailed IC model.

A comparison of the transient response between the detailed thermal model and the modified DELPHI DCTM is shown in figure 6. Overall the correlation between the two is quite good with the DCTM Junction temperature matching the detailed model at 2% difference at the end of the transient, or overall thermal resistance. The behavior of the temperature response during the transient is captured by the DCTM as well.

Summary

To design electronics for the dynamic world

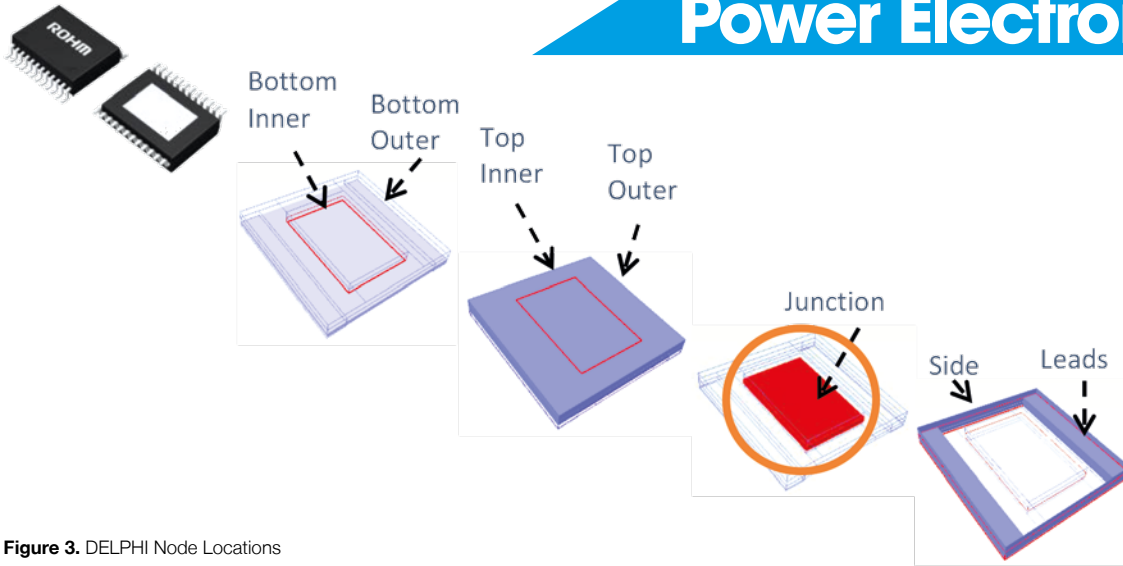


Figure 3. DELPHI Node Locations

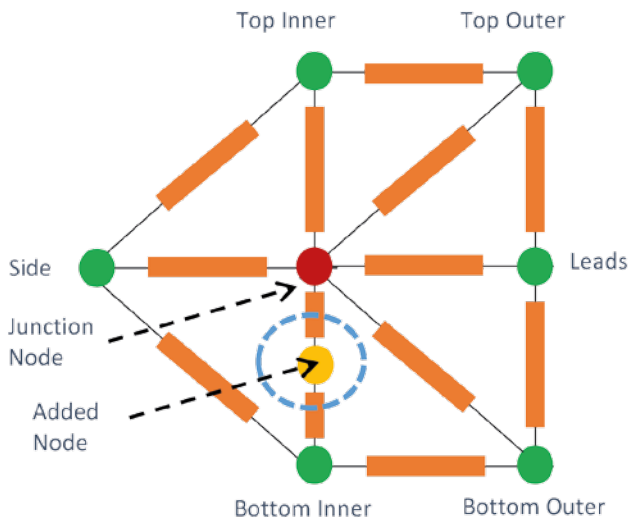


Figure 4. Modified DELPHI Resistor Network

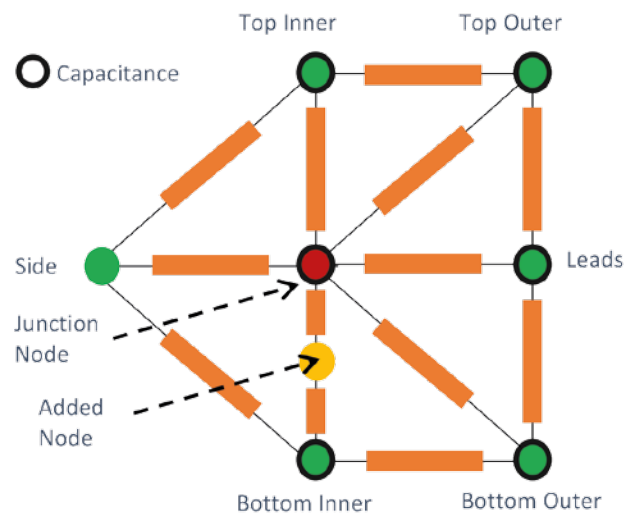


Figure 5. Modified Delphi Network Capacitance

we live in we must understand their dynamic behavior, with the IC component as an integral part. With T3Ster hardware and the Structure Function the transient response of IC packages can be accurately measured which is supported with standards. The development of a DELPHI CTM is outlined through standards, with the first requirement being to start with a validated detailed model. Currently there are no standards regarding the development of a DCTM. Though there is no standard, ROHM Semiconductor has implemented a process to develop a DCTM to a quantified degree of accuracy that allows their customers to design in a dynamic world. The process used by ROHM is not only benefiting their customers but also used in a collaboration effort with JEITA to develop a standardized approach to DCTM development.

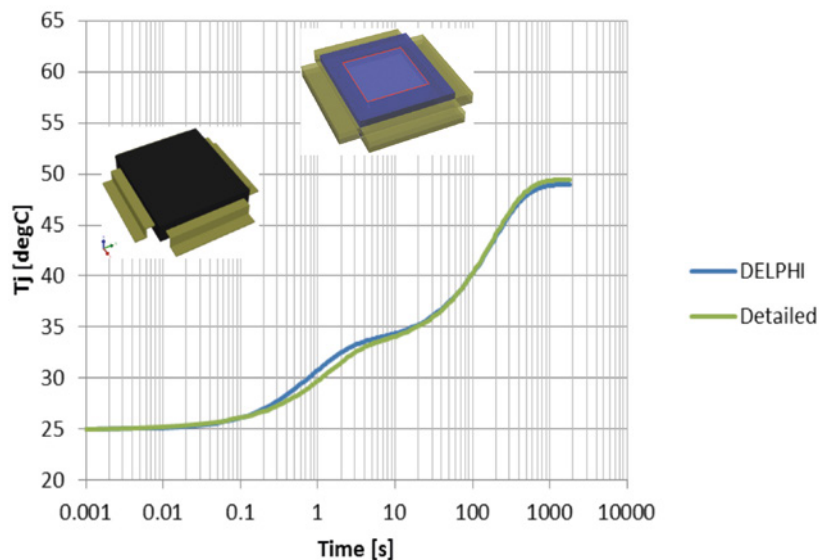


Figure 6. Junction temperature vs. time comparison

About ROHM

ROHM Semiconductor is an industry leader in system LSI, discrete components and module products, utilizing the latest in semiconductor technology. ROHM's proprietary production system, which includes some of the most advanced automation technology, is a major

factor in keeping it at the forefront of the electronic component manufacturing industry. In addition to its development of electronic components, ROHM has also developed its own production system so that it can focus on specific aspects of customized product development. ROHM employs highly skilled

engineers with expertise in all aspects of design, development and production. This allows ROHM the flexibility to take on a wide range of applications and projects and the capability to serve valuable clients in the automotive, telecommunication and computer sectors, as well as consumer OEMs.

Optimizing an Automotive Air Handling Unit for Uniform Temperatures using FloEFD™

By Lu Ping, Pan Asia Technical Automotive Center, Shanghai, China

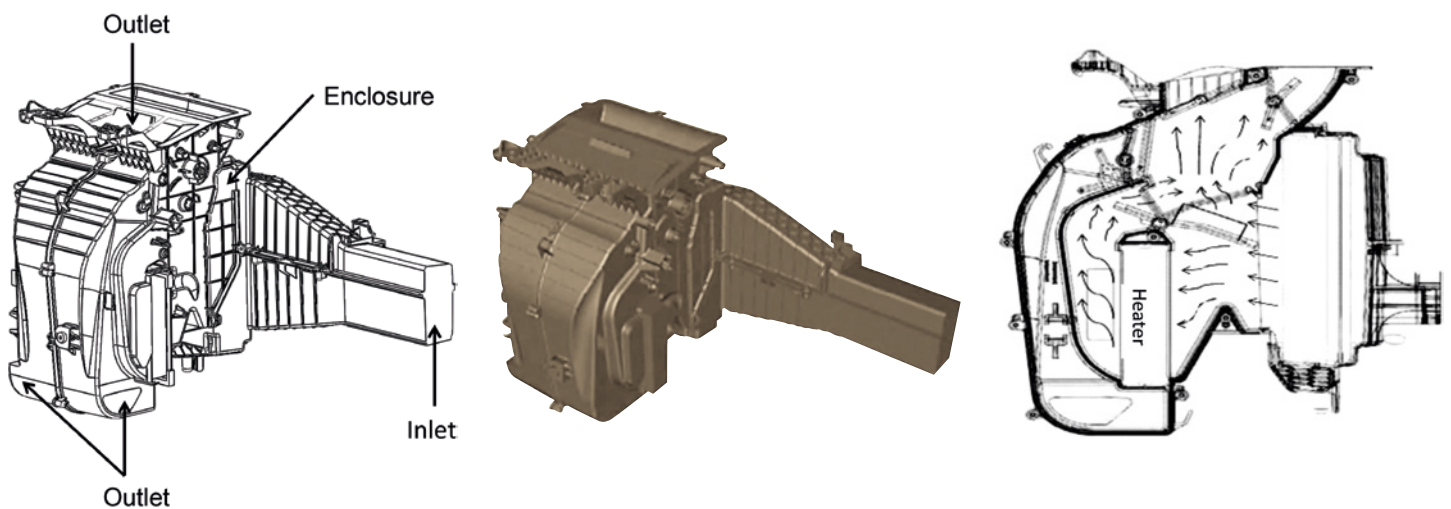


Figure 1. AHU geometry, its CAD Model, and a Sectional Schematic of Airflow Paths through it

The number of car owners in China is increasing exponentially. China will soon have nearly as many drivers as the U.S. With this band of newly qualified drivers, a demand for higher standards in vehicle ride “comfort” is developing. One such area is the standard of cabin comfort. This is directly related to a car’s air-conditioning unit with discharge temperature uniformity which is one of the key factors impacting perceived comfort levels.

On the one hand, discharge air temperature from the HVAC air box has to be uniform for passenger comfort, but on the other, uniformity can reduce the extent of the automatic air-conditioning calibration workload. However, due to packaging limitations in typical vehicle development, its air conditioning unit has to be as compact as possible, which usually make it a poor or inadequate mixture of cold and hot airflow inside the air conditioning unit and finally leads to a non-uniform discharge temperature. In the development of automotive HVAC air handling units (AHU), to control the discharge air temperature uniformity, performance is

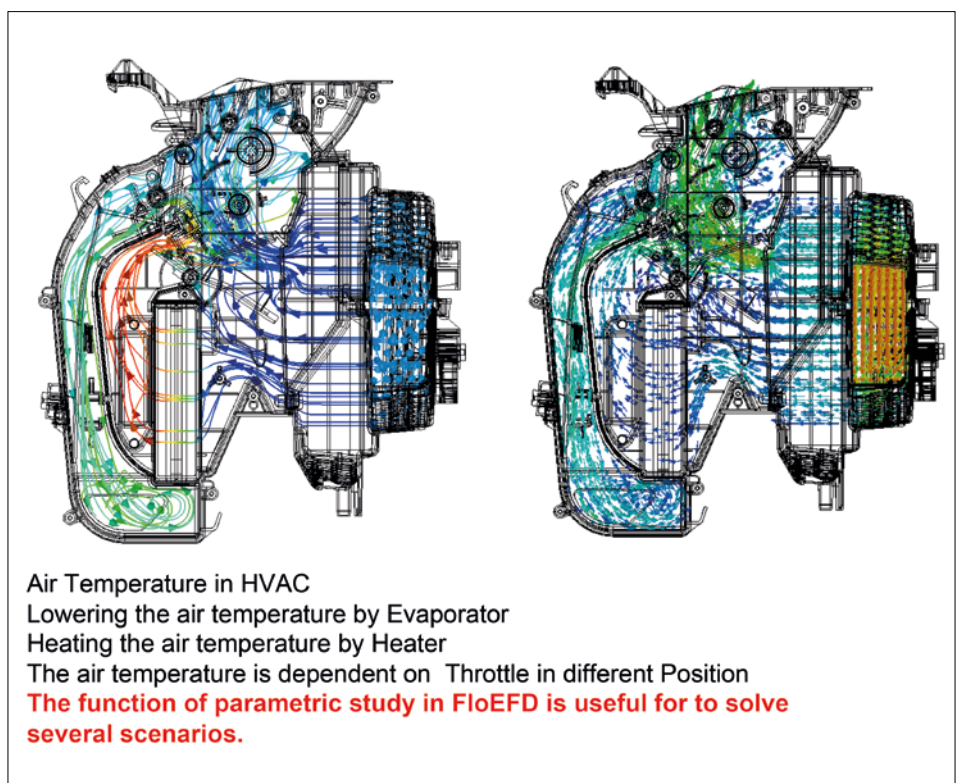


Figure 2. FloEFD predictions of airflow Vectors (right) and Temperature Distribution (left) inside the AHU



Temperature flap door in different position

Throttle in different Position

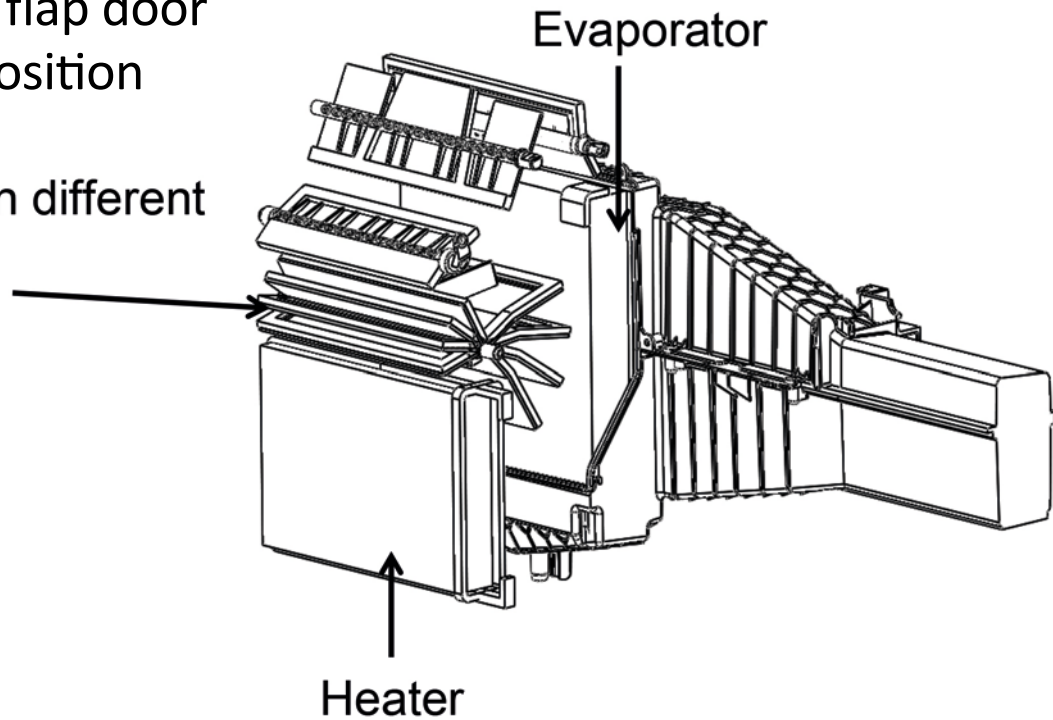


Figure 3. Air Handling Unit geometry showing details of the Evaporator, Heater and Temperature flap door under different positions

key, and it is important to consider the factors mentioned above for the development of a car's HVAC air handling unit (AHU).

Figure 1 shows the specific AHU being evaluated in this study. Flow through it involves complex tortuous passageways and the mixing of both cold and hot airflows. The unit has one inlet and two outlet zones, and its complex geometrical nature means that it is most realistic to simulate fluid flow and heat transfer inside a CAD package using a CFD tool such as FloEFD. The AHU itself consists of air box housing, an evaporator, a heater, and flap door components. During normal operation, airflow enters the air conditioning unit through the intake housing, and then flows through the evaporator to be cooled down. After cooling, the airflow partially goes through the heater core to be warmed up while part goes towards the outlet area with the flow guiding of a temperature flap door. These two hot and cold air streams then re-converge and mix to achieve a proper and comfortable temperature. Conditioned airflow is finally delivered to passengers through the air box outlet. A typical FloEFD simulation prediction for airflow vectors and temperature effects inside the AHU is shown in Figure 2.

The position of the temperature flap door effectively acts as a control valve inside the unit and ultimately determines the hot and cold airflow "mixing ratio". It can be altered

	Runner Hedge Angle (°)	Runner Area Ratio (%)
Case 1	120	44
Case 2	120	49
Case 3	120	39
Case 4	116	44
Case 5	116	49
Case 6	116	39
Case 7	124	44
Case 8	124	49
Case 9	124	39

Table 1. The nine AHU CFD Simulation Scenarios examined in this study

to different positions (Figure 3). The "hedge angle" and "area ratio" of the cold and hot airflow channel have an important influence on the final mixed airflow temperature distribution.

The CFD boundary conditions simulated in this AHU study extended from airflow rates of 15l/s to 60l/s at an air inlet temperature of 20°C with 875W heat transfer rate from the heater component. Nine parametric

CFD simulations inside FloEFD were used to determine an optimized cold and hot flow channel "hedge angle" together with runner "area ratios" as shown in Table 1.

This parametric study focused on the AHU outlet airflow temperature distribution under different temperature flap door setting. More focus is around the middle position, that is, for angle degree of outlet damper door

from 25° to 50°, considering the middle position is relative to a customer's actual high frequency usage scenario (see Figure 4). The temperature difference is seen to be optimal for Case 3 for the two temperature flap door conditions. Hence, the cold and hot airflow channel hedge angle and runner ratio area under this case is the most ideal which was verified visually (Figure 5) by outlet CFD temperature contours under these two temperature flap door positions.

Finally, we validated the CFD simulation Case 3 prediction against an experimental test of the actual car AHU. We chose an air conditioning box inlet temperature of 0°C, and the heater inside operating with a 90°C fluid so as to replicate a real vehicle use of air conditioning over cold and hot atmospheric conditions. By adjusting the temperature flap door in the AHU to control air-conditioning of cold and hot air mixing, we were able to verify the box's linear temperature uniformity performance target. We positioned 4 thermocouples on each outlet and measured the average exit air temperature. Figure 6 shows the actual measured performance data of the AHU. Aligned with the CFD simulation results, we achieved the maximum temperature difference within 4°C among four vent outlets when the temperature flap valve is adjusted between 35% and 65%. We reached the requirement of a linear thermal design, while at the same time it was basically consistent with the virtual design CFD results.

In conclusion, we adopted the commercial CFD software, FloEFD, for this study because of its ease of use in meshing when compared to the tetrahedral or prismatic meshing approaches in traditional CFD codes. We found that FloEFD gives more accurate and more efficient CFD simulation results. Since it works within the mechanical CAD environment, it is a highly engineered universal fluid flow and heat transfer analysis software. FloEFD was able to examine a range of AHU hedge angles for hot and cold airflow channels. The hedge angle and area ratios of 120° and 39% respectively were found to be the most optimal. FloEFD with its parameterized calculation function was highly efficient in varying a range of AHU parameters that we studied. It showed great design performance improvements in terms of achieving an optimized design while at the same time reducing our overall cost of development.

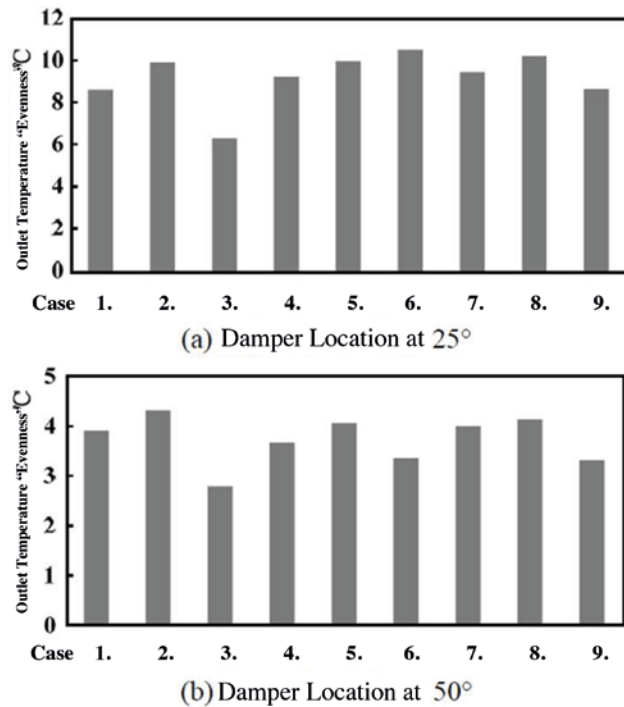


Figure 4. CFD predictions of Outlet Air Temperature "Evenness" for the nine different hedge ratio Cases at two Temperature Flap Door Angles

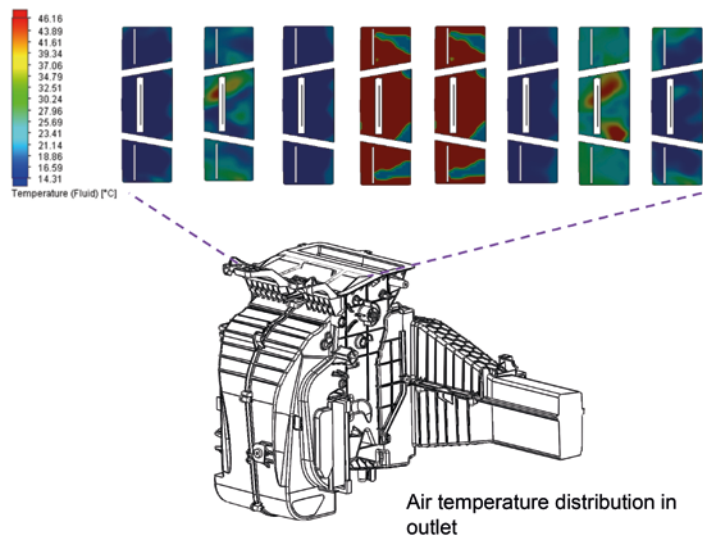


Figure 5. Air Handling Unit predicted Air Temperature Contours in the outlet face for the different hedge ratios

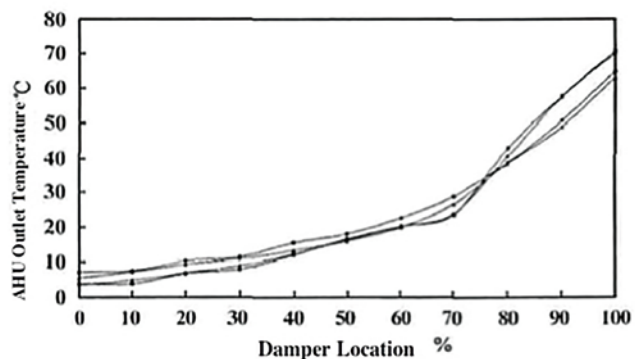


Figure 6. Data from four experimental Thermocouples of Outlet Air Temperature versus Temperature Flap valve Location for Case 3



Flowmaster Simulation Helps European Nuclear Safeguards Activities



By Mike Croegaert, Industry Vertical Manager, Mentor Graphics

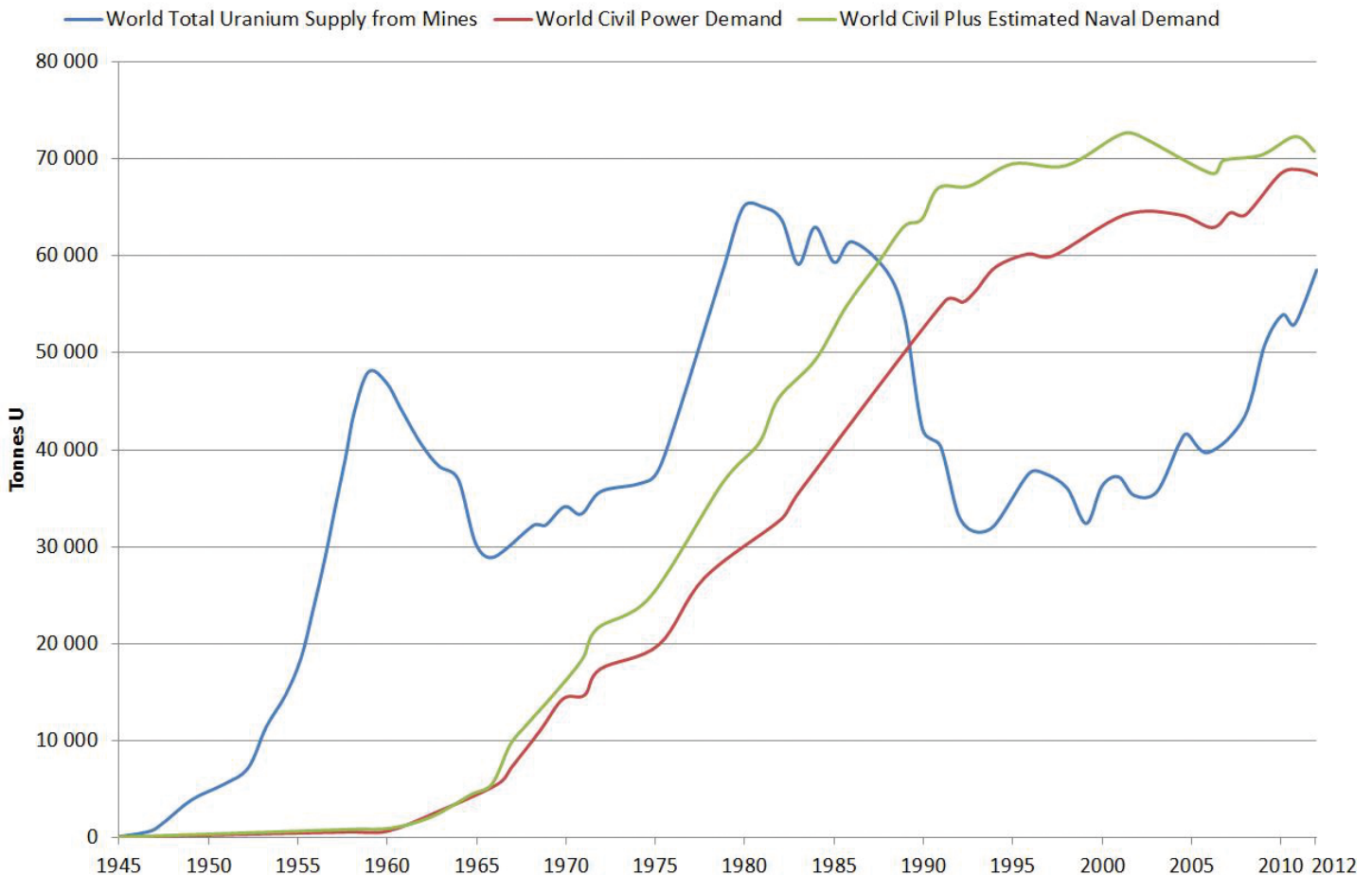


Figure 1. World uranium production and demand trends.

The increasing world energy demand and concerns over CO₂ emissions have led to the search of sources alternative to coal and gas. The continuous increase of uranium production and demand (Figure 1) indicates that nuclear power is seen as a valuable alternative source. Indeed, China, India, South Korea, and

Russia remain committed to it even after the Fukushima accident and the global uranium demand forecast indicates a long-term growth.

In the world today, there are about 500 commercial nuclear power reactors operating or under construction, most of which require uranium enriched in the U-235

fissile isotope for their fuel. One of the most widely used technologies for enriching uranium is represented by centrifugation of gaseous uranium fluoride. In gas centrifuge enrichment plants, hundreds or even thousands of centrifuges are arranged in cascades. Each cascade is made up by stages containing a certain number of centrifuges (Figure 2).

News in recent about the Iranian nuclear program has clearly shown how uranium enrichment is a sensitive technology from a non-proliferation point of view because it can be used for producing atomic weapons as well as fuel rods. For this reason uranium enrichment activities need to be subject to tight international control.

Most countries participate in international initiatives designed to limit the proliferation of nuclear weapons. Nuclear safeguards are measures to verify that states do not use nuclear materials to develop weapons and that they respect their obligations under international non-proliferation treaties. The European Union has set up a system of nuclear safeguards under the Euratom Treaty. In this framework, The Nuclear Security Unit of the Institute for Transuranium Elements at the Joint Research Centre (JRC) Ispra provides research, technology, instruments, technical services and training to the inspectors of the International Atomic Energy Agency (IAEA). The Non Proliferation analyses of Gas Centrifuge Enrichment Plants make regular use of advanced numerical modeling techniques supported and/or validated with data acquired during field inspections.

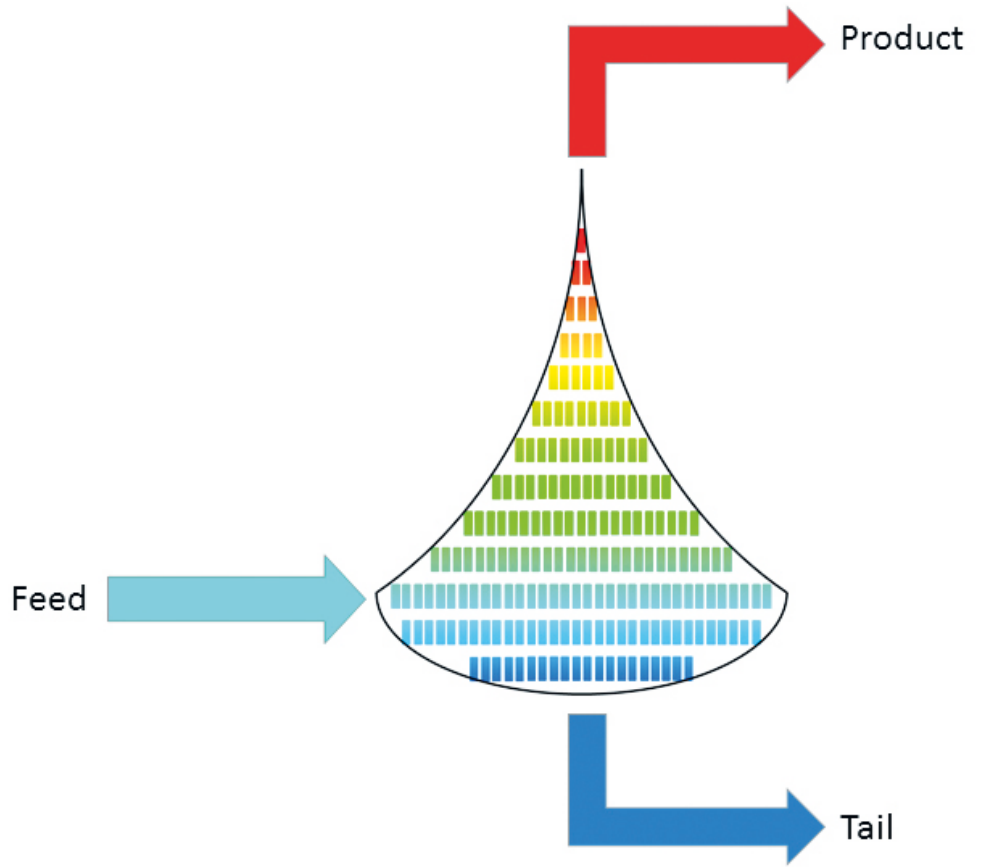


Figure 2. Schematic representation of a centrifuge cascade for uranium enrichment.



Figure 3. Example of a gas centrifuge enrichment plant.



By adopting this approach, normal and off normal conditions can be tested at an early stage improving the odds of a timely detection of eventual misuses or diversions of Nuclear Materials.

The numerical simulation of Gas Centrifuge Enrichment Plants presents many important challenges:

- Fluid properties: uranium hexafluoride is a heavy gas, having a density about 10 times larger than air;
- Flow conditions: the system works at low pressure (around 500 Pa) and with extremely small flow rates, in the order of micrograms per seconds;
- System complexity: plants contains hundreds or thousands of centrifuges;
- Physical complexity: the isotope separation process takes place in centrifuges spinning at hypersonic velocities.

A system level fluid-dynamic approach was implemented using the advanced 1D System Simulation tool, Flowmaster® from Mentor Graphics. Flowmaster was chosen because it had the advantage of mass accumulation in the piping system and the time lag that can be associated with the mass in the pipes. This was critical for accurately predicting the concentration of uranium entering the centrifuge. In order to model the complexity of the system, several custom components were implemented into the library. The most important one is the component capable to model a single centrifuge or a single stage of the cascade by providing the separative power of the centrifuge as a function of gas flow rate and the number of centrifuges in the stage.

The preliminary simulations performed on simplified network models (Figure 4) show that a system level approach is capable to model the main features of a uranium enrichment cascade on workstations in times ranging from a few seconds to a few hours depending on the length of the simulated times. In particular, the model allows a reliable estimation of the cascade separation performances under different operating conditions opening the way to effective simulations of misuse and diversion scenarios.

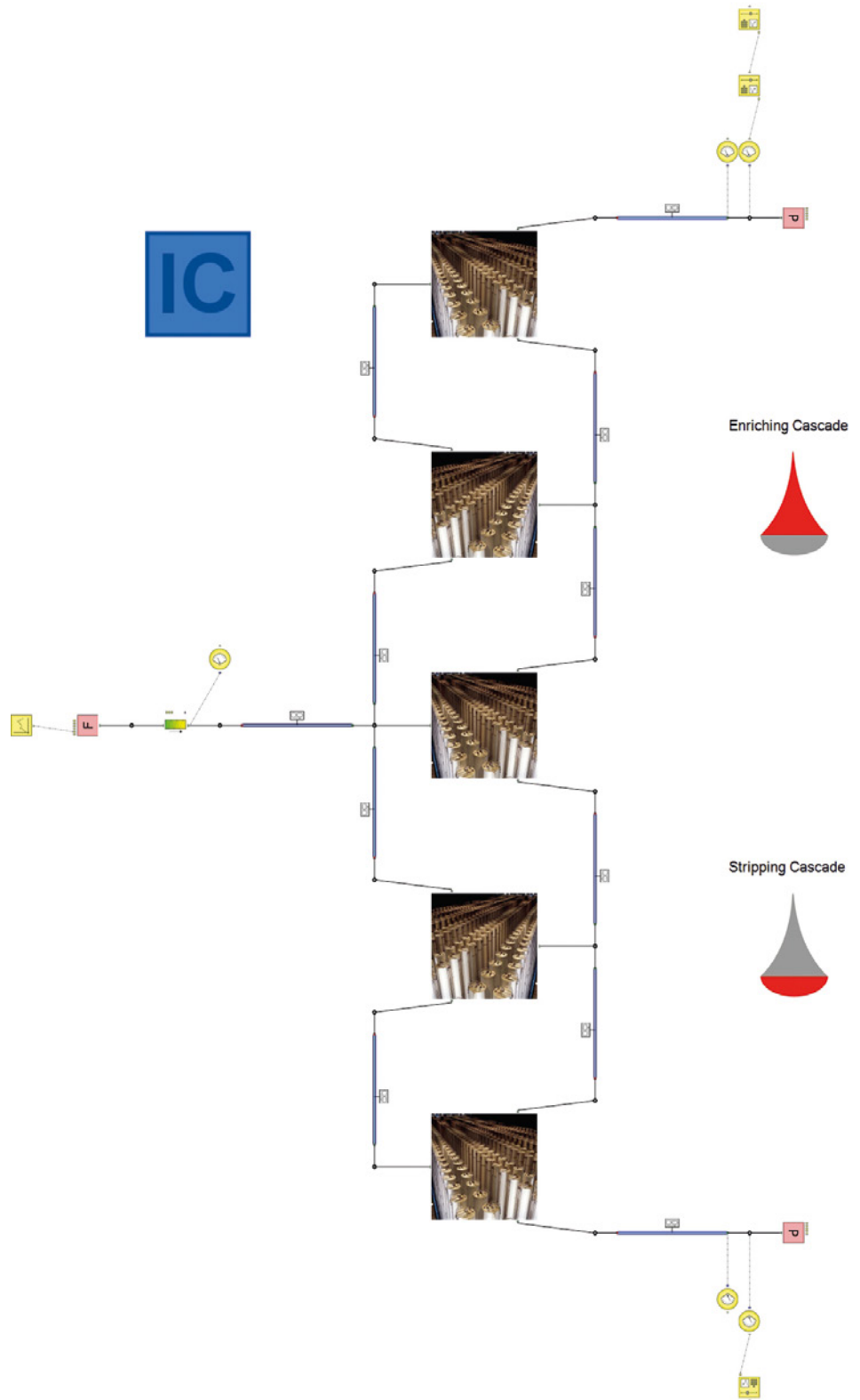


Figure 4. Network model of a 5-stage cascade implemented in Flowmaster.

Steering Towards Flow Optimization

FloEFD™ is an established part of the development process at Robert Bosch Automotive Steering GmbH

By Rolf Haegele, development engineer acoustics / simulation, Robert Bosch Automotive Steering GmbH.

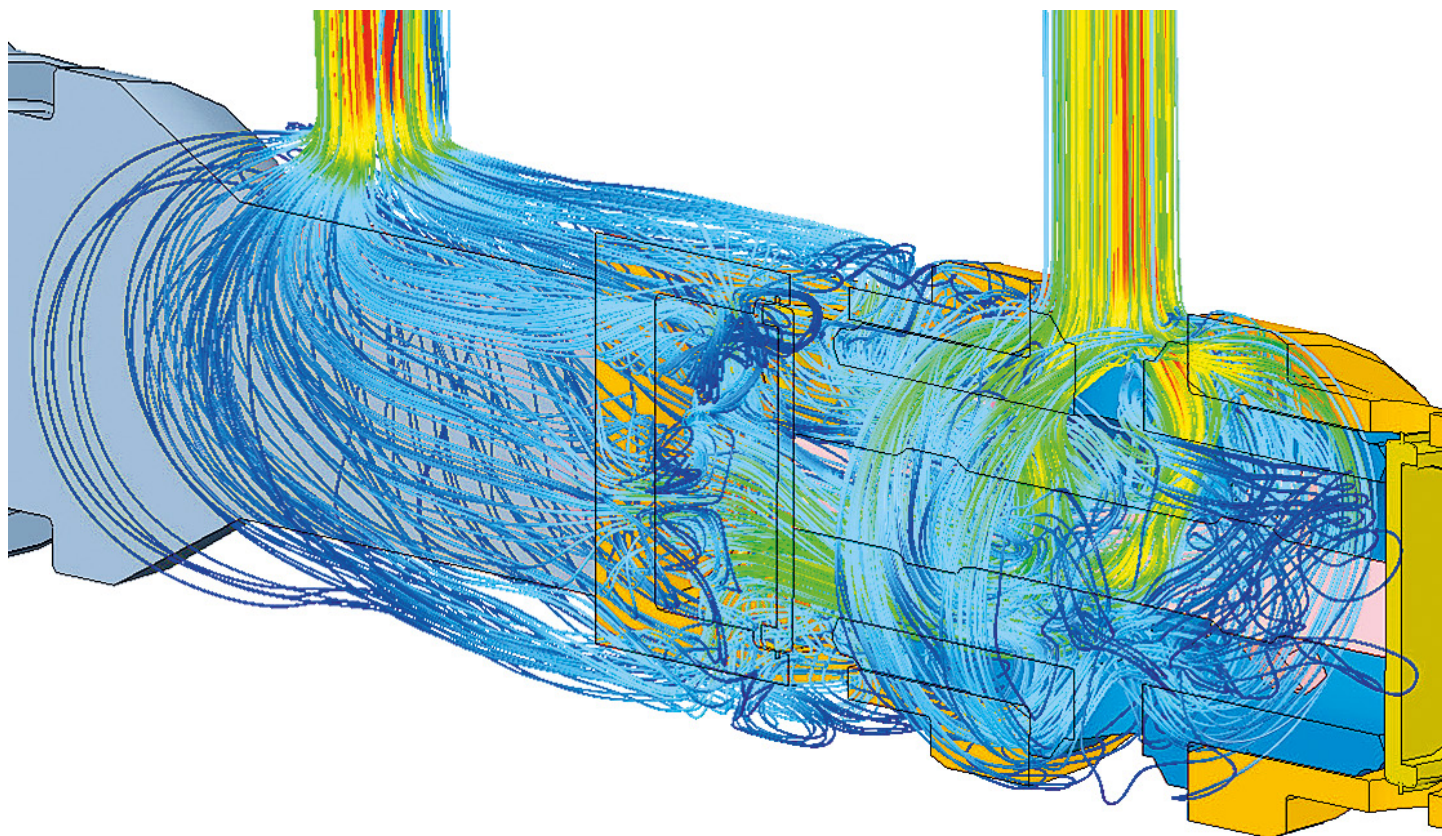


Figure 1. Flow Trajectories Inside the Valve.

The ever-shortening product cycles and decreasing development times in the automotive industry raise the need for up-to-date simulation tools equipped with reliable physical calculation methods. The use of Mentor Graphics' FloEFD Concurrent CFD software enables an evaluation of future automotive components at the earliest possible stage during the development cycle. This allows problem identification and correction when the concept is first evaluated at the feasibility stage of the project.

Steering assistance in commercial vehicles is performed by means of a hydraulic system

circuit. The double valve (Figures 1 and 2) is used to supply the feed pump as a control valve. The double valve consists of one inlet and two outlets. The two outlets are opened by pressing against the corresponding spring force depending on the operating condition. Each outlet is opened by undershooting the environment pressure in the requesting partial circuit. A pin controls the distance and the partial circuit is supplied with hydraulic oil after that. To supply the drive with the required flow rate capacity, the pressure drop arising within the valve must be overcome. If the pressure drop is too high, there will be insufficient flow to the drive, and the system will not function correctly. In addition,

a lower pressure drop reduces the power consumption of the hydraulic system, and thus the amount of energy required to steer the vehicle, contributing to the overall fuel savings and energy efficiency.

Hence the objective is to supply the required volume flow for each operating case, taking into account the given pressure conditions and keeping the pressure drop at required volume flow rates to a minimum. Simultaneously, cavitation effects have to be avoided. This is a critical consideration because the valve is opening by undercutting 0.95 bar below ambient (initial design shown in Figure 2). This pressure should be prevented from dropping

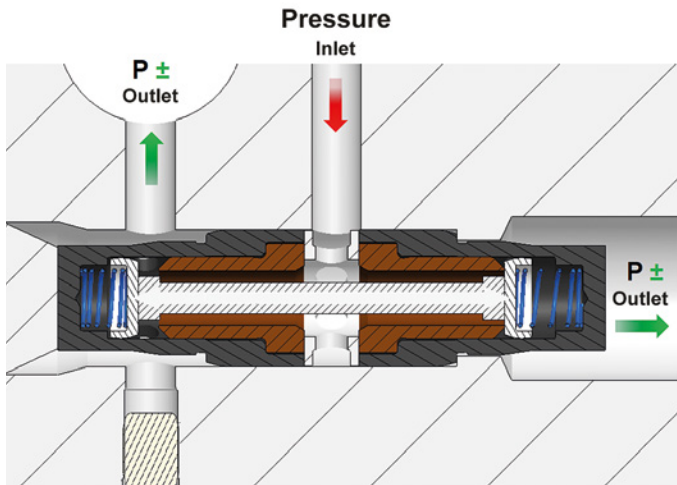


Figure 2. The initial design opens on the left by undershooting the environment pressure.

too low while being sufficiently negative to open the valve. At the same time, external factors constraining the design, such as available installation space and manufacturing capabilities have to be considered.

Several design variations for the double valve were investigated in FloEFD. Aside from the main geometry modifications, detailed changes to individual components and their effects were analyzed. For example, the pin designs shown in figures 3 and 4. The insights gained were incorporated at an early stage in the development of the product concept. The most efficient overall design based on the simulation results (Figures 5 and 6) was manufactured as a prototype and measured in a test setup. The measurements confirmed that the simulation results were accurate, reducing the number of physical prototypes to just one.

Using FloEFD for this application, the available flow rate was increased by approximately 300%, while the pressure drop was reduced by approximately 20% to approximately 0.8 bar below environment pressure. The time saving achieved compared to the conventional prototype-based development process was around five

weeks for the application described above. By “frontloading” simulation – simulating each design iteration at the beginning of the development process – the development process is streamlined, and optimized to ensure that each design iteration leads to an improvement in performance.

For FloEFD simulation Bosch Automotive Steering uses native 3D CAD data directly within the PTC Creo Parametric environment. During the modeling process, the fluid space is automatically captured and the mesh is generated from just a few settings within the software. Today Bosch development engineers use the parametric study capability within the PTC Creo environment to quickly prepare FloEFD simulations that are both fast and reliable to run, eliminating the need and cost of integrating with other software, or face the problems associated with using CAD neutral files including loss of parametric information and feature history.

In this case, by frontloading the CFD simulations Bosch Automotive was able to optimize the design of the pin in detail, allowing it to be designed for use across a series of such valves in the future. In

addition, with the simulation models being available for future analysis where the impact on the resulting weight and the quantity of material can be evaluated. Therefore cost optimizations have already been achieved at the product concept phase for the series.

“Using FloEFD within our PTC Creo environment has allowed us to front-load full CFD simulation into our design processes, cutting design times and making optimization possible from the very start of the development process. FloEFD has helped us meet today’s requirement for short development cycles.”

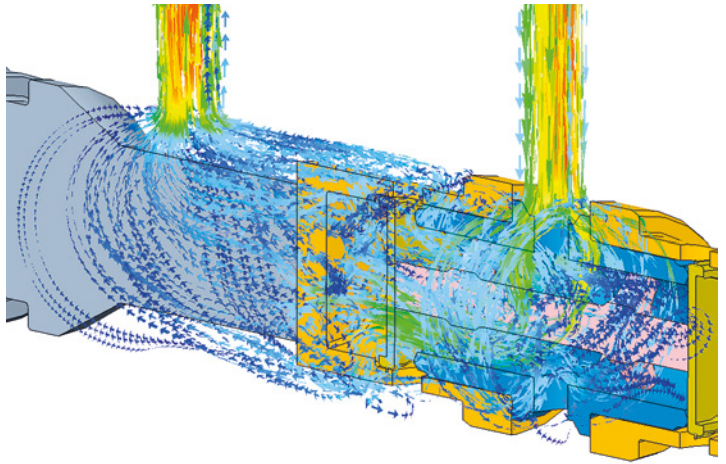


Figure 6. Flow Vectors Inside the Valve.

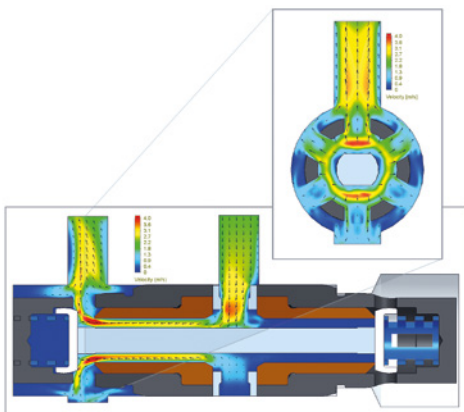


Figure 3. Design variation

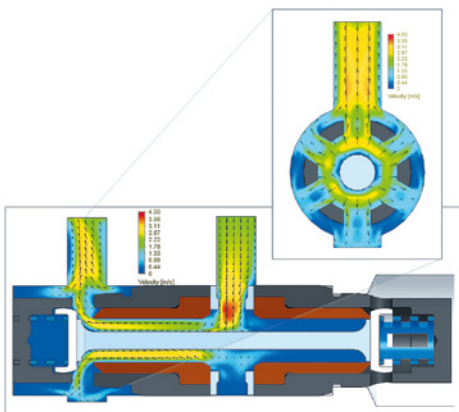


Figure 4. Design variation

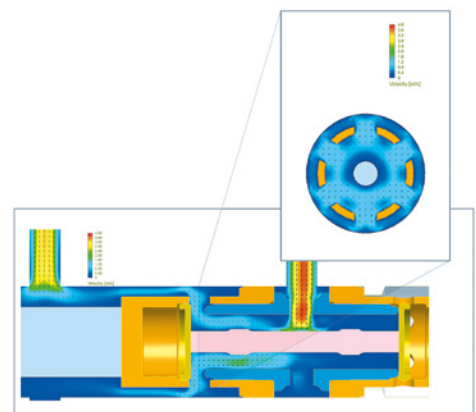


Figure 5. Design variation

Innovation isn't Optional

Mercury Racing® use FloEFD™ in the design of their latest intercooler filter

By Prasad Tota, Application Engineer, Mentor Graphics

Mercury Racing® is known worldwide for its leadership in powerboat racing and production of high performance consumer and race marine products. Founded in the 1970's as a division of Mercury Marine®, Mercury Racing's philosophy of "innovation isn't optional" has served them well and led their customers to winning multiple championships including the Unlimited Offshore World Championship and Abu Dhabi Grand Prix Class 1 World Championship.

Their product line includes sterndrive and outboard engines, drive and propellers. We met up with Hiro Yukioka, Technical Specialist, at Mercury Racing and their latest project, a design study of an intercooler filter on a sterndrive engine- QC4V (figure 1) using FloEFD™ 3D CFD simulation software from Mentor Graphics.

The 9L V8 engine with an output of up to 1650hp, has two turbochargers. The engine uses a charge air cooler (CAC) to cool the compressed air from the turbo charger. The CAC uses seawater as a coolant and comes with some challenges owing to the debris it picks up, such as sand, sea shell etc. Mercury Marine has found from field experience that not all seawater boat filtration systems are capable of preventing this debris from accumulating in the CAC.

In the existing design, the size of the passage where seawater enters into the CAC is less than 0.033" (0.84 mm), figure 2. However, it would be a mistake to assume that all the debris that enters the CAC will exit the CAC with the heated water leaving the unit. Depending on the flow velocity, some of the debris entering the CAC can settle or accumulate in the unit. If the water speed inside CAC is too low then debris could settle inside it. At such low velocities the debris accumulation is also influenced by gravity i.e. weight of the particles. FloEFD simulation software was used to study the performance of the existing filtration system and to come up with an improved design.

FloEFD for Creo is a CAD-embedded general purpose CFD software designed for engineers,

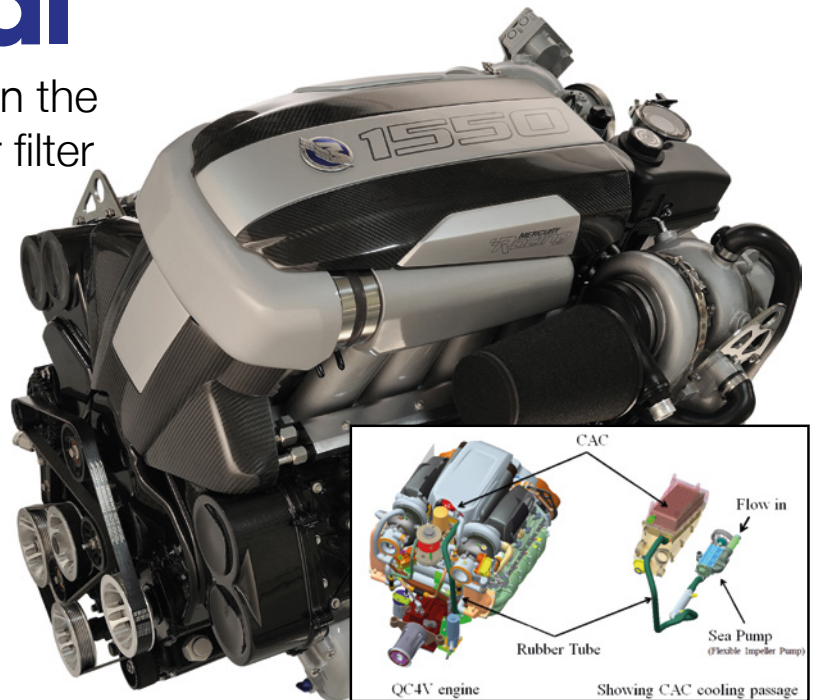


Figure 1. QC4V engine with compressed air cooler (CAC)

this focus makes the software easy to use by designers and engineers in an environment that they are already familiar with. The virtual test setup involves a CAD model with a flow inlet where the debris enters with the seawater, travels through a rubber tube into the CAC where some debris gets filtered and finally leaves from the flow outlet. It is important to note that the flow outlet is at a higher elevation than the inlet and hence the pump needs to deliver enough pressure for it to work against the adverse hydrostatic pressure.

At a flowrate of 60 litres/min the velocity inside the tube is about 3 m/s, but the velocity inside the CAC is less than 0.5 m/s. At such low velocities debris would settle inside the CAC. Hiro Yukioka had an idea to use the particle studies feature in FloEFD to virtually visualize if debris particles of a certain size would be carried by the seawater all the way to the outlet or remain in the unit. The particle study was conducted for debris size of 0.2 to 0.5mm in diameter in increments of 0.1 mm. The particles were fed in at a mass flow rate of 0.01 kg/s which is less than 1% of the fluid mass flow rate. Activating the gravity field in the model accounted for particles settling under their own

weight. The images in figure 3 show the particle trajectory colored by velocity magnitude.

Based on the findings, a sea strainer was created with wire mesh positioned around the inside of a cylindrical perforated part (Figure 4). The mesh element should have openings smaller than 0.3 mm and an off the shelf (OTS) wire cloth was chosen that met the criterion.

"If we wish to run a CFD simulation incorporating this new design the number of computational grid cells needed to refine the fine geometry of wire mesh is extremely high and impractical on a typical designer

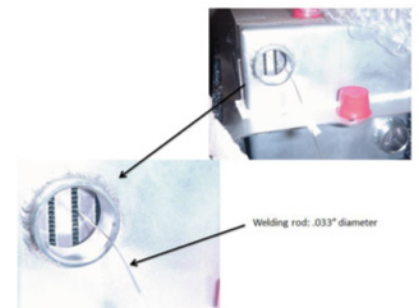


Figure 2. Fluid passage size at CAC entry



Figure 3. Virtual Debris test, Debris size from left to right (a) 0.2 mm (b) 0.3 mm (c) 0.5 mm

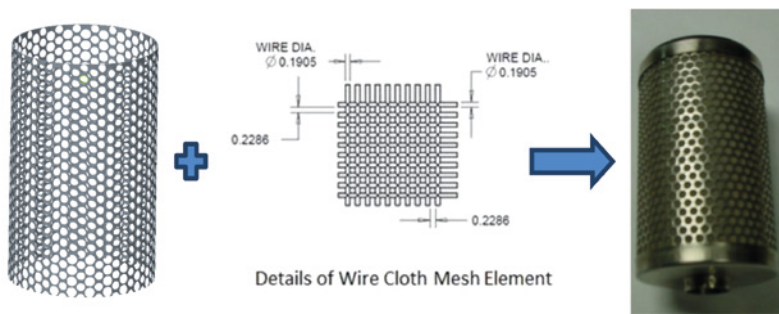


Figure 4. Sea strainer formed with a perforated part and wire mesh rolled on it

workstation. Fortunately FloEFD has a modeling technique where an object can be defined as a porous media which allows flow to go through the media with a pressure loss,” said Hiro. A resistance curve was attached to the porous object to emulate the flow vs pressure drop characteristics of the actual device. For this particular geometry an axisymmetric porous media is ideal where the flow loss coefficient (K) can be defined normal to flow direction (r, radial) and along the axis (L, length) of cylinder (Fig.5).

The resistance characteristics of the wire mesh can be either obtained in physical testing or virtual tests set up in FloEFD. In this case a section of wire mesh was tested in a virtual wind tunnel set up within FloEFD to come up with a flow vs. resistance curve that was then attached to the cylindrical part in the overall model for CAC.

The final FloEFD model with the wire mesh incorporated is shown in Figure. 7. The fluid flow simulations showed that the sea strainer results in a pressure drop of 20 kPa at a flowrate of 80 l/min.

The next step was to analyze the effect of debris accumulation on the pressure drop when a part of the overall height in cylindrical volume is completely covered with debris. This was easily tested with small modifications to the FloEFD model where a shell was added, blocking 50% of overall volume and using the parametric study feature in FloEFD this height was varied to 75% and 85%. The results show that there is minimal increase in pressure drop with debris accumulation. (Figure 8)

A prototype was built to validate the CFD results using thorough hardware testing. Physical tests showed a pressure drop of 25-30 kPa for the sea strainer that is new (no blockage) to 90% blockage to mimic the effects of debris accumulation. These findings are in good agreement with FloEFD predictions of 25-26 kPa for a flowrate of 80 l/min where blockage was varied from 0% to 85%.

Conclusion

After testing the prototype on a test rig for

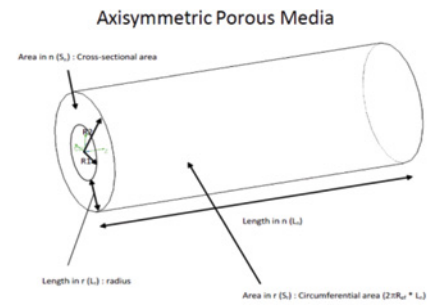


Figure 5. Axisymmetric Porous Media in FloEFD software

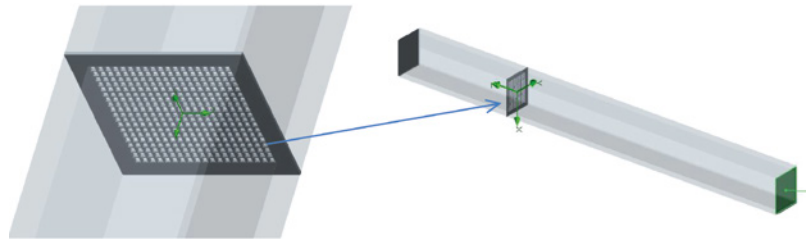


Figure 6. Virtual wind tunnel set up to characterize the wire mesh

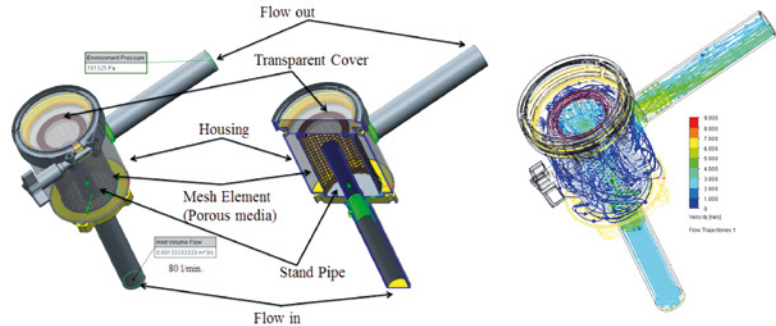


Figure 7. Cross section view of sea strainer and flow trajectories colored by speed (left to right).

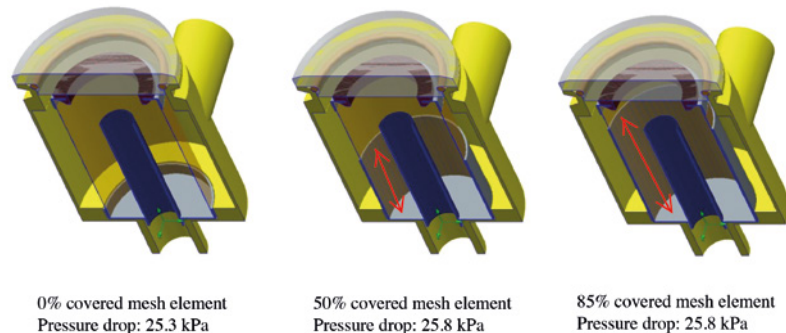


Figure 8. Debris accumulation effects on total pressure drop

several of Mercury Racing’s customers, the redesigned CAC on the field in various conditions, the customer feedback was overwhelmingly positive. Performance was not compromised and the CAC filter was presented at the Miami Boat show in February 2015 and was very well received.

“Without the FloEFD software it would have been very difficult to develop this CAC filter in such a short time. The software is embedded within CAD environment and easy to use, which allowed us to test various ideas and design virtually without the need to create multiple prototypes and several days of physical test.” said Hiro Yukioka.

Lastly I would like to express my gratitude to excellent customer support from Mentor Graphics. During this design activity I contacted them several times and every time I was impressed by their professionalism and great technical advice. FloEFD itself is an excellent product and, in my opinion, their support group adds significant value on this product.” Hiro Yukioka

Reference

[1] <http://www.mercuryracing.com/sterndrives/engines/1550-2/>





Fluid Dynamics Simulation Of Aqueous Humor In A Hole Implantable Collamer Lens Ks-Aquaport™

Concept and development history of the Hole Implantable Collamer Lens

By Takushi Kawamorita, CO, PhD, Department of Orthoptics and Visual Science,
Kitasato University School of Allied Health Sciences, Sagamihara, Japan.

Implantable collamer lenses (ICL) have many advantages in the treatment of refractive errors, especially for cases involving high and moderate ametropia. In addition, the ICL has been known to be effective for the correction of refractive errors when compared to the LASIK procedure. However, cataract development has been a concern after ICL implantation (Figure 1).

It has reported that the incidence of cataract formation was approximately 10 % after the implantation. One of the causes of the cataract was thought to be a change in the circulation of the aqueous humor to the anterior surface of the crystalline lens. Therefore, Prof. Kimiya Shimizu created a centrally perforated ICL in 2006 (i.e., the Hole-ICL KS-AquaPORT™) to improve aqueous humor circulation in addition to work performed on the development of the Hole-ICL (Figure 2).

Basis examination in Hole ICL Aqueous humor circulation

After observing improved aqueous humor circulation with the use of the Hole-ICL, Fujisawa [1] reported that no cataracts were formed when Hole-ICLs were implanted into

porcine eyes. The study concluded that the Hole-ICL allowed sufficient flow of aqueous humor and distribution over the anterior surface of the crystalline lens through its central hole. In addition, Shiratani et al. [2] showed the possibility of preventing cataracts with the Hole-ICL by using minipigs.

We investigated the fluid dynamics of the aqueous humor in a Hole-ICL using the thermal-hydraulic analysis software program FloEFD V5 (Mentor Graphics Corp.) (Figure 3).

The analysis confirmed an improvement in the aqueous humor circulation when using a Hole-ICL [3]. The total flow velocity between the anterior surface of the crystalline lens and the posterior surface of the Hole-ICL was higher than that between the crystalline lens and the conventional ICL (Figure 4).

The difference was of particular note in the center of the lens, as shown in the figure. An outward flow from the hole in the Hole-ICL by trajectory analysis was noted (Figure 5). The validity of the FloEFD software utilizing computational fluid dynamics was confirmed through the agreement between the theoretical and experimental data.

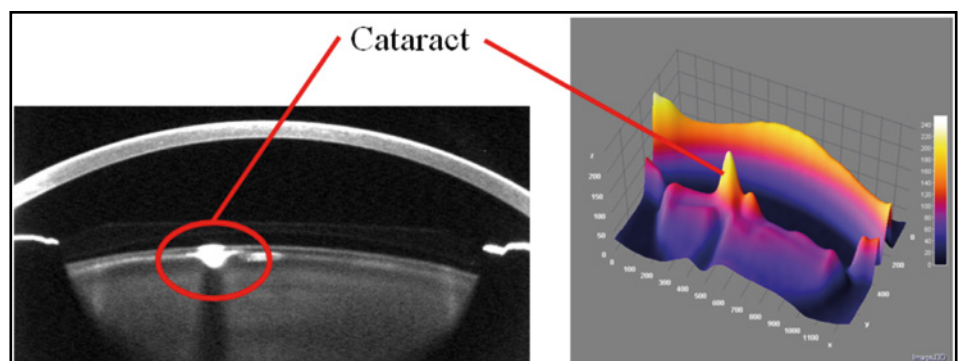


Figure 1. Cataract development of an eye with an ICL taken by Scheimpflug photography (left) and 3D densitometry by Image J 1.47v (NIH, USA) and the plug-in "Interactive 3D Surface Plot v2.33 by Dr. Barthel" (right)

In addition, many surgeons also perform peripheral laser iridotomy (LI) prior to ICL implantation to prevent the failure of aqueous humor circulation (Figure 6). The advantages of the Hole-ICL include improvements in aqueous humor circulation; hence, there is no need for the LI procedure as it may cause complications including the elevation of intraocular pressure.

There are several examples of optical systems with a centrally perforated lens, such as astronomical telescopes or special contact lens. Shiratani et al. [2] showed that the modulation transfer function of an ICL with a central hole of diameter 1.0 mm obtained using optical simulation software was similar to a conventional ICL. Uozato et al. [4] investigated the optical performance of the Hole-ICL with a diameter of 0.36 mm in an optical bench test as well as optical simulations. The authors concluded that a minimal central hole in an ICL may not have a significant impact on the optical performance for various ICL powers and pupil sizes. If the central hole size of the Hole-ICL were to increase, the circulation of aqueous humour in the surrounding crystalline lens would improve. However, the retinal image quality decreases. This indicates the existence of a trade-off between fluid dynamics and optical characteristics. Therefore, we investigated the ideal hole size in a Hole-ICL from the standpoint of the fluid dynamic characteristics of the aqueous humor using the FloEFD software (Figure 7).

The results of the computer simulation determined the desirable central hole size as 0.2 mm or larger based on fluid dynamics. The current model, based on a central hole size of 0.36 mm, was close to the ideal size. The optimization of the hole size should be performed based on results from a long-term clinical study to allow for analysis of the optical performance and incidence rate of secondary cataracts. A slight decrease in optical properties is considered an effective measure of risk mitigation when compared to low retinal image quality that can occur because of the potential for secondary cataracts to develop. In the future, the optimum hole size should be determined based on these simulation results, the results of optical analysis containing illumination optics, and long-term clinical results regarding visual performance, optical performance and complications.

Clinical results of the Hole ICL

Our results suggest that Hole-ICLs improve the circulation of the aqueous humor to the anterior surface of the crystalline lens. The Hole-ICL is expected to continue to lower the risk of cataracts. Currently, the Hole-ICL

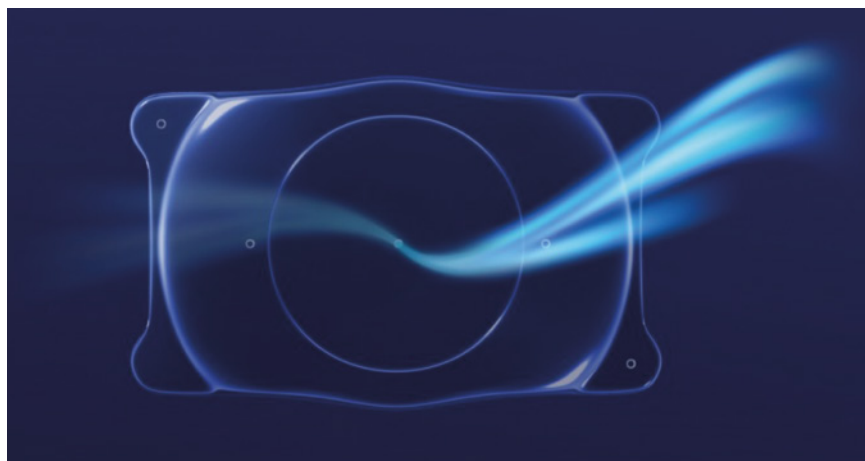


Figure 2. Illustration of the Hole-ICL KS-AquaPORTTM (STARR Surgical CO Ltd.)

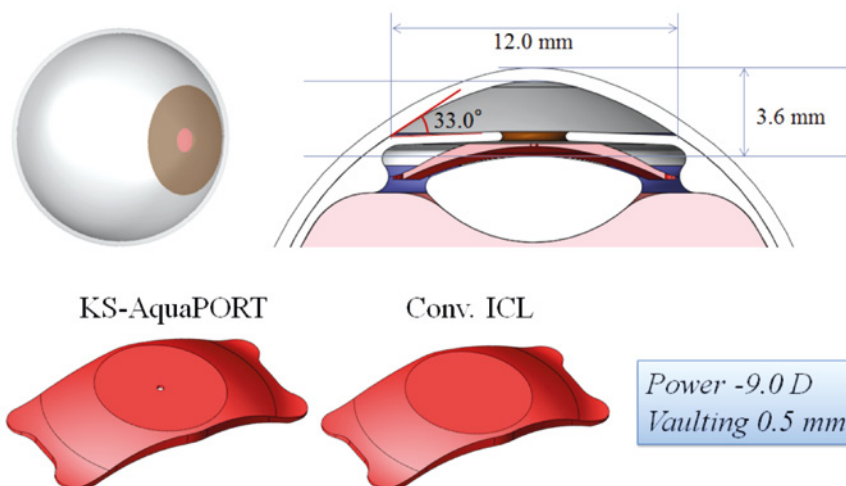


Figure 3. 3D models of eyes with ICLs created with FloEFD software. Appearance of the eye model (top left), Anterior ocular segment (top right), Conventional ICL (bottom left), Hole-ICL (bottom right)

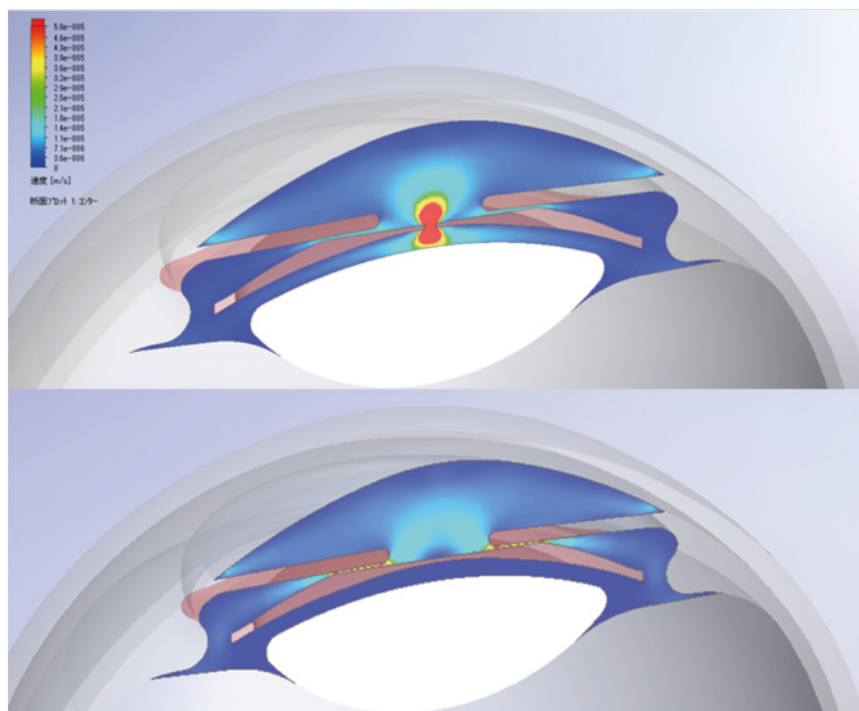


Figure 4. Flow distribution along the long axis of the cross-sectional surface of the Hole-ICL (upper) and the conventional ICL (lower)



has been used approximately 200,000 times with lenses from approximately 70 countries. There are useful clinical reports with similar visual functions as the conventional ICL (Figure 8) [5, 6]. In conclusion, the thermal-hydraulic analysis software program FloEFD contributed to the optimization of the lens design.

Acknowledgment

The authors thank Prof. Kimiya Shimizu, Prof. Hiroshi Uozato, Prof. Nobuyuki Shoji, Kozo Keikaku Engineering Inc. (Mr. Osamu Kuwahara, Mr. Soichi Masuda, and Dr. Tsuyoshi Yamada), Cybernet Systems Co., Ltd. (Mr. Takayuki Sakaguchi) for technical support, and Editage for critical reading of the manuscript. This study was supported by a grant from the Kitasato University School of Allied Health Sciences (Grant-in-Aid for Research Project) (T.K.), a Kitasato University Research Grant for Young Researchers 2010-2016 (T.K.), and a Grant-in-Aid for Young Scientists (B) (T.K.).

References

- [1] Fujisawa K, Shimizu K, Uga S, et al. Changes in the crystalline lens resulting from insertion of a phakic IOL (ICL) into the porcine eye. *Graefes Arch Clin Exp Ophthalmol*. Jan 2007;245(1):114-122.
- [2] Shiratani T, Shimizu K, Fujisawa K, Uga S, Nagano K, Murakami Y. Crystalline lens changes in porcine eyes with implanted phakic IOL (ICL) with a central hole. *Graefes Arch Clin Exp Ophthalmol*. May 2008;246(5):719-728.
- [3] Kawamorita T, Uozato H, Shimizu K. Fluid dynamics simulation of aqueous humour in a posterior-chamber phakic intraocular lens with a central perforation. *Graefes Arch Clin Exp Ophthalmol*. Jun 2012;250(6):935-939.
- [4] Uozato H, Shimizu K, Kawamorita T, Ohmoto F. Modulation transfer function of intraocular collamer lens with a central artificial hole. *Graefes Arch Clin Exp Ophthalmol*. Jul 2011;249(7):1081-1085.
- [5] Kamiya K, Shimizu K, Saito A, Igarashi A, Kobashi H. Comparison of optical quality and intraocular scattering after posterior chamber phakic intraocular lens with and without a central hole (Hole ICL and Conventional ICL) implantation using the double-pass instrument. *PLoS One*. 2013;8(6):e66846.
- [6] Shimizu K, Kamiya K, Igarashi A, Shiratani T. Intraindividual comparison of visual performance after posterior chamber phakic intraocular lens with and without a central hole implantation for moderate to high myopia. *Am J Ophthalmol*. Sep 2012;154(3):486-494 e481.1

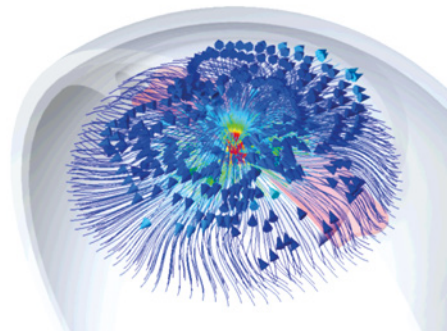


Figure 5. Trajectory analysis within the Hole-ICL

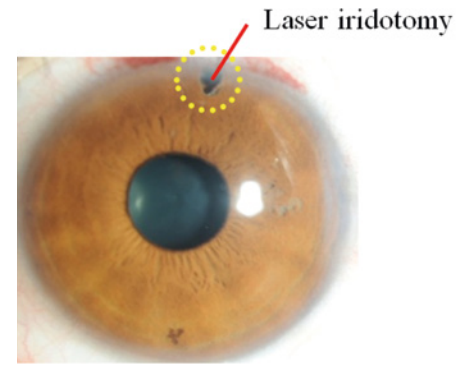


Figure 6. Photograph of laser iridotomy

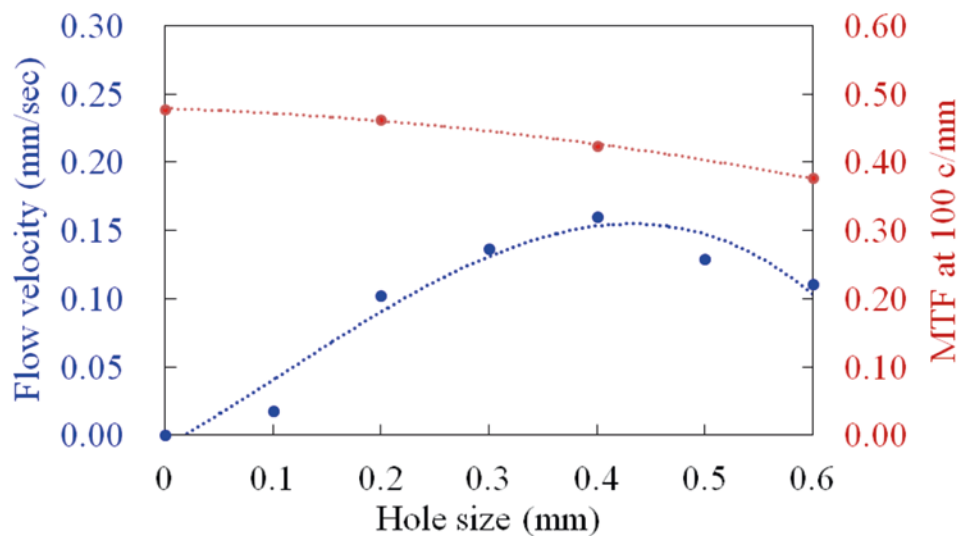


Figure 5. The relation between hole sizes and velocity of the aqueous humor fluid, including the modulation transfer function at a spatial frequency of 100 c/mm

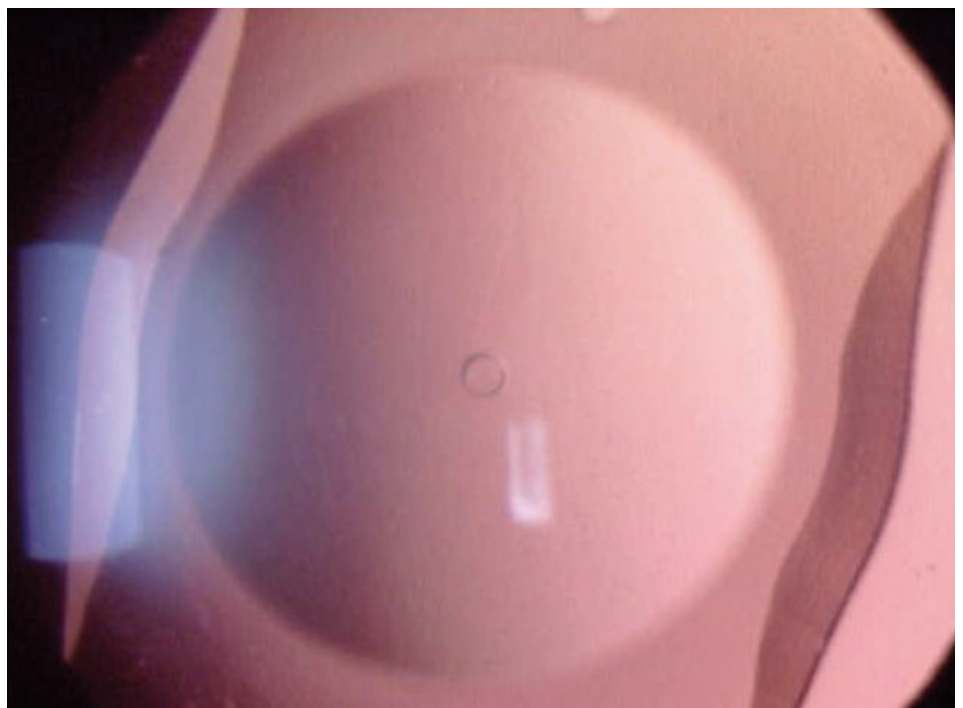


Figure 8. Photograph of an eye implanted with the Hole ICL KS-AquaPORTTM (STARR Surgical CO Ltd.)

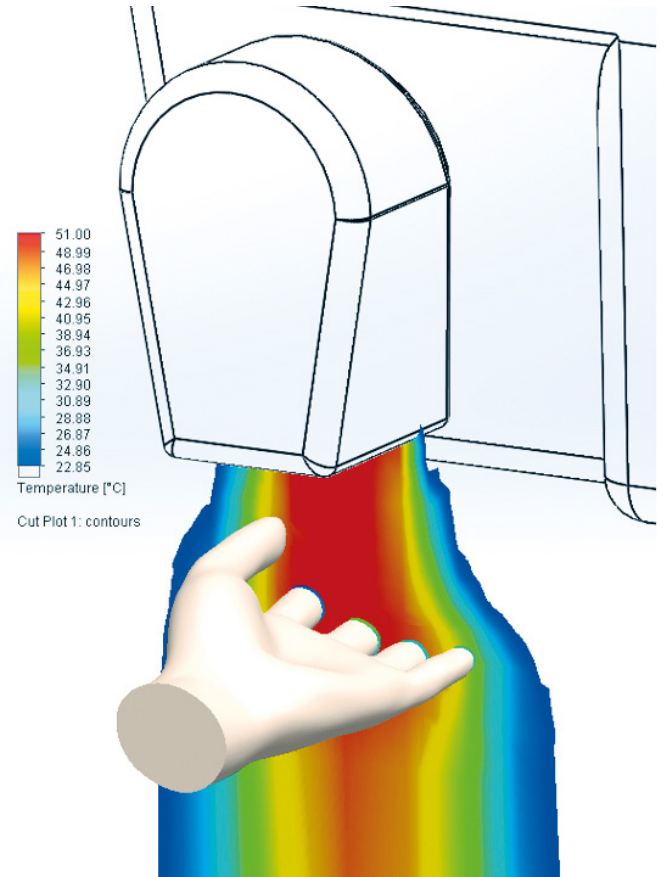
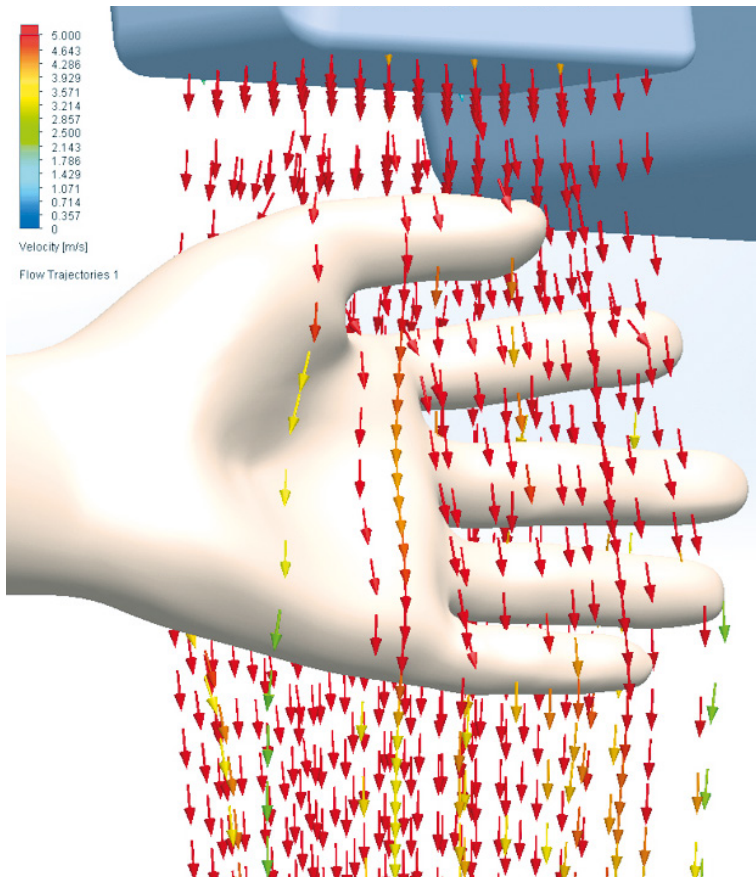


Figure 1. FloEFD Model of a Convectively Dried Hand

What's the Fastest Way to Dry Your Hands? FloEFD Investigates...

Robin Bornoff, Market Development Manager, Mentor Graphics

I haven't got very big hands, quite the opposite in fact, so it's not as if I spend an inordinate amount of time standing there with my just washed hands under a convective hand dryer in a public/office toilet (who has these things at home anyway?). Whenever I do though I'm always wondering whether I'm doing it right. Should I rotate my hands, leave them in one position, if so, which position? Why didn't they teach us these things at school? I've got better things to do than just stand here wishing there were some paper towels to dry my hands with instead, so it's logical to pose the question "what's the fastest way to dry your hands under such a dryer?" Just the sort of question that can be answered with FloEFD!

A 3D model was constructed with a hand placed below a mass flow boundary condition applied to an underside face of a convective hand dryer part. Hot-dry air blown over the hand and a transient simulation conducted.

It's always a good idea to deconstruct a question to ensure it is answered correctly. What does 'dry' mean? In terms of hand drying I found out that it is common to consider a hand dry when it has lost 90% of the initial water that was clinging to the skin.

FloEFD has a 'water film' feature where an amount of water on a surface can be simulated, including the transient effects of evaporation. A transient simulation requires an initial condition of the thickness

of the water film when drying commences. I chose 25 microns (though I did find references of anything up to 100 micron water film thickness after hands are submerged and retracted from a water bath).

I modeled the hand at 10 different orientations and tracked the reduction in the total water film mass over time. The relative reduction of these orientations, together with a comparison of the drying rate when the hand rotated, is shown in the following graph. Due to the qualitative nature of this study I've left the time axis blank.

When the hand is vertically orientated it reaches the 90% dry condition fastest (Design Point 10). Both sides of the wet hand are well dried by the hot air stream that passes over both sides at once. The slowest drying is when the hand is near horizontal (Design Point 7). Here the back of the hand is very well shielded from the hot air and, although the water mass initially decreases quickly (as the palm of the hand gets all the drying) the back of the hand takes much longer.

Further insight into the drying process can be seen when surface plotting the reduction in water film thickness at various percentages of water film mass reduction. Red represents a thick water film, blue represents dry skin.

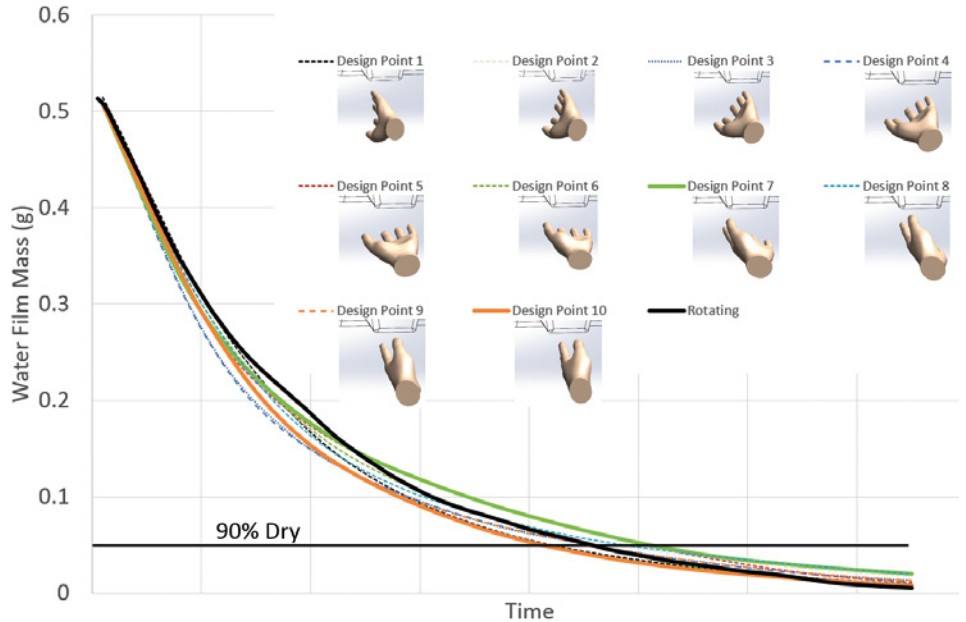


Figure 2. Water Film Mass Reduction Rates for Various Hand Orientations

The fingers dry first due to their large surface area in proportion to their volume, the palm finishing last.

I had assumed that a rotating hand would dry quickest, this was not the case. Although more hand surface area is apparent to the hot air flow in a given time period, it doesn't stay still long enough for

the water film to experience locally rapid drying. Sure, in the end it's the fastest for complete drying, but by that time you could be back to the bar enjoying your next beer.

So, next time you're drying your hands, keep them vertical and be patient (unless of course you're using paper towels!)

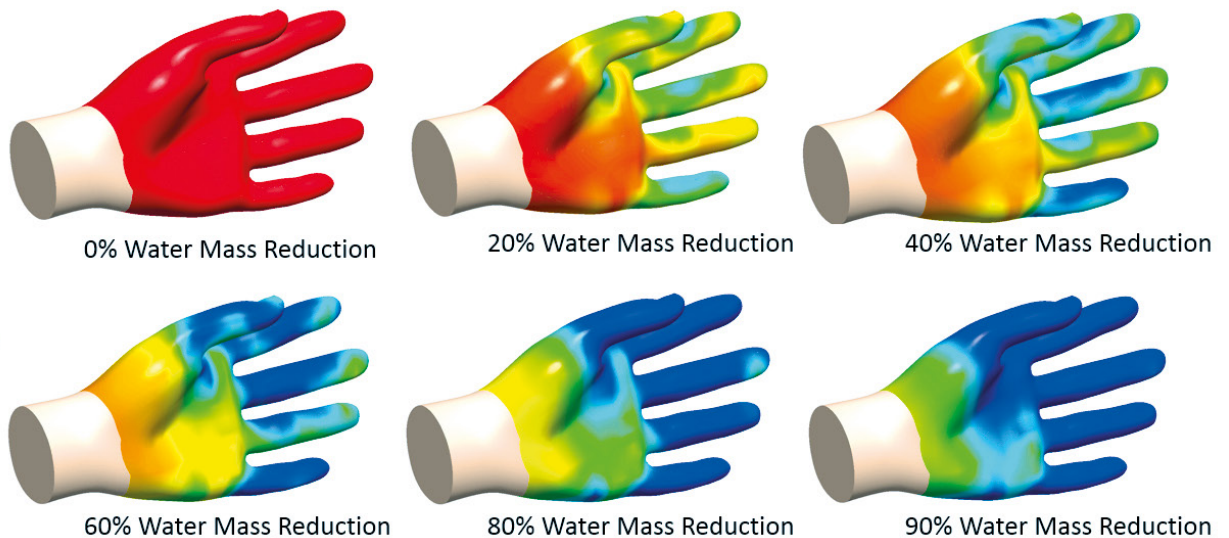
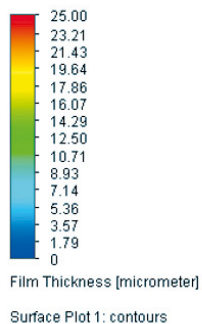


Figure 3. Water Film Thickness Reduction for Vertical Hand Orientation

Geek Hub



Competition

Are you Engineering Fit for Rio 2016?

How can CFD improve an Olympic sport or an athlete's performance?

Send us your simulations and you could win \$500 of Amazon Vouchers and be published in the next issue of Engineering Edge.

How?

- 1 Simulate any Olympic event, athlete or equipment using MAD CFD software
- 2 Provide a short 200 - 300 word explanation
- 3 Send us your work: ee@mentor.com by the 8th July 2016

Terms & Conditions apply. Go to: <http://bit.ly/1rZEeOZ>



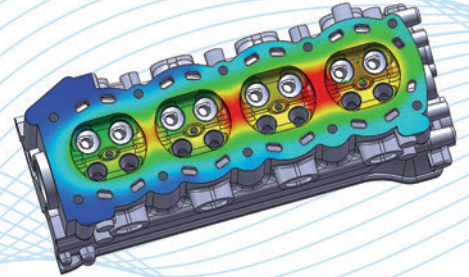
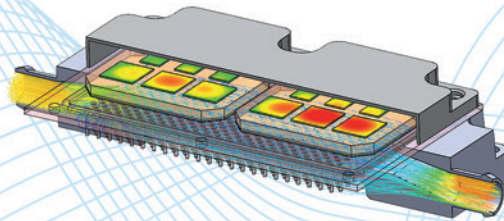
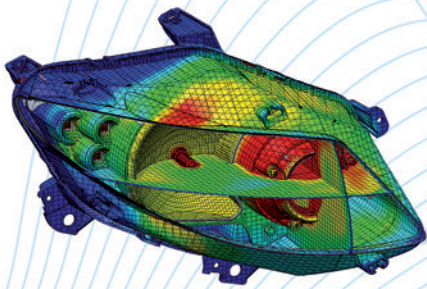
**Mentor
Graphics**

Mechanical Analysis

FloEFD Simulation Conference 2016

8th - 9th November 2016 Frankfurt, Germany

Join us at the inaugural **FloEFD Simulation Conference 2016**, the first global event dedicated to FloEFD, a leading frontloading Computational Fluid Dynamics (CFD) solution. The event showcases multiple applications across several industries including Aerospace, Automotive, Telecoms, Consumer Products and Manufacturing.



This event is an excellent opportunity to meet and network with other FloEFD users and also a platform to talk directly to the FloEFD Development Team to hear first-hand product insights. Existing users and prospective users would both benefit from this event.

The event will be held 8th-9th Nov, 2016 at the **Frankfurt Marriott Hotel** near the **Frankfurt Fair Tower**. An additional third day of FloEFD general training is available for attendees.

Register your interest here: go.mentor.com/4z9xi